



UNIVERSIDAD NACIONAL AUTÓNOMA DE MÉXICO
PROGRAMA DEL POSGRADO EN CIENCIAS DE LA TIERRA
INSTITUTO DE GEOFÍSICA
GEOFÍSICA DE LA TIERRA SÓLIDA

**Exploración geofísica somera en sitios de la Zona
Metropolitana de la Ciudad de México**

TESIS
QUE PARA OPTAR POR EL GRADO DE:
DOCTOR EN CIENCIAS DE LA TIERRA (GEOFÍSICA DE LA TIERRA SÓLIDA)

PRESENTA:

ALEJANDRO ROSADO FUENTES

TUTOR
DRA. MARÍA ALEJANDRA ARCINIEGA CEBALLOS
INSTITUTO DE GEOFÍSICA

COMITÉ TUTOR

DR. FRANCISCO JOSÉ SÁNCHEZ SESMA
INSTITUTO DE INGENIERÍA

DR. MARTÍN CÁRDENAS SOTO
FACULTAD DE INGENIERÍA

CIUDAD DE MÉXICO, MÉXICO, JUNIO 2024



UNAM – Dirección General de Bibliotecas

Tesis Digitales
Restricciones de uso

DERECHOS RESERVADOS ©
PROHIBIDA SU REPRODUCCIÓN TOTAL O PARCIAL

Todo el material contenido en esta tesis está protegido por la Ley Federal del Derecho de Autor (LFDA) de los Estados Unidos Mexicanos (México).

El uso de imágenes, fragmentos de videos, y demás material que sea objeto de protección de los derechos de autor, será exclusivamente para fines educativos e informativos y deberá citar la fuente donde la obtuvo mencionando el autor o autores. Cualquier uso distinto como el lucro, reproducción, edición o modificación, será perseguido y sancionado por el respectivo titular de los Derechos de Autor.

COMITÉ TUTOR :

Dra. María Alejandra Arciniega Ceballos - Instituto de Geofísica
Dr. Francisco José Sánchez Sesma - Instituto de Ingeniería
Dr. Martín Cárdenas Soto - Facultad de Ingeniería

JURADO EXAMINADOR :

Presidente - Dr. Francisco José Sánchez Sesma
Vocal - Dr. Juan Esteban Hernández Quintero
Secretario - Dra. María Alejandra Arciniega Ceballos
Suplente - Dra. Claudia Arango Galván
Suplente - Dr. Fernando Corbo Camargo

“We require science, technology, and innovation
to transform our country and improve
the lives of our people”

- Dr. Mokshagundam Visvesvaraya

Agradecimientos

El agradecimiento más grande y dedicatoria de este trabajo es para mi familia, Beatriz, Mario, Mario y Héctor, que de una forma u otra apoyan y motivan fuertemente y constantemente mi vida personal y académica; y para Mishel, por todos los momentos vividos, los paseos, las pláticas y las emociones de compartir esto contigo; además del gran apoyo y motivación durante todo el proceso. La UNAM la construimos todos, la amplia gama de oportunidades y actividades que brinda, desde seminarios hasta actividades extracurriculares, han enriquecido mi experiencia educativa y contribuido a mi desarrollo y crecimiento académico y profesional. Quiero expresar mi reconocimiento y agradecimiento a todas las instituciones y personas que fueron partícipes de este proceso, de forma directa o indirecta. Por ellos es pertinente mencionar los agradecimientos de todos los productos desarrollados durante el doctorado, aunque se reiteren de forma particular en cada uno de ellos. Agradezco especialmente al Posgrado en Ciencias de la Tierra, al Instituto de Geofísica y en particular al Servicio Geomagnético por apoyar y permitir desarrollar el Campo de Pruebas Geofísicas Teoloyucan dentro del Observatorio Geomagnético de Teoloyucan. A la Comisión Nacional del Agua (CONAGUA) por proporcionar la información litológica de los pozos del Programa de Acción Inmediata ramal Teoloyucan.

Agradezco el apoyo sustancial y económico mediante el financiamiento, beca, campañas de campo y asistencia a congresos brindados de forma directa e indirectamente por la DGA-PA, UNAM a través de los proyectos PAPIIT IN105716, IN108219, IN107720, IN104823 e IN105523, por el CONACYT mediante la beca 620517/ 336033 y el proyecto UC MEXUS-CONACYT número CN-18-51, por el UNAM-UI Research Partnership Program 2023, por la NSF, USA mediante los proyectos EAR-1620576, CMMI-1266418, CMMI-1822482 y CMMI-2100889, por el Posgrado en Ciencias de la Tierra y por Grupo MARQ. Al Servicio Sismológico Nacional, UNAM y la Red Universitaria de Observatorios Atmosféricos, UNAM por el uso de datos de la estación sismológica PPIG y meteorológica Altzomoni, respectivamente. A los comités, directores y personal administrativo del Posgrado en Ciencias de la Tierra por su apoyo y orientación desde la inscripción hasta la titulación, en particular a Araceli Chaman.

A mi tutora, la Dra. María Alejandra Arciniega Ceballos, con quien he trabajado y colaborado desde la licenciatura. A los miembros del Comité Tutor, los Drs. Francisco José Sánchez Sesma y Martín Cárdenas Soto, su colaboración y orientación a lo largo del doctorado ha favorecido mi desempeño académico. A los co-autores de los artículos, particularmente al Dr. J. Esteban Hernández Quintero, la Dra. Claudia Arango Galván y Dr. Clinton M. Wood. Al Dr. Fernando Corbo Camargo, miembro del Jurado Examinador. A la Dra. Linda R. Manzanilla Naim por permitirnos el acceso en Teotihuacan, Estado de México. Al Arqlgo. Gustavo Alberto Ramírez Castilla y su grupo de trabajo por invitarme a colaborar en el salvamento arqueológico Chak-Pet, Tamaulipas. A la Dra. Rosa Guadalupe de la Peña Virchez, al Arqlgo. Ricardo A. Jaramillo Luque y al Mtro. Héctor Pérez García por invitarme a colaborar en el Cerro Toloche, Toluca, Estado de México. A las Dras. Patricia Pérez Martínez y Tamara Cruz

y Cruz por invitarme al proyecto en Santa Isabel Ixtapan, Estado de México. A la Dra. Ana María Soler Arechalde y al Museo de Geofísica por las invitaciones a divulgar la ciencia. A los comités, directores y personal administrativo de la Facultad de Ciencias y la Escuela Nacional de Ciencias de la Tierra por las facilidades para formarme íntegramente en las Ciencias de la Tierra a través de mis actividades como docente. Este trabajo culmina, mas no los proyectos e ideas en las que seguramente seguiremos colaborando en el futuro.

A Gerardo M. Mendo Pérez, José Luis Salas Corrales, Félix A. Centeno Salas, Arnaldo Hernández Cardona, Walter A. Flores García, Diego Quiroz Suárez y Abner D. González Bernal por su apoyo en campo y gabinete, y las discusiones que enriquecieron los estudios realizados. A Jesús Ancira por su apoyo crucial durante la construcción del Campo de Pruebas Geofísicas Teoloyucan y su mantenimiento. A la maestra Elia F. China Torres y la Escuela Secundaria Pública en San Baltazar Atlimeyaya, Puebla por las facilidades para colocar la red sismo-acústica ATLI. Finalmente se agradece a quienes apoyaron las campañas de adquisición de datos de campo: César Pacheco Aguirre, Iván Campos Cerón, Marco A. Mendoza Rojas, a los estudiantes de la Dra. L. R. Manzanilla Naim y mis estudiantes de Geofísica Aplicada 1 y 2 de los semestre 2024-1 y 2024-2 de la ENCiT, UNAM. Por último, pero no menos importantes, a mis amigos del Columbia y del *árbol* quienes de forma directa o indirecta han apoyado y motivado la continuidad de mis proyectos.

Índice general

Resumen	1
Abstract	2
Introducción	3
1. Caracterización geofísica, diseño y construcción del Campo de Pruebas Geofísicas de Teoloyucan para aplicaciones arqueológicas y de ingeniería, Centro de México	7
1.1. Resumen del artículo	8
1.2. Resumen de los resultados del artículo	8
1.3. Artículo publicado	12
2. Mapeo de estructuras someras en un campo de pruebas geofísicas usando gradientes magnético y de inducción electromagnética	26
2.1. Resumen del artículo	27
2.2. Resumen de los resultados del artículo	28
2.3. Artículo publicado	32
2.4. Material suplementario	44
3. Mediciones de velocidad de onda de corte y periodo fundamental del sitio en la parte occidental de la Cuenca de la Ciudad de México después del sismo de magnitud Mw 7.1 de 2017 en Puebla-Morelos, México	54
3.1. Resumen del artículo	56
3.2. Resumen de los resultados del artículo	57
3.3. Artículo publicado	60
4. Otros productos y actividades	83
Conclusiones	85
Referencias	87

Resumen

El texto de esta tesis doctoral mediante la modalidad de artículos publicados en revistas indexadas internacionales parafrasea, en español, el contenido de los mismos artículos presentados en el documento. Este trabajo incluye estudios de exploración geofísica somera multi-técnica realizados en distintos puntos dentro de la Zona Metropolitana de la Ciudad de México, en particular en Teoloyucan, Estado de México y en la parte occidental de Ciudad de México (CDMX), zona que resultó fuertemente dañada por el sismo Mw 7.1 Puebla-Morelos del 19 de septiembre de 2017. En cada estudio se combinan al menos dos de las siguientes técnicas: radar de penetración terrestre (GPR), tomografía de resistividad eléctrica (ERT), gradiente magnético (MG), inducción electromagnética (EMI), tomografía de refracción sísmica (SRT), análisis multicanal de ondas superficiales (MASW), arreglo multicanal de microtretemores (MAM) y cociente espectral H/V (HVSR), todas abreviadas por sus siglas en inglés.

A raíz de la necesidad de contar en México con campos de pruebas en el área de exploración geofísica que estén documentados y enfocados a fortalecer las técnicas ingenieriles y aquellas que coadyuven a la arqueología y el patrimonio cultural, se diseñó y construyó el Campo de Pruebas Geofísicas Teoloyucan (TGTS - por sus siglas en inglés) dentro del Observatorio Geomagnético de Teoloyucan (TGO - por sus siglas en inglés), de la Universidad Nacional Autónoma de México (UNAM) en Teoloyucan, Estado de México. Previo a su construcción, el área se caracterizó geofísicamente por la combinación de cinco técnicas: GPR, ERT, MG, EMI y SRT. Los resultados se integraron con los resultados de un análisis granulométrico y el perfil litoestratigráfico. La integración muestra que el subsuelo se conforma de cuatro capas de suelo grueso bien graduado con interfaces relativamente planas y la presencia de anomalías someras atribuidas a desechos antropogénicos. Un segundo estudio se realizó en el TGTS con las técnicas de MG y EMI en el que se propone complementar las metodologías de adquisición y procesamiento de datos, incluyendo emplear la novedosa técnica de Gradiente de Inducción Electromagnética (EMIG - por sus siglas en inglés). Los resultados indican la conveniencia de utilizar las metodologías propuestas y de aplicar la técnica EMIG pues con ello se resaltan anomalías que pasarían desapercibidas con las metodologías convencionales.

Por otra lado se aborda la caracterización pasiva y activa de la parte occidental de la CDMX mediante la combinación de técnicas sísmicas: MASW, MAM y HVSR. En este estudio se conjuntan perfiles 1D de velocidad de onda de corte (V_s) y mediciones de periodo fundamental del sitio; estas últimas se compararon con los periodos fundamentales obtenidos por otros estudios y por las Normas Técnicas Complementarias por Diseño Sísmico de la CDMX. Los resultados muestran que los primeros 60 m del subsuelo están conformados por cinco capas principales cuyos valores de V_s y espesor dependen de la ubicación, puesto que varían a lo largo de la zona de estudio. De igual forma se analiza con mayor detalle la capa de arcillas lacustres blanda no consolidada por dominar los efectos sísmicos. Por último se mencionan otros productos y actividades realizadas durante el doctorado que han contribuido a mi formación íntegra como profesional y académico en el área de las Ciencias de la Tierra.

Abstract

The text contained in this PhD dissertation through the modality of published articles in indexed international journals paraphrases, in Spanish, the content of the same articles presented in the document. This work presents multi-technique shallow geophysical exploration studies carried out at different sites within Mexico City's Metropolitan Area, particularly in Teoloyucan, State of Mexico and in the western portion of Mexico City (CDMX) that was heavily damaged by the Mw 7.1 Puebla-Morelos earthquake on September 19, 2017. Each study combines at least two of the following techniques: ground penetrating radar (GPR), electrical resistivity tomography (ERT), magnetic gradient (MG), electromagnetic induction (EMI), seismic refraction tomography (SRT), multichannel analysis of surface waves (MASW), multichannel array of microtremors (MAM) and H/V spectral ratio (HVSR).

The Teoloyucan Geophysical Test Site (TGTS) was designed and built within the Teoloyucan Geomagnetic Observatory (TGO), National Autonomous University of Mexico (UNAM - for its acronym in Spanish) in Teoloyucan, State of Mexico due to the need to have documented geophysical exploration test sites in Mexico that are focused on strengthening engineering techniques and those that contribute to archaeology and cultural heritage. Prior to its construction, the area was geophysically characterized by combining five techniques: GPR, TRE, MG, EMI and SRT. The results were integrated with the results of a granulometric analysis and the lithostratigraphic profile. They show that the subsoil is made up of four layers of thick, well-graded soil with relatively flat interfaces and the presence of shallow anomalies attributed to anthropogenic debris. A second study is carried out at the TGTS with MG and EMI techniques which suggests to complement the data acquisition and processing methodologies, including the implementation of the new Electromagnetic Induction Gradient (EMIG) technique. The results indicate the convenience of using the proposed methodologies and applying the EMIG technique since this enhances anomalies that would go unnoticed with the application of conventional methodologies.

On the other hand, a passive and active characterization of the western portion of CDMX is addressed through the combination of seismic wave techniques: MASW, MAM and HVSR. In this study, 1D shear wave velocity (V_s) profiles and site period measurements are combined, the latter were compared with site periods obtained by other studies and with CDMX's Complementary Technical Standards for Seismic Design. The results show that the first 60 m of the subsoil are composed by five main layers whose V_s and thickness values vary throughout the study area since they depend on the location. Likewise, the unconsolidated soft lacustrine clay layer is analyzed in greater detail because it dominates the seismic site effects. Finally, other products and activities carried out during the doctorate that have contributed to fully consolidating me as a professional and academic in the field of Earth Sciences are mentioned.

Introducción

La exploración geofísica engloba una amplia variedad de métodos, técnicas y metodologías físicas y matemáticas, tanto cuantitativas como analíticas. Su finalidad es inferir desde la superficie y mediante la distribución de las propiedades físicas del subsuelo la ubicación, geometría, profundidad, área de afectación y zonas de continuidad y discontinuidad de cualquier estructura geológica o antropogénica que se encuentre en el subsuelo. Por su versatilidad, los métodos de exploración geofísica (MEG) se aplican en diversas disciplinas como geología, agricultura, ciencias forenses, geotermia, hidrocarburos, minería, protección civil e hidrología [Erkan, 2008; Everett, 2013; Reynolds, 1997; Telford *et al.*, 1978]. En particular, los estudios geofísicos reportados en esta tesis se concentran a casos particulares de aplicación en contextos ingenieriles, arqueológicos y de patrimonio cultural.

En muchos contextos los estudios geofísicos enriquecen, complementan y precisan información, contribuyendo en el diseño, proyección, planeación y ejecución de proyectos y ahorran recursos y tiempo. La complejidad de establecer guías de trabajo radica en que la selección del método y técnica a utilizar depende de los objetivos del estudio, las características físicas del objeto de estudio y del subsuelo en su entorno, las condiciones ambientales y del terreno, de las características y limitaciones de los sensores y de las metodologías de adquisición y procesamiento de datos [Isaacson *et al.*, 1999]. Considerando adicionalmente el principio de la no unicidad de modelos, por ser métodos no directos, y que un cambio en la distribución de las propiedades físicas del subsuelo no necesariamente refleja un cambio litológico; para reducir la incertidumbre en los modelos y su interpretación es conveniente realizar estudios multi-técnica e integrar los diferentes resultados [Erkan, 2008; Everett, 2013; Reynolds, 1997]. Por lo anterior, en cada artículo mencionado en este trabajo se realizaron estudios multi-técnica combinando al menos dos de las siguientes técnicas: gradiente magnético (MG), inducción electromagnética (EMI), tomografía de resistividad eléctrica (ERT), tomografía de refracción sísmica (SRT), radar de penetración terrestre (GPR), análisis multicanal de ondas superficiales (MASW), arreglo multicanal de microtremores (MAM) y cociente espectral H/V (HVSR), todas abreviadas por sus siglas en inglés.

Aunando al párrafo anterior, en muchos estudios geofísicos no se tiene certeza de la presencia, o no, de las características geológicas o antropogénicas que se deducen de los resultados. Aunque se trabaje con una combinación de métodos y técnicas, esta incertidumbre es sostenida también por el poco o nulo contraste de propiedades físicas que puedan tener las distintas características del subsuelo y su entorno, a que el contexto en el que se encuentran está conformado por diversas capas superpuestas con propiedades similares y poca distancia entre ellas o inclusive a que los objetos de interés estén hechos con los mismos materiales que se encuentran en su entorno [Pringle *et al.*, 2012]. Esto conlleva a que en algunos casos sea necesario verificar los resultados geofísicos con métodos directos como excavaciones o perforaciones, o realizar métodos directos para recuperar los objetos de interés y/o extraer muestras para otros estudios en laboratorio que complementen los estudios de exploración geofísica [Everett, 2013].

Surge entonces la necesidad de contar con campos de pruebas para investigar la respuesta geofísica del subsuelo por características geológicas o antropogénicas conocidas dentro de un contexto también conocido. Los campos de prueba son útiles para validar métodos, técnicas o metodologías, probar nuevas ideas, comparar datos sintéticos con mediciones de campo, probar nuevas tecnologías, sensores o arreglos y para calibrar instrumentos [Isaacson *et al.*, 1999; Wai-Lok Lai *et al.*, 2018]. Por otro lado, estos sitios pueden ser usados para la formación de recursos humanos, capacitando estudiantes y técnicos en el uso y manejo de equipo geofísico. Su diseño y construcción replica y simula contextos con características semejantes a sitios de distintas ramas de estudio para estudiar su respuesta geofísica.

El presente trabajo para obtener el grado de doctor muestra parte de las investigaciones realizadas en exploración geofísica durante el lapso del doctorado. El escrito conjunta tres artículos que tratan de estudios multi-técnica de exploración geofísica somera en diversos sitios dentro de la Zona Metropolitana de la Ciudad de México (ZMVM). Si bien el resto de las investigaciones y sus productos se mencionan en el último capítulo, *Capítulo 4*, no fueron incluidos en este escrito por no tener una relación tan estrecha con los artículos tratados aquí. Sin embargo, se reconocen y agradecen todos los apoyos obtenidos a lo largo del doctorado.

En este sentido, dos de los artículos mostrados en el presente escrito abarcan estudios realizados en el Campo de Pruebas Geofísicas de Teoloyucan (TGTS). Este campo fue diseñado para contextos de ingeniería y patrimonio cultural y se ubica dentro del Observatorio Geomagnético de Teoloyucan, UNAM en el municipio de Teoloyucan, Estado de México. El primer artículo, presentado en el *Capítulo 1*, abarca el diseño y construcción del TGTS en un área primeramente caracterizada geofísicamente con el estudio multí-técnica de MG, EMI, ERT, SRT y GPR que se describe también en ese mismo artículo [Rosado-Fuentes *et al.*, 2021]. El segundo artículo, presentado en el *Capítulo 2*, trata de una propuesta que complementa las metodologías de adquisición y procesamiento de datos para MG y EMI. En este segundo artículo se propone y presentan resultados de la novedosa técnica de Gradiente de Inducción Electromagnética (EMIG) [Rosado-Fuentes *et al.*, 2023]. Cabe mencionar que el TGTS se encuentra disponible para la comunidad académica y la iniciativa privada previa solicitud a los autores de los artículos y el Instituto de Geofísica, UNAM. El grupo de investigación conformado durante el doctorado continuamente aplica diferentes técnicas geofísicas en el TGTS; nuestros resultados podrán encontrarse en otro tipo de trabajos y publicaciones en el futuro.

Por otro lado, gran parte de la ZMVM se encuentra dentro de la Cuenca de México, una cuenca endorréica de forma elipsoidal que comenzó a formarse por una compleja e intensa actividad volcánica desde el Oligoceno Tardío. Al cerrarse por completo en el Pleistoceno con la formación de la Sierra Chichinautzin, el agua no desemboca hacia el río Balsas y comienza su acumulación, y la de los sedimentos que arrastra, en las partes más bajas [Mooser *et al.*, 1974; Padilla y Sánchez, 1989]. Así nace el sistema lacustre de la Cuenca de México, del cual hoy en día quedan algunos remanentes en Texcoco, Zumpango, Xochimilco y Tláhuac. Las características topográficas que tenía la Cuenca antes de cerrarse provocaron que los lechos

de los lagos que conformaban el sistema lacustre fueran topográficamente irregulares. Estas características también propiciaron la formación de islotes y una deposición sedimentaria de tamaño granular variable y con distribución horizontal [Padilla y Sánchez, 1989]. Si bien el propio sistema lacustre favoreció el asentamiento, desarrollo, evolución y subsistencia del ser humano dentro de la Cuenca, es la propia actividad humana, desde tiempos Prehispánicos, que modifica la naturaleza del ecosistema hasta desecar, casi en su totalidad, el sistema lacustre que tanto le favoreció. Con el constante crecimiento de la mancha urbana continuamos modificando y disminuyendo las zonas de recarga del acuífero, sobre-exploitamos el acuífero y desecharmos las aguas fuera de la Cuenca mediante un sistema complejo de obras hidráulicas [Alcocer y Williams, 1996; Campos-Enríquez *et al.*, 1997; Lozano-García y Ortega-Guerrero, 1998].

Con más de 21,436,911 habitantes [SEDATU, 2024], la ZMVM es claramente la urbe más poblada del país y una de las más pobladas del mundo. Los MEG pueden aportar mucha información valiosa y ayudar a resolver problemas relacionados con la localización y caracterización de agua subterránea, agrietamientos y hundimientos, urbanización y planeación, identificación de zonas de riesgo y filtrado, ubicación, localización y construcción de infraestructura pública y privada, identificación de restos arqueológicos y paleontológicos e interacción suelo-estructura ante un evento sísmico, por mencionar algunos. Si bien estos problemas no son exclusivos de la ZMVM, es aquí donde toman mayor relevancia, en particular aquellos entorno al riesgo y peligro sísmico. A lo largo de la historia la ZMVM ha sufrido graves daños por el efecto de los sismos (e.g. Franke *et al.* [2019]; Pestana *et al.* [2002]; Seed *et al.* [1988]; Singh *et al.* [1988, 2018]). Uno de los eventos más recientes fue el sismo Puebla-Morelos del 19 de septiembre de 2017 con Mw 7.1. Con una distancia epicentral de 120 km al sureste de la Ciudad de México, el evento generó un estado de emergencia en 320 municipios del centro del país, 369 personas perdieron la vida y se afectó un estimado de 28 millones de personas, 54,000 escuelas y 5,700 edificaciones del sector salud. En la CDMX colapsaron 38 edificaciones, 340 se catalogaron como de alto riesgo y otras 273 fueron catalogadas como de seguridad incierta [GEER, 2017; Singh *et al.*, 2018].

Asociado a que gran parte de la CDMX está asentada sobre los lechos del prácticamente extinto sistema lacustre, estudios previos han mostrado una amplificación significativa de las ondas sísmicas dentro de la Cuenca [Chávez-García y Bard, 1994; Kawase y Aki, 1989; Lermo y Chávez-García, 1994; Seed *et al.*, 1988], una zonificación de la CDMX por la categorización del periodo fundamental del sitio [Lermo *et al.*, 2020; Pérez-Rocha *et al.*, 1995; Sánchez-Sesma *et al.*, 1993], una prolongada duración de las ondas sísmicas dentro de la Cuenca [Kawase y Aki, 1989] y que las áreas circundantes están conformadas por depósitos de roca erosionada y suelos duros, mientras que las áreas centrales están conformadas principalmente por depósitos de arcilla lacustre muy blanda no consolidada que aumentan su espesor desde el borde de la Cuenca hacia su centro. Estos depósitos lacustres están intercalados con capas de limo arenoso muy denso o arcillas más gruesas [Mooser, 1975; Santoyo Villa *et al.*, 2005]. De las capas lacustres, la capa más crítica es la de arcilla no consolidada muy blanda por dominar los efectos de sitio como la amplificación y larga duración del movimiento del terreno [Kawase y

Aki, 1989; Molina-Villegas *et al.*, 2018; Pestana *et al.*, 2002; Seed *et al.*, 1988; Sánchez-Sesma *et al.*, 1993; Wood *et al.*, 2019]. Aunque su velocidad de onda de corte (V_s) es generalmente menor a 100 m/s, su valor real y espesor dependen de la ubicación [Mayoral *et al.*, 2016; Pestana *et al.*, 2002; Wood *et al.*, 2019]. Adicionalmente, se ha demostrado el acortamiento de los periodos de sitio con el tiempo debido a cambios constantes de las propiedades de esta capa de arcilla lacustre [Arroyo *et al.*, 2013; Wood *et al.*, 2019]. Por ello es sumamente importante caracterizar geológicamente y geofísicamente toda la Cuenca de México. En particular, realizar estudios dirigidos a conocer más a fondo las características y propiedades estáticas y dinámicas de la capa de arcilla lacustre no consolidada muy blanda. A pesar de poder investigar sus propiedades utilizando distintos métodos, un número limitado de estudios se han realizado al respecto en toda la Cuenca [Mayoral *et al.*, 2008, 2016; Wood *et al.*, 2019]. En este sentido, el tercer artículo, presentado en el *Capítulo 3*, trata de la caracterización activa y pasiva con métodos de ondas sísmicas superficiales de la parte occidental de la CDMX, la cual sufrió graves daños por el sismo de Mw 7.1 de Puebla-Morelos de 2017 [Wood *et al.*, 2023].

1. Caracterización geofísica, diseño y construcción del Campo de Pruebas Geofísicas de Teoloyucan para aplicaciones arqueológicas y de ingeniería, Centro de México

(Artículo publicado, citar como: Rosado-Fuentes, A., Arciniega-Ceballos, A., Hernández-Quintero, E., Arango-Galván, C., Salas-Corrales, J. L. and Mendo-Pérez, G. (2021). Geophysical characterization, design and construction of the Teoloyucan Geophysical Test Site for archaeological and engineering applications, Central Mexico. *Journal of Applied Geophysics*, 194, 104459. <https://doi.org/10.1016/j.jappgeo.2021.104459>)

Este capítulo trata del primer artículo publicado referente al Campo de Pruebas Geofísicas de Teoloyucan (TGTS). Es el punto de partida para cualquier estudio que se realice en este sitio y es referencia para otros campos de prueba diseñados con otros objetivos y en otros contextos geológicos.

Hasta donde sabemos, existían solamente tres sitios de pruebas en México que se han estudiado con diferentes técnicas geofísicas. Dos de ellos están diseñados para contextos de ingeniería, uno está compuesto por contenedores de plástico y metal vacíos o llenos de algún líquido enterrados a 1.20 m de profundidad [Blancas-Vázquez *et al.*, 1996] y el otro contiene tubos de concreto, plástico y metal enterrados a una profundidad máxima de 1.00 m [Gres-Hernández, 2010]. El tercer sitio fue diseñado para un contexto forense donde los objetos fueron enterrados en los primeros 1.40 m de profundidad [Quiroz-Suárez, 2020]. A ellos se agrega el Campo de Pruebas Geofísicas de Teoloyucan, siendo el campo más completo y complejo hasta ahora diseñado para varios contextos de ingeniería y arqueología en México. El TGTS, ubicado en el Observatorio Geomagnético de Teoloyucan, UNAM en el municipio de Teoloyucan, Estado de México, cuenta con 17 estructuras enterradas a menos de 2.0 m de profundidad que cubren una amplia variedad de geometrías, secuencias estratigráficas y materiales que se han usado para la construcción, en México, desde la época Prehispánica.

Previo a la construcción del TGTS, el sitio seleccionado fue caracterizado con una combinación de técnicas someras no invasivas, como MG, EMI, GPR, ERT y SRT. Se diseño el TGTS para calibrar equipo, probar técnicas someras de exploración geofísica, capacitar estudiantes e investigar nuevas ideas en la adquisición, procesamiento e interpretación de estructuras someras en contextos de ingeniería y arqueología. La construcción del campo fue documentada para controlar cuantitativamente los parámetros espaciales y materiales de las estructuras enterradas. Aunque ya se completó su construcción y no se tiene prevista ninguna modificación al campo ni extenderlo añadiendo nuevas estructuras, el equipo de investigación conformado durante el doctorado continúa realizando estudios de investigación en el sitio.

1.1 Resumen del artículo

El TGTS está diseñado para replicar y simular diversos escenarios encontrados en contextos arqueológicos e ingenieriles. Está concebido para calibrar instrumentos, probar técnicas geofísicas someras, capacitar estudiantes y desarrollar nuevas ideas para estudios someros e interpretación de datos. El TGTS fue construido dentro del Observatorio Geomagnético de Teoloyucan de la UNAM en el poblado de Teoloyucan, al norte de la Ciudad de México. El campo de pruebas tiene una superficie de 864.00 m^2 , está conformado por 17 estructuras enterradas a menos de 2.00 m de profundidad con formas regulares e irregulares, y con capas verticales y horizontales que simulan secuencias estratigráficas. Para su elaboración se seleccionaron materiales similares a aquellos que comúnmente se emplean desde la época prehispánica (adobe, madera, basalto, tezontle) y materiales actuales (concreto, concreto armado, contenedores de plástico y PVC). Previo a la construcción, el área de estudio fue caracterizada por una combinación de técnicas geofísicas someras no invasivas que incluyen gradiente magnético, inducción electromagnética, radar de penetración terrestre, tomografía de refracción sísmica y tomografía de resistividad eléctrica. Las propiedades físicas de las estructuras (densidad, módulos elásticos, conductividad eléctrica y susceptibilidad magnética) y sus características geométricas son bien conocidas, por lo que en ese aspecto la respuesta geofísica somera del TGTS está controlada. Los resultados geofísicos indican la presencia de tres interfaces planas a profundidades aproximadas de 0.45 m, 0.91 m y 1.82 m, respectivamente. El análisis litológico indica que las capas están conformadas por suelos bien gradados y de grano grueso, incluyendo dos horizontes volcánicos duros (tepetates). Los resultados geofísicos coinciden con la litología de Teoloyucan, demostrando que el área seleccionada es adecuada para el campo de pruebas. Hasta donde se sabe, es el único campo de pruebas para estructuras arqueológicas e ingenieriles en México y de los pocos existentes en América.

1.2 Resumen de los resultados del artículo

- Creación de una sección litoestratigráfica de los primeros 20.00 m de profundidad a lo largo de los pozos de extracción de agua del Programa de Acción Inmediata (PAI) ramal Teoloyucan con información solicitada a la Comisión Nacional del Agua (CONAGUA).
 - Conformada mayoritariamente por sedimentos aluviales o lacustres intercalados con depósitos de arena, arcilla o limo que pueden extenderse hasta 280.00 m de profundidad.
 - Presencia de sedimentos volcanoclásticos en los primeros 10.00 m de profundidad como toba o una capa de ceniza de 8.00 m de espesor.
 - El perfil sugiere que el límite norte de la unidad geológica TplA (andesita-dacita del Neógeno) al norte del centro de Teoloyucan debería estar más cercana a la batería de pozos del PAI-Teoloyucan. Manteniendo una frontera similar a la unidad geológica Qhoal (aluvión del Cuaternario) como se observa al límite sur del centro de Teoloyucan y el Observatorio Geomagnético Teoloyucan (TGO).

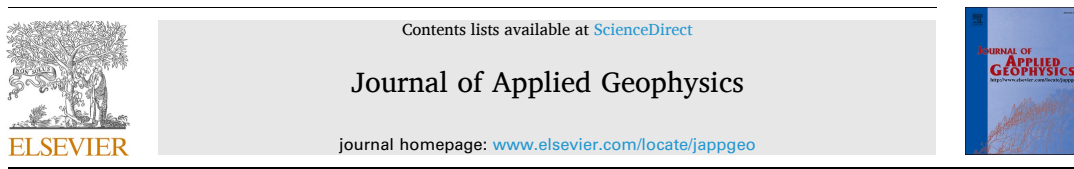
- Caracterización geofísica somera multi-técnica en un área de 24 x 36 m dentro del TGO de la UNAM, en Teoloyucan, Estado de México. Misma que puede ser empleada como referencia para otras zonas del municipio de Teoloyucan o en zonas de los municipios circundantes como Coyotepec, Cuautitlán, Melchor Ocampo, Tepotzotlán y Tultepec.
- Mapeo y perfiles coincidentes empleando las técnicas MG, EMI, GPR, SRT y ERT.
 - El mapa de MG muestra que el campo magnético total en el sitio se encuentra en el rango 120.00 - 420.00 nT.
 - Los mapas generados con la técnica EMI muestran valores de conductividad aparente y fase de 70.00 - 120.00 mS/m y 1.14 - 1.63 ppt, respectivamente.
 - La esquina noreste tiene los valores de conductividad y fase más altos, mientras que los valores más bajos se encuentran en la esquina sureste.
 - El área del TGTS puede ser considerada magnética y electromagnéticamente constante por el rango de valores y porque no se presenta ninguna tendencia considerable.
 - Los perfiles de SRT indican la existencia de tres capas planas. La capa más somera tiene un espesor promedio de 0.50 m y un rango de velocidad de onda P (V_p) de 380 - 560 m/s. La segunda capa tiene un espesor de 0.25 m y un rango de V_p de 560 - 750 m/s. La tercera capa inicia a una profundidad promedio de 0.75 m y su V_p incrementa ligeramente de 750 m/s en la esquina noroeste a 930 m/s en la esquina sureste.
 - Los perfiles de ERT y GPR indican la existencia de cuatro capas planas con pequeños desniveles. Las primeras tres capas tienen espesores promedio de 0.43 m, 0.56 m y 0.86 m, y rangos de resistividad aparente de 12.50 - 20.20 Ωm, 7.70 - 28.00 Ωm y 3.00 - 20.20 Ωm; respectivamente. La capa más profunda comienza a una profundidad promedio de 1.85 m y tiene un rango de resistividad aparente de 3.0 - 12.5 Ωm.
 - Las interfases de SRT coinciden con las primeras dos interfases de ERT y GPR, a profundidades promedio de 0.45 m y 0.91 m.
 - La interfase más profunda de ERT y GPR no se observa claramente en los perfiles de SRT por el bajo contraste de impedancia entre las capas contiguas.
 - Los perfiles de SRT, ERT y GPR muestran depresiones similares a una profundidad promedio de 0.90 m y con un ancho promedio de 6.50 m.
 - Los perfiles de ERT muestran cuatro dipolos eléctricos centrados a una profundidad promedio de 1.40 m y ubicados a un lado de reflectores observados en los perfiles de GPR localizados a una profundidad promedio de 1.14 m.
 - Los resultados indican que el sitio presenta una distribución suave de propiedades físicas sin la presencia de discontinuidades ni cambios abruptos. Las anomalías presentes en el sitio no debieran enmascarar ni contribuir a la respuesta geofísica de los objetos enterrados en futuros estudios. El área estudiada es ideal para la construcción del TGTS.

- Ubicación, excavación y remoción de anomalías magnéticas someras generadas por desechos antropogénicos modernos, así como la recuperación de tepalcates y obsidiana.
 - La profundidad del dipolo magnético más intenso fue estimada en 0.22 *m* y 0.15 *m* mediante las reglas de Tilburg y Hansel, respectivamente.
 - Mediante una excavación del área se encontraron restos de una cubeta metálica de pintura a una profundidad promedio de 0.20 *m*, dentro del rango estimado por las reglas de Tilburg y Hansel.
- Diseño y construcción del TGTS con base en los resultados obtenidos por la interpretación individual y conjunta de las técnicas geofísicas someras empleadas.
 - Diseño de 17 estructuras con formas regulares e irregulares.
 - + Ocho estructuras cúbicas con las mismas dimensiones: concreto (2), concreto armado (1), basalto (1), tezontle (1), tabique (1), madera (1) y adobe (1).
 - + Dos contenedores cuadrados de plástico que simulan una cavidades: 1 vacía y una que se puede llenar con algún líquido.
 - + Tres estructuras cilíndricas: concreto (1) y tuberías de PVC selladas (2).
 - + Dos estructuras que simulan secuencias estratigráficas compuestas de cubos de materiales descritos anteriormente: secuencia vertical (1) y secuencia horizontal (1).
 - + Dos estructuras irregulares hechas de concreto sin estructuras metálicas.
 - Excavación de 17 hoyos a menos de 2.00 *m* de profundidad para la construcción *in situ* de las 17 estructuras, niveladas y orientadas oeste-este o sur-norte. Los hoyos fueron rellenados y compactados con el material de la excavación, salvo por una estructura de concreto que fue rellenada con arena.
 - Se tuvo un estricto control de la ubicación de los hoyos y de las estructuras enterradas, sus dimensiones, profundidad y espesor del material de relleno en cada hoyo. Con ello se generaron planos de ubicación y secciones transversales sur-norte y oeste-este de cada estructura enterrada.
- Toma y análisis granulométrico de 19 muestras de suelo recuperadas en tres hoyos excavados.
 - Para cada muestra analizada se grafican las curvas de frecuencia acumulada de sedimentos utilizando la transformación Phi (Φ). Los parámetros estadísticos calculados son diámetro promedio, diámetro medio, desviación estándar, asimetría, segunda asimetría y curtosis.
 - Para cada muestra se determina la densidad promedio y el índice promedio de vesicularidad.
 - El análisis muestra que el TGTS está compuesto por tres capas de suelo grueso bien gradado.

- + La primera es una capa de arena gruesa con raíces, en ella se encontraron los tepalcates y obsidiana.
- + La segunda es una capa de transición de grava fina compuesta por un tepetate beige mezclado ligeramente con tierra y raíces delgadas.
- + La tercera capa es un tepetate de arena gruesa a grava fina.
- + La esquina suroeste del TGTS parece tener una capa adicional de suelo grueso compuesto por un tepetate de arena.
- + Lo anterior se plasma en una sección litoestratigráfica de TGTS con sentido suroeste-noreste.
- + La mayoría de los porcentajes de composición de los tepetates no concuerdan con valores obtenidos en otros estudios.
- + La primer interfase de esta secuencia es muy somera y no se muestra en los resultados geofísicos.
- + Considerando las profundidades promedio de las interfasas, la segunda y tercera interfasas de la secuencia litoestratigráfica coinciden con la primera y segunda interfase geofísica.
- + La tercera interfase geofísica se encuentra a mayor profundidad que la alcanzada por la secuencia litroestratigráfica.

1.3 Artículo publicado

[Journal of Applied Geophysics 194 \(2021\) 104459](#)



Geophysical characterization, design and construction of the Teoloyucan Geophysical Test Site for archaeological and engineering applications, Central Mexico



Alejandro Rosado-Fuentes^{a,*}, Alejandra Arciniega-Ceballos^b, Esteban Hernández-Quintero^b, Claudia Arango-Galván^b, José Luis Salas-Corrales^b, Gerardo Mendo-Pérez^a

^a Posgrado en Ciencias de la Tierra, Universidad Nacional Autónoma de México, 04510 CDMX, Mexico

^b Instituto de Geofísica, Universidad Nacional Autónoma de México, 04510 CDMX, Mexico

ARTICLE INFO

Keywords:
Geophysical characterization
Non-invasive
Multi-technique
Teoloyucan
Near-surface
Test site

ABSTRACT

The Teoloyucan Geophysical Test Site (TGTS) is designed to replicate and simulate scenarios encountered in engineering and archaeological contexts. It is meant for calibrating instruments, testing near-surface geophysical techniques, training students and developing new ideas for shallow surveys and data interpretation. TGTS has been built within the Teoloyucan Geomagnetic Observatory of the Universidad Nacional Autónoma de México (UNAM) in the town of Teoloyucan, N of Mexico City. The test site covers an area of 864.00 m², consisting of 17 structures buried less than 2.00 m deep with regular and irregular shapes, and vertical and horizontal layers simulating stratigraphic sequences. We selected materials similar to those commonly used since the Pre-Hispanic period (adobe, wood, basalt, tezontle), and current materials (concrete, reinforced concrete, plastic containers and PVC). Prior to the construction, the field area was characterized by a combination of non-invasive near-surface geophysical techniques including magnetic gradiometry, electromagnetic induction, ground penetrating radar, seismic refraction tomography and electrical resistivity tomography. The structures' physical properties (density, elastic modulus, electrical conductivity and magnetic susceptibility) and their geometrical characteristics are well known, therefore the near-surface geophysical response of the TGTS is controlled. The geophysical results indicate three flat interfaces at approximate depths of 0.45 m, 0.91 m and 1.82 m, respectively. The lithological analysis indicate that the layers are well graded coarse soil layers, including two volcanic hard-horizons (*repetates*). Geophysical results coincide with Teoloyucan's lithology, proving that the field area selected is suitable for a test site.

1. Introduction

Near-surface geophysical surveys encompass an ample range of methods and techniques whereby signals and fields observed at the Earth's surface (Lai et al., 2018) are used to map features in the subsurface. They are widely implemented in research in geology, sedimentology, hydrology, mining, permafrost, engineering, agriculture, forensic investigations, civil protection, archaeology and cultural heritage. Applied geophysical methods are selected depending on the particularities of each site and the objectives of the survey. The physical characteristics of the targets and the subsoil (e.g. mass, geometry, dimensions, depth, orientation, physical properties, porosity, moisture, salinity), the field and environmental conditions (e.g. vegetation,

climate, proximity of sources of noise, human activity) and the interaction between all these factors challenge the capabilities of the geophysical techniques (e.g. sensor type, sensibility, configuration, location with respect of the target, penetration, resolution), data processing methodologies and interpretation (Isaacson et al., 1999). All these characteristics determine the success or failure of an investigation. Not all techniques and methods are appropriate for all sites and work well under all ambient conditions. Therefore, the complexity to establish specific guidelines for any conjunction of factors makes the combination of geophysical techniques the best practice for target detection (Pringle et al., 2012), reducing uncertainties to some degree. Nevertheless, the final interpretation may need verification with direct methods such as drilling or digging. Some sites represent unique opportunities for

* Corresponding author.
E-mail address: arosadof@ciencias.unam.mx (A. Rosado-Fuentes).

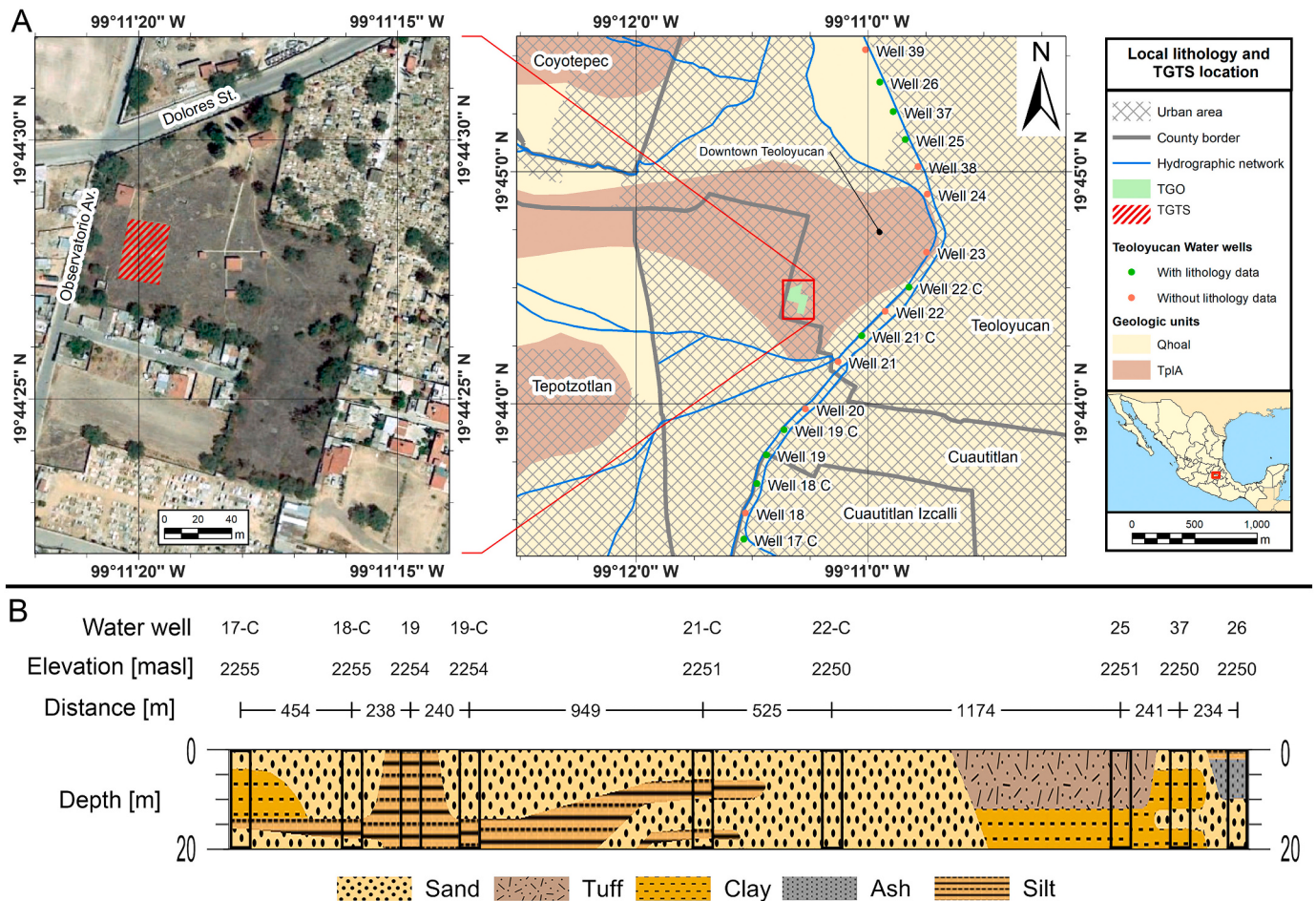


Fig. 1. A) Left panel shows Teoloyucan Geomagnetic Observatory (TGO) location and a zoom out of Teoloyucan Geophysical Test Site (TGTS). Right panel shows local lithology, the geologic units shown are andesite-dacite (TpIA) and alluvial (Qhaoal) from the Neogene and Quaternary, respectively. Teoloyucan's water wells located at less than 2.00 km from TGTS are indicated in green and red dots depending if there is lithology information available or not, respectively. B) Lithological profile of the first 20.00 m deep using data of the Teoloyucan water wells (CONAGUA) that are shown with green dots in panel A. (For interpretation of the references to colour in this figure legend, the reader is referred to the web version of this article.)

engineering, archaeology or cultural heritage, therefore detecting the underground features and estimating their depths is crucial. Thus, geophysical surveys provide economic, non-destructive and rapid tools to distinguish underground characteristics, saving resources.

Test sites are built to investigate the ground's geophysical response by targets of known attributes and properties in a certain environment. They are useful to validate geophysical methods (Lai et al., 2018), software, compare models with field measurements (Isaacson et al., 1999), test new technologies, sensors and arrays, calibrate the geophysical response of particular objects in certain environments and to design, optimize and integrate techniques. Moreover, test sites are ideal to train students and technicians in the use of geophysical methods, providing experience and expertise. Most test sites are designed to replicate and simulate a broad range of features commonly encountered in different fields of study and scenarios. Geotechnical sites like Montagnole test site, France, where structural experiments are carried out (Catapano et al., 2012) or the National Geotechnical Experimentation Sites of Texas A&M University, USA, for full scale testing structures (Briaud, 2000). Environmental test sites where steel and plastic drums were buried to simulate waste containers are found at the Sydney Basin test site, Australia (Emerson et al., 1992), and in Central Italy (Marchetti et al., 1998). The Laboratoire Central des Ponts et Chaussées test site, France (Grandjean et al., 2000), and the National Technical University of Athens, Greece, test site (Orfanos and Apostolopoulos, 2012) were designed to simulate urban contexts. In Illinois, USA, an exclusive

controlled archaeological test site was constructed (Isaacson et al., 1999). Forensic scenarios have also been simulated around the globe. Some examples include test sites by the Llano University, Colombia, in which simulated burials have been studied and monitored with different methods (Molina et al., 2016) and the test site by Keele University, UK, in which the effects of seasonal changes in climate and soil type were studied on simulated graves (Jervis and Pringle, 2014). Multi-purpose test sites designed for urban, geotechnical, archaeological and environmental contexts include the West Michigan University geophysical test site, USA (Sauck, 2009), the IAG/USP test site, Brazil (Porsani et al., 2006), and the shallow geophysical test site facility at the University of Leicester, UK (Cassidy et al., 2011). Even areas with little to no human activity or terrain alteration, where the geology and lithology are well known through previous historic, geophysical, geologic and drilling studies, can be designated as testing grounds. Examples include Nauen test site, Germany, for aquifer characterization (Yaramanci et al., 2002), Gypsy test site, USA, for reservoir characterization (Parra et al., 1996), Grimel test site, Switzerland, for radioactive waste disposal research (Buehnemann and Holliger, 1998), Bornheim test site, Germany, for local seismic response (Richwalski et al., 2007), and also Reid-Mahaffy (Reford and Fyon, 2000) and Cavendish (MacNae, 1980) test sites, Canada, for local and regional geological features.

To the best of our knowledge there are three test sites in Mexico that have been studied with different geophysical techniques. Two sites deal with engineering situations, one contains plastic and metal drums filled

with air and liquids located within the first 1.20 m deep (Blancas-Vázquez et al., 1996), the other has concrete, plastic and metal pipes situated at a maximum depth of 1.00 m (Gres-Hernández, 2010). The third site focuses on forensic research where the objects were buried in the first 1.40 m of the subsoil (Quiroz-Suárez, 2020). Teoloyucan Geophysical Test Site (TGTS) is designed to represent ground environments like those encountered in various engineering and archaeological contexts in Mexico. The structures' characteristics cover a range of features in geometry, stratigraphic sequences and material composition (Pre-Hispanic materials like adobe, wood, basalt, tezontle and current materials like concrete, reinforced concrete, plastic containers and PVC). In this work we first describe the site characterization by applying non-invasive near-surface geophysical techniques such as magnetic gradiometry, electromagnetic induction, ground penetrating radar, seismic refraction tomography and electrical resistivity tomography. Later, we describe how TGTS was designed and built, showing that it was quantitatively constructed controlling the spatial and material parameters (density, granulometry, elastic modules, electrical conductivity and magnetic susceptibility) of 17 structures buried at less than 2.00 m, aiming to control the near-surface geophysical response of the test site. Although the construction of the test site is completed and some geophysical methods have been applied to measure the geophysical response of the designed targets, these results will be part of further publications which are currently in preparation.

2. Regional geological settings

TGTS is located in a field area of 864.00 m² (24.00 m E by 36.00 m N) within the Teoloyucan Geomagnetic Observatory of the Universidad Nacional Autónoma de México (UNAM) in the town of Teoloyucan, N of Mexico City (Fig. 1A). Teoloyucan is situated N of the endorheic Valley of Mexico, in the 3870.00 km² NNW-NNE oriented Cuautitlán-Pachuca Aquifer (Huizar-Alvarez et al., 2003; Roy et al., 2010; SEMARNAT, 2016). The Aquifer has an average altitude of 2450 masl (Lafragua Contreras et al., 2003), a temperate semi-dry climate with an annual temperature ranging between 12 °C and 18 °C and an average annual precipitation of 578.55 mm (CONAGUA, 2002). The largest body of water is Lake Zumpango (Lafragua Contreras et al., 2003) and among the most important rivers are Tepozotlán, Tlalnepantla and Cuautitlán (CONAGUA, 2002; Galindo Castillo et al., 2011; Lafragua Contreras et al., 2003).

In Teoloyucan region, the carbonate rocks from the Quaternary and the volcano-clastic deposits since the Paleocene (Hernández-García and Huizar-Alvarez, 2003) have originated cumulative exogenous forms (e.g. foothills, alluvial and flood plains), erosive valleys, gullies and erosive-denudatory cirques of variable sizes and thickness that are interleaved and, for most of the Aquifer, covered by alluvial and lacustrine deposits (CONAGUA, 2002; Huizar-Alvarez et al., 2003) formed by gravel, sand, silt, clays, tuffs, sandstone and breccia (Hernández-García and Huizar-Alvarez, 2003; Huizar-Alvarez et al., 2003; Lafragua Contreras et al., 2003; Vázquez-Sánchez and Jaimes-Palomera, 1989). TGTS sits on top of a Neogene andesite-dacite unit (TpLA) from the Sierra de Tepoztlatán (SGM, 2002) surrounded by Quaternary alluvial deposits (Qhao), inside a 90.00 km long and 15.00 km wide graben limited by two SW-NE normal faults: Zumpango Norte and Tepoztlatán (Huizar-Alvarez et al., 2003). In 2010, the static water level of the Aquifer system in the region was between 70.00 m and 90.00 m deep (Galindo Castillo et al., 2011). Subsidence gradients can be observed (Siles et al., 2015) along the Teoloyucan water well system, found in alluvial deposits (Vázquez-Sánchez and Jaimes-Palomera, 1989) next to the Cuautitlán River (Fig. 1A).

Fig. 1B shows a lithological profile of the first 20.00 m of the subsoil generated with data from water wells located at less than 2.00 km from TGTS (Fig. 1A), data was provided by the Mexican National Water Commission (CONAGUA). The profile mostly presents alluvial or lacustrine sediments alternating between sand, clay and silt deposits

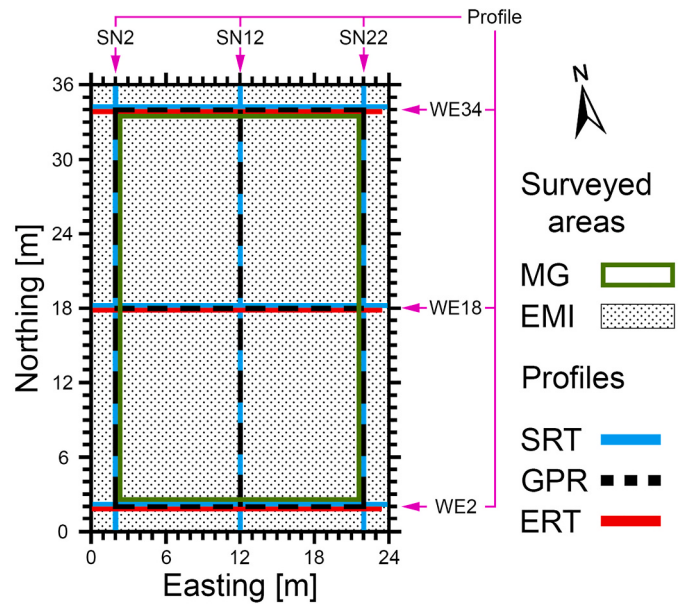


Fig. 2. Distribution of the magnetic gradiometry (MG, green box) and electromagnetic induction (EMI, black dotted area) surveyed areas and profiles for seismic refraction tomography (SRT, blue lines), electrical resistivity tomography (ERT, red lines) and ground penetrating radar (GPR, black dashed line). Profiles' names are also shown. The periphery (black solid line) is marked every 2.00 m with half-buried concrete cylinders of 0.15 m in diameter and 0.30 m in height. (For interpretation of the references to colour in this figure legend, the reader is referred to the web version of this article.)

that can extend to 280.00 m deep. Volcano-clastic sediments are present in the first 10.00 m deep according to well 25 as tuff and in well 26 as a pocket of ash of 8.00 m thick. This profile suggests that the N limit of unit TplA, N of downtown Teoloyucan (Fig. 1A), should be closer to water well 25; having a similar frontier with unit Qhao as shown in the S boundary of downtown Teoloyucan and Teoloyucan Geomagnetic Observatory (TGO). Other geological profiles elsewhere in the Aquifer can be consulted in Aguilar-Téllez et al. (2012), Carrera-Hernández and Gaskin (2007) and Roy et al. (2010).

At least the first 3.00 m of the subsoil of unit TplA in TGO is conformed by *tepetate*, term derived from the Nahuatl *tepetlatl*. It can be defined as a rock-like hard-consolidated horizon of volcanic origin. Indeed, Teoloyucan presents the geological and meteorological characteristics related to fine pyroclastic flows (Acevedo-Sandoval et al., 2003; Dubroeucq, 1992; Gama-Castro et al., 2007; Peña and Zebrowski, 1992; Quantin et al., 1993; Zebrowski, 1992). Tepetates have been reported elsewhere in America under different names (Peña and Zebrowski, 1992; Zebrowski, 1992) and are commonly associated with underlying or emerging soil or alluvium or colluvium deposits (Gama-Castro et al., 2007; Williams, 1972). The overlying sand-silt soil is formed by pyroclastic material, in some areas it has fragments of pottery and obsidian (Peña and Zebrowski, 1992; Quantin et al., 1993; Williams, 1972).

Tepetates are impervious to air, water and root growth. They vary in colour, from whitish gray to yellowish brown, and have a 13–24% porosity; although some authors have calculated it between 40% and 55%. Their matrix is a mixture of sand (22–82%), silt (9–42%), clay (25–54%), gravel, pumice, conglomerates and caliche; expanding the range of texture, structure and consistence. Their apparent density ranges from 1.2 g/cm³ to 1.9 g/cm³ and their real density from 2.4 g/cm³ to 2.8 g/cm³. Their resistance varies from 26 kg/cm² to 800 kg/cm². They are similar to rhyolites and rhyodacites, rich in silica and clays (Dubroeucq, 1992; Gama-Castro et al., 2007; Hidalgo et al., 1997; Peña and Zebrowski, 1992; Quantin et al., 1993; Williams, 1972).

3. Site description and geophysical characterization

TGO covers an irregular area of 2.10 ha, the geomagnetic sensors are located in the buildings at the center of the terrain. TGTS is in the W center portion of TGO (red striped area in Fig. 1A left), warehouses are close to its SW and NW corners. The area is flat and overgrown with grass and weed. TGTS is delimited every 2.00 m with half-buried concrete cylinders of 0.15 m in diameter and 0.30 m in height. The area was characterized to determine any subsurface anomaly with five non-invasive near-surface geophysical methods: magnetic gradiometry (MG), electromagnetic induction (EMI), ground penetrating radar (GPR), seismic refraction tomography (SRT) and electrical resistivity tomography (ERT). The results of the multi-geophysical data provided the basis to design and build the test site. The surveyed areas and profiles for each method are shown in Fig. 2 and explained in detail below.

3.1. Magnetic Gradiometry (MG)

The magnetic method measures the Earth's geomagnetic field as the sum of the principal field, the lithospheric field and the field generated by sources in the magnetosphere and ionosphere. Since the geomagnetic field's diurnal variation is random and irregular, the residual field can be obtained by a diurnal correction or applying the magnetic gradiometry (MG) method. This method consists in measuring simultaneously the Earth's magnetic field with two equal sensors with the same configuration but separated a certain distance from each other. The measurements can be obtained vertically or horizontally (Langel and Hinze, 1998; Telford et al., 1978).

In TGTS area we conducted an MG survey on March 24, 2017 using two Geometrics G-858 cesium vapor magnetometers oriented vertically and separated 1.00 m from each other, the lower sensor was in average 0.45 m from the ground surface. A mesh consisting of 18 N-S and 11 E-W transects separated every 2.00 m covered an area of 680.00 m² (20.00 m E by 34.00 m N, see green box in Fig. 2) preventing the effects of the concrete bodies that delimit the site. Measurements were taken approximately every 0.50 m, giving a total of 1445 points. The average value of the Kyoto Dst Geomagnetic Index, available from the World Data Center for Geomagnetism, Kyoto, Japan is -7.54 nT. The average value of the Postdam Kp Index, available from the Geo-ForschungsZentrum, Postdam, Germany, is 0.71 nT. Both indexes correspond to a quiet geomagnetic day, therefore there were no undesirable effects due to the natural field variations. TGO data indicates a total field diurnal variation of <2.00 nT during the prospection. After corrections, data was interpolated using the Kriging method (Haas and Viallix, 1976) and reduced to the magnetic pole.

3.2. Electromagnetic Induction (EMI)

Electromagnetic induction (EMI) is a controlled low-frequency domain method in which time-varying electromagnetic fields originated near the surface are induced into the subsurface according to induction phenomena. The EMI sensor features a transmitter and a receiver coil. A current flow in the transmitter coil generates a primary magnetic field which induces eddy currents in the soil, which induce a secondary magnetic field that is characterized by the target's geometry, position and electrical conductivity. Primary and secondary magnetic fields induce a current in the receiver coil that is corrected by removing the primary field, giving the normalized response function. Its real term is related to the magnetic susceptibility of the measured material, it is a relative quantity in parts per thousand (ppt) of the primary magnetic field and it is referred to as the in-phase signal since its time variation coincides with that of the transmitter's current. The imaginary part is referred to as the quadrature since its time variation is 90° out of phase with the transmitter's current, it is related to the apparent conductivity of the subsoil which is measured in Siemens per meter (S/m) (Everett, 2013; GF Instruments, 2020; Spies and Frischknecht, 1991). The target

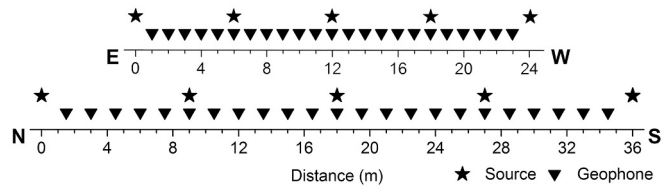


Fig. 3. W-E (top) and N-S (bottom) SRT profiles' geometry. Triangles and stars indicate the geophones and source-points locations, respectively.

depth range is determined by the frequencies used, the source-receiver distance and coil configuration with respect of the center of the array (GF Instruments, 2020; Spies and Frischknecht, 1991).

The EMI survey covered the full TGTS area (see black dotted area in Fig. 2) using two GF Instruments conductivity meters (CMD-2 and CMD-4) equipped with a differential GPS. The sensor measures apparent conductivity and the in-phase values simultaneously. CMD-2 and CMD-4 have a dipole distance of 1.89 m and 3.77 m and effective depth range of 1.50 m and 3.00 m, respectively (GF Instruments, 2020). The survey had vertical coplanar coil configuration (VCL or low mode) and sampling rate of 1 Hz following a N-S zig-zag path, starting in the NE corner of the site and moving W; sampling lines are separated every 2.00 m. This procedure was carried out with both instruments. Data processing includes removing incomplete acquisition points, averaging data from points with the same geographical coordinates, changing the units to mS/m and transforming data to TGTS relative coordinates (Northing and Easting); data was interpolated using Kriging method (Haas and Viallix, 1976).

3.3. Seismic Refraction Tomography (SRT)

Seismic refraction is based on Snell's Law, and Fermat's and Huygens' Principles. Data acquisition requires an active seismic source to generate elastic waves that travel from the source point to a geophone array distributed in the surface. The objectives of the study and the maximum depth of interest determine the distribution and geometry of the array. This method solves lateral and vertical velocity changes but assumes that P-wave velocity increases with depth and may not be sensible to low velocity layers or hidden layers between high velocity layers. The seismic inversion used consists in a non-linear least-squares scheme which calculates the ray path, travel times and slowness by minimizing the difference between the observed and calculated first arrival travel-time curves (Stein and Wysession, 2003; Telford et al., 1978). In this work, seismic data was processed by applying a 2D seismic refraction tomography (SRT).

For data acquisition we used a 48-channel Geometrics Stratavisor NZII seismograph and twenty-three 14-Hz natural frequency Oyo-Geospace vertical geophones. Three parallel 24.00 m long W-E profiles and three parallel 36.00 m long N-S profiles were set along the site (see blue lines in Fig. 2), with a geophone spacing of 1.00 m (Fig. 3 top) and 1.50 m (Fig. 3 bottom), respectively. Five source-points using an 8 kg sledgehammer vertically impacting on a ground-coupled steel plate were distributed along each profile (stars in Fig. 3). Five impacts were stacked per source-point to enhance the signal-to-noise ratio and the sampling rate was 0.125 ms. We evaluate the quality of the data with the principle of reciprocity by calculating the reciprocal travel-times for the first arrival travel-time curves. Then we applied the time-term inversion to generate a P-wave velocity (Vp) layered model. Later in the iterative tomographic inversion, the Vp model is meshed into cells of 8 nodes and width equal to the geophone spacing (Arciniega-Ceballos et al., 2009; Rosado-Fuentes and Arciniega-Ceballos, 2015; Stein and Wysession, 2003). The best Vp model is selected by analyzing the root-mean-square (RMS) values versus the number of iterations. This model corresponds to the first iteration whose difference with respect to the curve's trend is <5.0%.

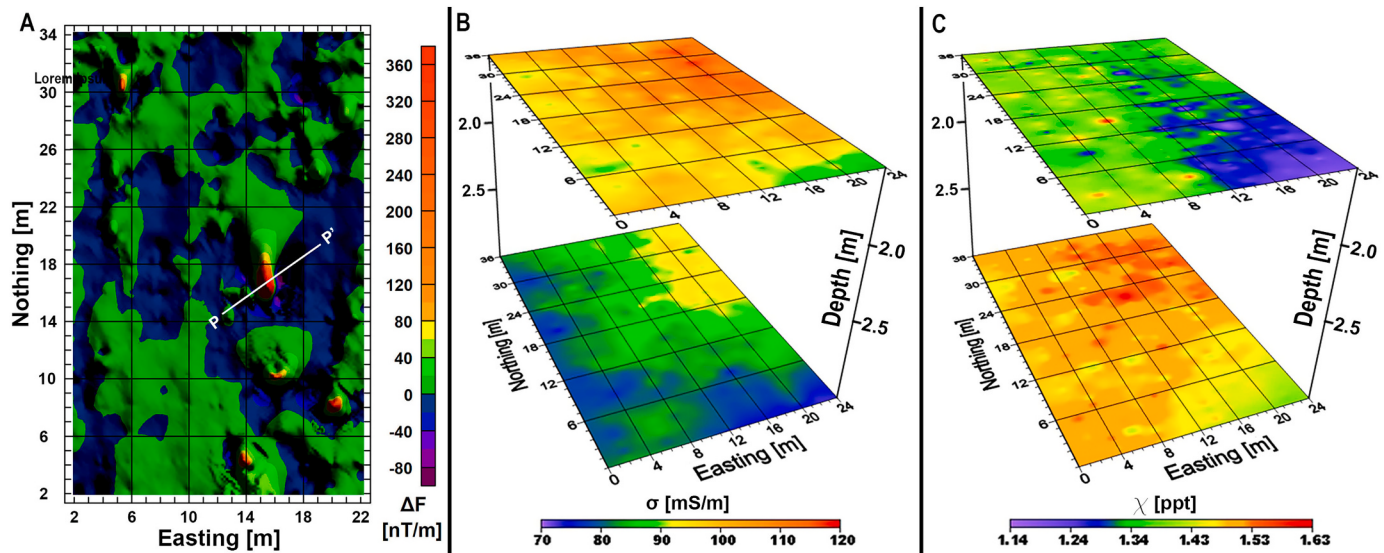


Fig. 4. TGTS' surveyed area maps for A) total gradient anomaly, B) electromagnetic conductivity and C) in-phase values. Colour bars in each panel indicate the corresponding parameter's value range. (For interpretation of the references to colour in this figure legend, the reader is referred to the web version of this article.)

The calculated reciprocal travel-times differences are below 3.5%. The RMS travel-time inversion error for a 2-layered initial model ranges between 0.30 ms and 0.92 ms. The tomographic inversion models were determined after 7–8 iterations, their RMS error in the range 0.36–0.80 ms.

3.4. Electrical Resistivity Tomography (ERT)

Electrical resistivity is based on Ohm's Law, a group of electrodes driven into the ground are used to inject an artificial direct electric current into the subsoil and to measure the resulting voltage. The impedance and a geometric factor that depends on the array are transformed into an apparent resistivity, an indicator of the actual electrical resistivity of the subsoil. A pseudo-section is obtained by alternating the current and potential electrodes along the array (Everett, 2013; Telford et al., 1978). In this work, data was processed by applying a 2D electrical resistivity tomography (ERT).

Field data is filtered to have a standard deviation of less than 0.20, this eliminates <5.0% of the measured points; bad data points are also eliminated. The pseudo-section is meshed into cells of 4 nodes and width equal to the electrode spacing to apply an iterative tomographic inversion technique based on a robust on the model least-squares scheme which calculates the resistivity values by minimizing the difference between the observed and calculated data. The best 2D resistivity model of the subsoil (Everett, 2013; Telford et al., 1978) is selected by analyzing the RMS values versus the number of iterations. This model corresponds to the first iteration whose RMS value difference with respect to the curve's trend is <5.0%.

The survey was carried out with an IRIS Instruments computer controlled multi-electrode Syscal Pro. Dipole-dipole data sets were acquired along three parallel E-W 23.50 m long profiles consisting of 47 ground-coupled electrodes separated every 0.50 m (see red lines in Fig. 2). Dipole-dipole is more sensitive to the regions beneath each dipole than regions between the dipoles and is highly sensitive to near-surface heterogeneities (Everett, 2013; Telford et al., 1978). Electrodes' contact resistance was below 1.0 Ω and current was injected for 1 s. The tomographic inversion models were determined after 5–6 iterations with a RMS error range of 0.87–1.23%.

3.5. Ground Penetrating Radar (GPR)

Ground penetrating radar is based on radio wave propagation from a

signal generator to a receiving antenna. The antenna scans the area of interest detecting changes in the electromagnetic (EM) impedance of the subsoil. The spatial distribution of the medium's electric properties and water content directly affect both the EM waves properties and the vertical penetration of the signal. The vertical resolution of this technique will depend on the sensibility to detect and differentiate two radar returns closely in time and on the emitted frequency of the signal (Everett, 2013; Jol, 2009).

The GPR survey was carried out using a 400 MHz shielded antenna controlled by a GSSI SIR 3000 console, both were mounted on a survey cart with an integrated survey wheel. Three parallel 32.00 m long N-S and three parallel 20.00 m W-E profiles were set along the site (see black dotted lines in Fig. 2). In this work data processing includes a time-zero correction, background-removal, filtering, deconvolution and gain. The filtering was done with a 100 MHz to 800 MHz band-pass finite impulse response filter (FIR) exhibiting phase linearity within this frequency range without signal distortion; AGC gain was conducted using a 12.00 ns time window (Everett, 2013; Jol, 2009). The three interfaces shown in the radargrams are used to perform a direct modeling that is later migrated. The layers, from the surface down, are assigned speeds of 0.05 m/ns, 0.09 m/ns and 1.00 m/ns and thicknesses of 0.30 m, 0.30 m and 0.50 m, respectively. The half-space has an assigned speed of 0.15 m/ns and starts at a depth of 1.10 m.

4. Geophysical results and interpretation

The geomagnetic gradient anomaly, EM conductivity and in-phase maps shows values ranging between 120.00 nT/m and 420.00 nT/m, 70.00–120.00 mS/m and 1.14–1.63 ppt, respectively (Fig. 4). The strongest magnetic dipole is centered at coordinates (Easting, Northing) = (16.00, 17.00) and is crossed by profile P-P' (Fig. 4a). The estimated depth, calculated using Tilburg's and Hansel's rules (Sheriff, 2002) and corrected by the distance between the ground and the lower sensor, are 0.22 m and 0.15 m, respectively. This area was excavated finding pieces of a metal drum that were removed from a depth of around 0.20 m, the difference between the real and estimated depths differ in ≤ 0.05 m. The upper EM conductivity layer has slightly higher values and the in-phase has moderately lower values than the deeper layer. The NE corner has the highest conductivity and in-phase values with ranges of 95.00–120.00 mS/m and 1.34–1.63 ppt, respectively. In contrast, the SE corner of the test site has relatively the lowest conductivity (Fig. 4b) and in-phase (Fig. 4c) values with ranges of 70.00–95.00 mS/m and

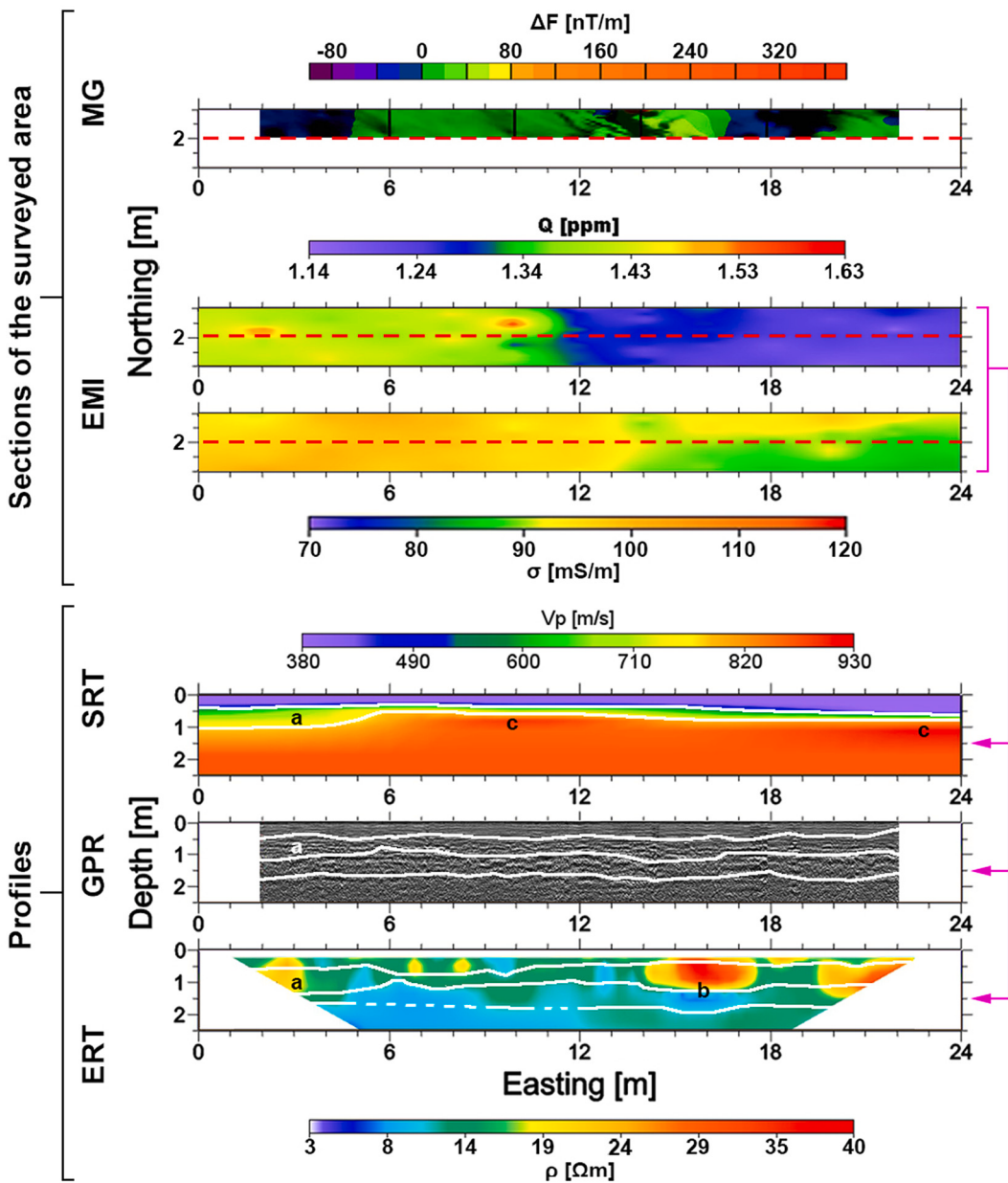


Fig. 5. Seismic refraction tomography (SRT), electrical resistivity tomography (ERT) and ground penetrating radar (GPR) profiles; and magnetic gradiometry (MG) and electromagnetic induction (EMI) sections along profile WE2. Red dotted lines on the EMI and MG sections of the surveyed areas indicate their intersection with ERT, GPR and SRT profiles. Purple lines and arrows indicate the depth of the intersection of the EMI section with the SRT, GPR and ERT profiles. White lines in the SRT, GPR and ERT results indicate layers' interfaces. Letters on SRT, GPR and ERT results indicate: a) depressions, b) electric resistivity dipoles and c) areas of maximum Vp. Colour bars in each panel indicate the measured parameter's value range. Location of the profiles is shown in Fig. 2. See text for details. (For interpretation of the references to colour in this figure legend, the reader is referred to the web version of this article.)

1.14–1.48 ppt, respectively. Isolated magnetic peaks are concentrated in the SE corner of the site as well and do not match the high in-phase values observed at either depths. These results indicate that TGTS does not present any magnetic trend nor strong EM anomalies and suggest that the magnetic peaks are originated by very shallow objects that most probably are pieces of garbage. Without considering the magnetic and in-phase peaks (see Fig. 4a and c), these results also suggest that the site is magnetically and electromagnetically smooth, i.e. no major anomalies will mask or contribute to the geophysical response of the buried targets in future studies.

Figs. 5 and 6 show ERT, SRT and GPR results of profiles WE2 and WE18, respectively (see Fig. 2); and their intersection with the EMI and MG survey results (Fig. 4). SRT images for TGTS indicate three flat layers with bumps whose Vp ranges from 380 m/s to 930 m/s. From the surface

down, the first two layers present average thicknesses of 0.50 m and 0.25 m, respectively. Their Vp ranges are 380–560 m/s and 560–750 m/s, respectively. The deepest layer starts at an average depth of 0.75 m and its Vp slightly increases from 750 to 930 m/s from the NW corner to the SE corner (see SRT profiles in Figs. 5 and 6). ERT and GPR images show that TGTS has four flat layers with bumps whose electric resistivity ranges from 3.0 Ωm to 40.0 Ωm. The first three layers show average thicknesses of 0.43 m, 0.56 m and 0.86 m, respectively; with electrical resistivity ranges per layer of 12.5–20.2 Ωm, 7.7–28.0 Ωm and 3.0–20.2 Ωm, respectively. The deepest layer starts around 1.85 m deep and its resistivity ranges from 3.0–12.5 Ωm (see ERT and GPR profiles in Figs. 5 and 6). SRT interfaces coincide with the first two ERT and GPR interfaces, their average depths are 0.45 m and 0.91 m. The deepest ERT and GPR interface, at 1.85 m deep in average, is not clear in the SRT

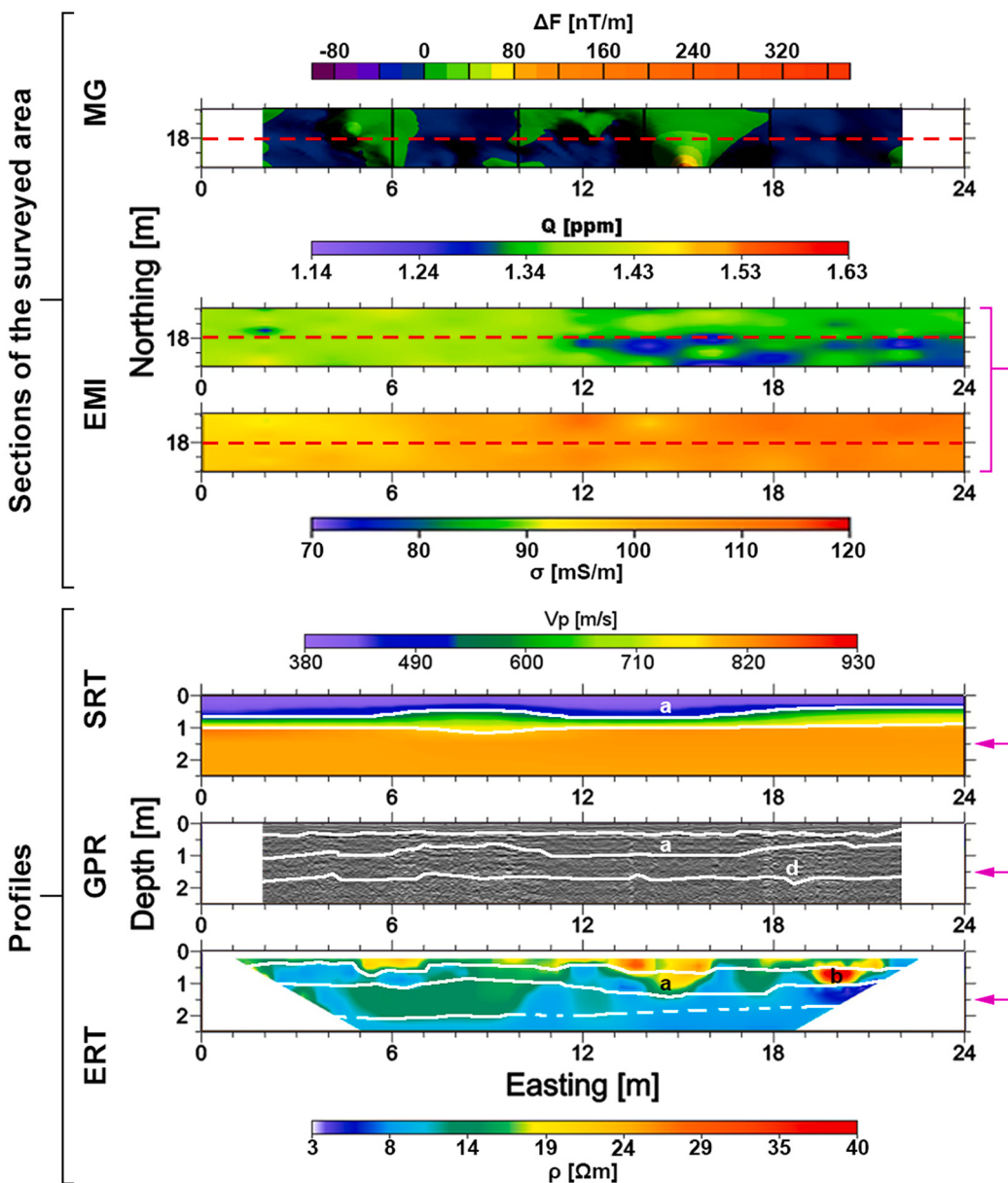


Fig. 6. Seismic refraction tomography (SRT), electrical resistivity tomography (ERT) and ground penetrating radar (GPR) profiles; and magnetic gradiometry (MG) and electromagnetic induction (EMI) sections of profile WE18. Red dotted lines on the EMI and MG sections of the surveyed areas indicate their intersection with ERT, GPR and SRT profiles. Purple lines and arrows indicate the depth of the intersection of the EMI section with the SRT, GPR and ERT profiles. White lines in the SRT, GPR and ERT profiles indicate layers' interfaces. Letters on SRT, GPR and ERT results indicate: a) depressions, b) electric resistivity dipoles and d) EM reflectors. Colour bars in each panel indicate the measured parameter's value range. Location of the profiles is shown in Fig. 2. See text for details. (For interpretation of the references to colour in this figure legend, the reader is referred to the web version of this article.)

images due to the low impedance contrast between contiguous layers (see Figs. 5 and 6). At 1.50 m deep the intersection between ERT (see Figs. 5 and 6) and EMI (Fig. 4b and c) results coincide, although conductivity values are not reciprocal to resistivity values. The discrepancy could be attributed to the physical principles of each method and the differences in the environmental conditions of the days in which the data were acquired.

SRT, ERT and GPR profiles show similar depressions of 6.50 m wide at 0.90 m deep, in average (see label a in Figs. 5 and 6). ERT results show four resistivity dipoles centered at an average depth of 1.40 m (see label b in Figs. 5 and 6). Next to these electric resistivity dipoles, GPR profiles' WE18 and WE32 show reflectors at an average depth of 1.14 m (see label d in Fig. 6). The maximum Vp values are embedded in the deepest SRT layer (see label c in Fig. 5). Our results indicate that the site presents

smooth distribution of geophysical properties without abrupt changes or discontinuities, making it ideal to build the test site and control the properties of the structures to be buried.

5. Construction and lithology of Teoloyucan Geophysical Test Site

Teoloyucan's soil is constituted mainly of hard *tepetate* that mechanically behaves as a duripan (Quentin et al., 1993). It does not break in water, it is hard to drill and compress and it bursts into fragments. We dug the 17 holes with a 0.50 m wide bucket backhoe, disturbing the surroundings as minimum as possible.

Fig. 7 show the location of the 17 structures that were built in situ, buried, leveled and oriented E-W. The holes were refilled and compacted

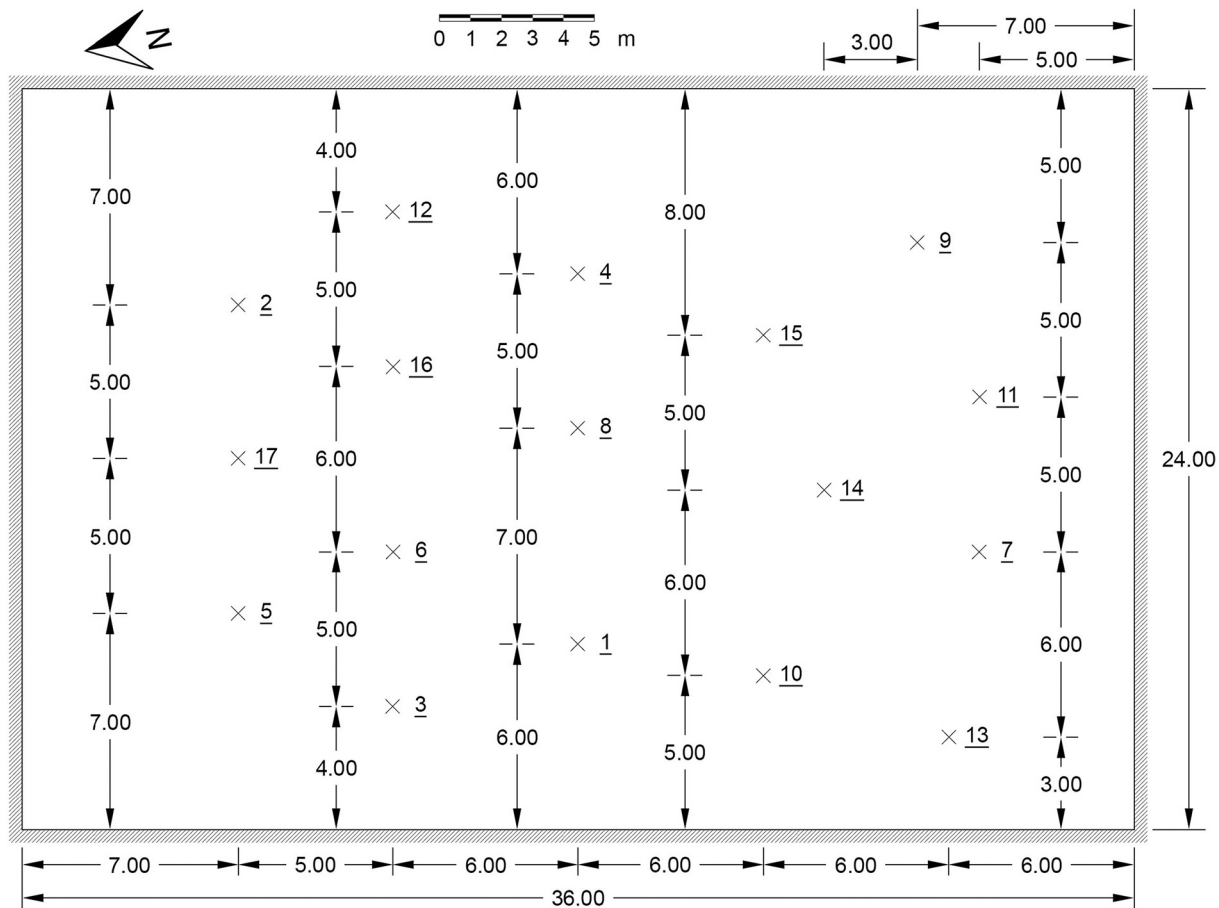


Fig. 7. Location of 17 buried structures denoted by underlined numbers. X-marks indicate the structure's center and the projection of the red dotted lines in Figs. 8 and 9. All units are in meters. (For interpretation of the references to colour in this figure legend, the reader is referred to the web version of this article.)

with the same material extracted during excavation; except for structure number 2 that was refilled with sand. We had strict control of the buried structures' location (Fig. 7), dimensions, depth and thickness of the material above each structure (Figs. 8 and 9). Structures from 1 to 8 are cubes made of concrete, basalt, tezontle, brick, wood and adobe (Fig. 8). Structure number 1, made of reinforced concrete, is the only one including metal parts (Fig. 8). Two square plastic containers simulate a void (structure 9 in Fig. 8) and a liquid cavity that can be refilled or changed through a tube connected to its lid (structure 10 in Fig. 8). Three cylindrical structures were built, one made of concrete (structure 11 in Fig. 9) and two are sealed PVC pipes (structures 12 and 13 in Fig. 9). Structures 14 and 15 simulate horizontal and vertical stratigraphic sequences, respectively; both were built using cubic structures made of the materials mentioned above (Fig. 9). Structures 16 and 17 have irregular shapes made of concrete (Fig. 9). Geophysical studies on TGTS should consider the resulting geophysical anomalies as a superposition effect of the structures, their holes and the refilled material. It is important to consider that the interpretation of the resulting anomalies could reflect the digging and refilling of the holes in some degree, depending on the characteristics of the buried structures. However, our data show negligible effects, which will diminish with time.

We generated TGTS's lithological section (Fig. 10 top left) with our results of the particle size analysis (Fig. 11) of 19 soil samples taken from the holes of structures 2, 8 and 13 (Fig. 7). Fig. 11 shows the statistical parameters calculated for each sample's sediment cumulative frequency curve following Inman's equations Inman (1952), using the Phi (Φ) transformation introduced by Krumbein Krumbein (1936), and the Wentworth size class Wentworth (1922). Parameters include the Phi mean diameter (M_Φ), Phi median diameter ($M_{d\Phi}$), Phi standard

deviation (σ_Φ), Phi skewness (α_Φ), 2nd Phi skewness ($\alpha_{2\Phi}$) and Phi kurtosis (β_Φ). These parameters consider the entire distribution correlating and differentiating between layers and sediment types (Inman, 1952). We used the standard deviation equation established by Folk and Ward Folk and Ward (1957) to determine samples' sorting. Vesicularity index was obtained by Houghton and Wilson's method Houghton and Wilson (1989) using a dense-rock equivalent density value of 2.50 g/cm³ (Fig. 10 bottom). Skewness values corroborate the resemblance to normal distributions, while kurtosis values reflect leptokurtic distributions.

The average density and vesicularity index distributions shown in the bottom panel of Fig. 10 and the grain size distribution curves and statistical parameters shown in Fig. 11 determine that TGTS is composed by three main well graded coarse soil layers. Their average thickness, density, vesicularity and percentage composition is shown in Table 1. From the surface down, the first layer is a poorly sorted coarse sand soil with roots. During construction of the test site fragments of pottery, worked obsidian and gastropods shells were recovered from this layer (Fig. 10 top right). The second layer is a poorly to very poorly sorted fine gravel transition layer composed by a beige *tepetate* mixed slightly with soil, named soil-*tepetate*; it has thin roots and occasionally seems laminated and whitish. The third layer is a beige to brown poorly sorted, coarse sand to fine gravel *tepetate*. Profile 13 suggests that, at least, the SW corner of the test site has an additional well graded coarse soil layer at the bottom composed by a poorly sorted medium sand dark brown *tepetate* easier to remove.

Most likely, both *tepetates* described in the sequence (Fig. 10) originated by pyroclastic materials from the Sierra de Tepotzotlán. Their percentage composition does not match those obtained in other studies

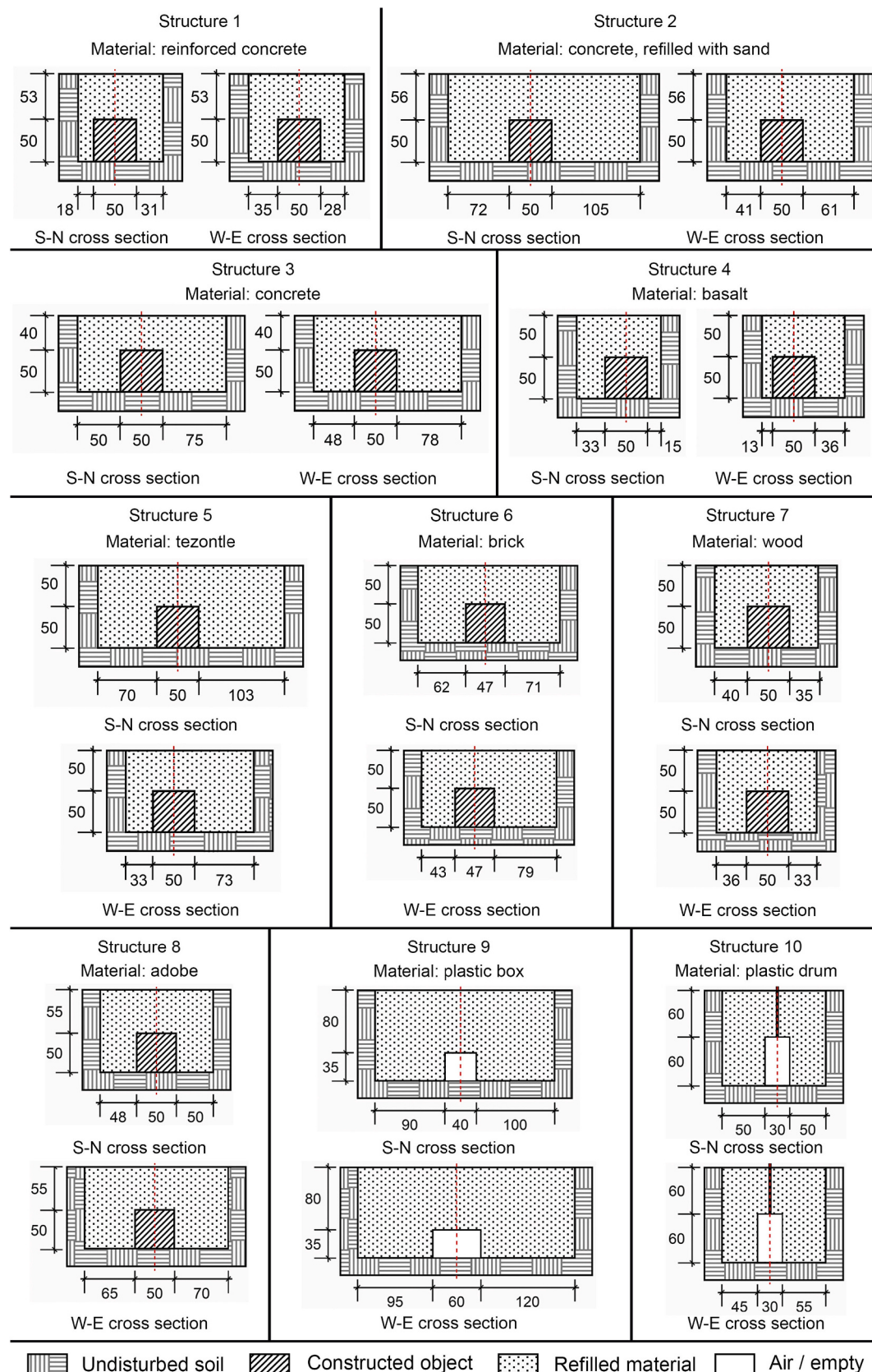


Fig. 8. N-S and W-E cross-sections of buried structures 1 to 10, their identification number is indicated at the top of each drawing. The red dotted line indicates the vertical projection of the center of the buried structures, shown with x-marks in Fig. 7, and the intersection of the cross-sections. All dimensions are in centimeters. (For interpretation of the references to colour in this figure legend, the reader is referred to the web version of this article.)

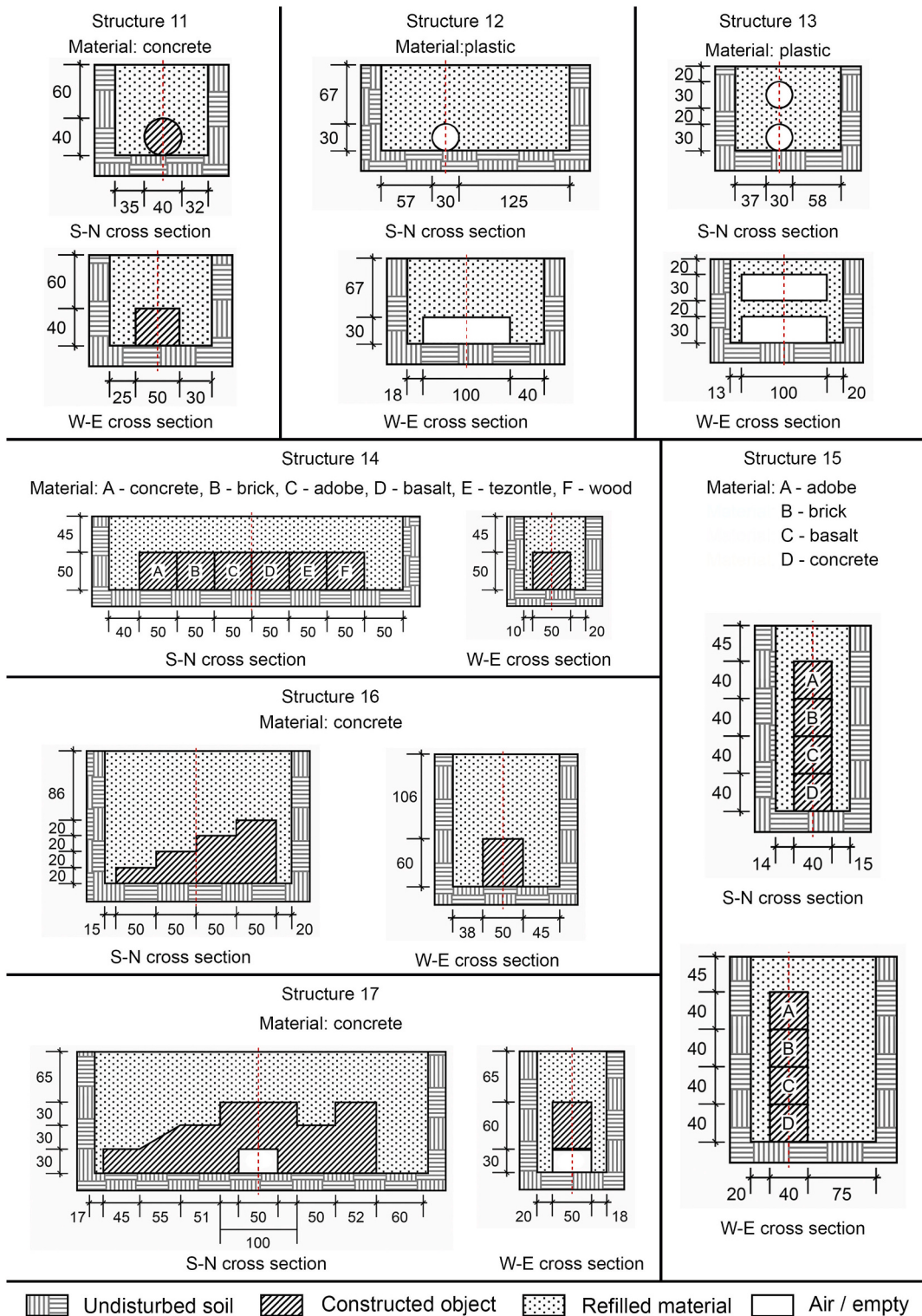


Fig. 9. N-S and W-E cross-sections of buried structures 11 to 17, their identification number is indicated at the top of each drawing. The red dotted line indicates the vertical projection of the center of the buried structures, shown with x-marks in Fig. 7, and the intersection of the cross-sections. All dimensions are in centimeters. (For interpretation of the references to colour in this figure legend, the reader is referred to the web version of this article.)

(Peña and Zebrowski, 1992; Quantin et al., 1993; Williams, 1972), except for the sand range of the beige to brown *tepetate*. Also, their apparent density is slightly below the range observed in other studies (Peña and Zebrowski, 1992; Quantin et al., 1993). These differences are attributed to the site's location, origin and environment. The first lithological interface is too shallow (Table 1) and it is not observed in the

geophysical results (Fig. 10 top left and Figs. 5 and 6). Considering the average depths, the second and third lithological interfaces (Table 1) coincide with the first and second geophysical interfaces (Figs. 5 and 6). These results indicate that the dark brown *tepetate* layer is not exclusive to the SW corner of the site, but rather sits deeper than the depths reached in lithological profiles 2 and 8. The third geophysical interface

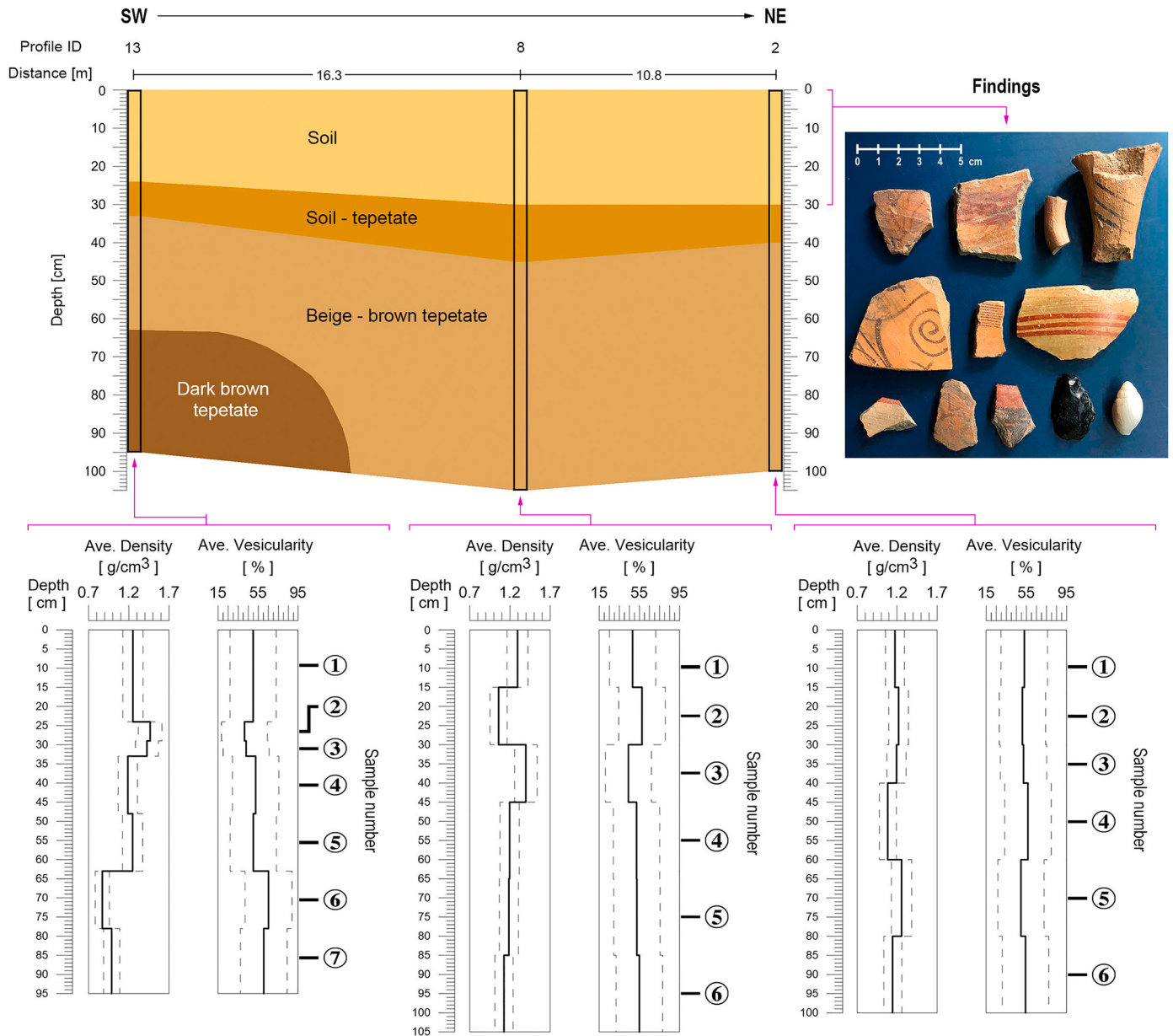


Fig. 10. Top left panel shows TGTS's lithological section along lithological profiles P13, P8 and P2; corresponding to the holes of buried structures 13, 8 and 2, see Fig. 7 for their location. Top right panel presents examples of pottery fragments, worked obsidian and gastropods' shells, recovered from the soil layer at different points along TGTS area during the construction of the test site. Bottom panels are the corresponding vertical profiles of holes 13, 8 and 2 versus its average density and vesicularity index distributions. The numbers in circle at the right indicate the samples' identification number, the vertical axis is depth in cm. Purple arrows indicate the position of each profile in the lithological section at the top left panel. (For interpretation of the references to colour in this figure legend, the reader is referred to the web version of this article.)

is also situated deeper than the depths reached by the lithological profiles.

6. Conclusions

Teoloyucan Geophysical Test Site (TGTS) is situated within Teoloyucan Geomagnetic Observatory, UNAM, Central Mexico. TGTS is meant to calibrate instruments, prove near-surface geophysical techniques, train students and investigate new ideas for near-surface surveys and data interpretation in archaeological and engineering contexts. We characterized and evaluated the area of 864.00 m² by applying five non-invasive near-surface geophysical techniques: magnetic gradiometry, electromagnetic induction, ground penetrating radar, seismic refraction tomography and electrical resistivity tomography. TGTS geophysical

results show smooth magnetic and EM properties, some isolated anomalies are attributed to very shallow garbage debris. TGTS is characterized by four flat layers with slight bumps. The E section of the site presents most of the isolated magnetic peaks, the electrical resistivity dipoles, the highest seismic velocities, the electrical reflectors and an alteration of the electromagnetic parameters (Figs. 4–6).

TGTS lithological section shows that the test site is composed of four main well graded coarse soil layers named: soil, soil-tepetate, beige to brown tepetate and dark brown tepetate. The tepetate originated by pyroclastic material from the Sierra de Tepotzotlán. The layers composition ranges, expressed in percentage, as well as the average density and vesicularity do not match the ranges mentioned in other studies (Peña and Zebrowski, 1992; Quantin et al., 1993; Williams, 1972). However, the grain size analysis is consistent with the lithological section (Fig. 10

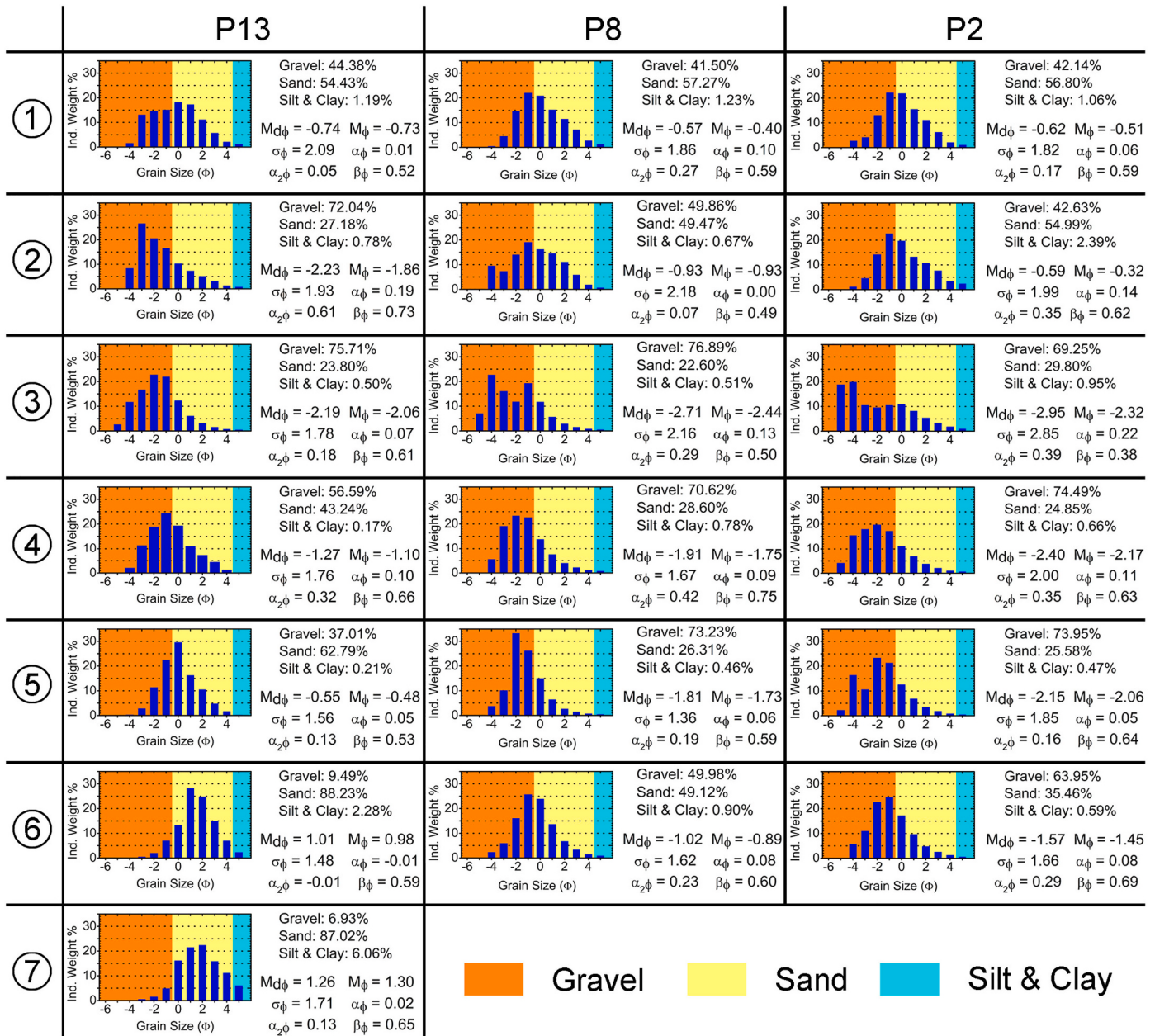


Fig. 11. Grain size distribution curves and statistical parameters for each sample taken on lithological profiles P13, P8 and P2; these correspond to the holes of buried structures 13, 8 and 2. Profiles' location and samples' depths are depicted in Figs. 7 and 10 bottom, respectively. Statistical parameters include Phi mean diameter (M_ϕ), Phi median diameter (Md_ϕ), Phi standard deviation (σ_ϕ), Phi skewness (α_ϕ), 2nd Phi skewness ($\alpha_{2\phi}$) and Phi kurtosis (β_ϕ).

Table 1
Average thickness, density and vesicularity, and percentage composition of TGTS lithological layers.

Layer name	Avg thickness [cm]	Avg density [g/cm^3]	Avg vesicularity [%]	Composition [%]		
				Gravel	Sand	Silt & clay
Soil	26.0	1.20 ± 0.12	51.98 ± 23.06	41–50	49–58	< 3
Soil - tepetate	13.0	1.37 ± 0.14	45.18 ± 22.91	69–77	22–30	< 1
Beige - brown tepetate	51.0	1.18 ± 0.12	52.84 ± 23.07	37–75	24–63	< 1
Dark brown tepetate ^a	32.0 ^a	0.93 ± 0.09	62.90 ± 23.31	6–10	87–89	< 7

^a The dark brown tepetate is only seen in profile 17, its average thickness is to the bottom of the profile.

top left panel), allowing to characterize the layers lithology which coincide with the geophysical results (Figs. 4–6). Therefore, these lithological ranges can be considered as references for other studies on tepetates elsewhere.

Geophysical results do not observe the first lithological interface

situated at an average depth of 0.26 m. The first and second geophysical interfaces coincide with the second and third lithological interfaces at average depths of 0.44 m and 0.91 m, respectively. The third geophysical interface sits below the depths reached by the lithological profiles, at an average depth of 1.85 m. In general, the combination of the

geophysical and lithological results were the bases for the construction of TGTS. Given that there are no abrupt changes, discontinuities or anomalies on the distribution of geophysical properties (MAG and EMI results, see Fig. 4, SRT, GPR, ERT results, see Figs. 5 and 6), Teoloyucan area is ideal for the construction of the test site. The smooth distribution of the geophysical properties set the reference measurements to discard undesirable effects on the geophysical response of the targets in future studies. Therefore, we prevented that the materials' properties of the 17 buried structures (<2.00 m deep) with different geometries have significant contrast with the surrounding soil (Figs. 7–9). The site is now available for academic research, education and industry purposes; previous request to the authors and the Institute of Geophysics, UNAM. Ongoing studies include the application of the same geophysical techniques to compare the response of the field with the buried structures.

Data availability

Datasets related to this article are available under request to the authors.

Declaration of Competing Interest

The authors declare that they have no known competing financial interests or personal relationships that could have appeared to influence the work reported in this paper.

Acknowledgements

The authors acknowledge the Instituto de Geofísica, UNAM for supporting this idea and allowing us to build the TGTS within the Teoloyucan Geomagnetic Observatory. We also thank Walter Antonio Flores García for his support in the field campaigns and technical advice, CONAGUA for providing the water well's lithological data and Jesús Ancira for his support during the site's construction. We also appreciate the substantial support given by the UNAM DGAPA-PAPIIT project IN105716. Alejandro Rosado-Fuentes thanks CONACYT (620517/336033) and UNAM DGAPA-PAPIIT project IN108219 for the scholarships provided and the Posgrado en Ciencias de la Tierra and Grupo MARQ for their support.

References

- Acevedo-Sandoval, O.A., Ortiz-Hernández, L.E., Flores-Román, D., Velásquez-Rodríguez, A.S., Flores-Castro, K., 2003. Caracterización física y química de horizontes endurecidos (tepetates) en suelos de origen volcánico del Estado de México. *Agrociencia* 37 (5), 435–449. <https://www.agrociencia-colpos.mx/index.php/agrociencia/article/view/272>.
- AgUILAR-Téllez, M.A., Rangel-Núñez, J.L., Comulada-Simpson, M., Auvinet-Guichard, G., Méndez-Marroquín, R., Maidl, U., 2012. Mexico City deep eastern drainage tunnel. In: Viggiani, G. (Ed.), *Geotechnical Aspects of Underground Construction in Soft Ground*, 1. Taylor & Francis Group. CRC Press, London, pp. 175–191. <https://doi.org/10.1201/b12748>.
- Arcevina-Ceballos, A., Hernandez-Quintero, E., Cabral-Cano, E., Morett-Alatorre, L., Diaz-Molina, O., Soler-Arechalde, A., Chavez-Segura, R., 2009. Shallow geophysical survey at the archaeological site of San Miguel Tocula, Basin of Mexico. *J. Archaeol. Sci.* 36 (6), 1199–1205. <https://doi.org/10.1016/j.jas.2009.01.025>.
- Blancas-Vázquez, J.E., Cortés-Ávila, F.J., Gómez-Vázquez, M., Alariste-Vilchis, D.R., 1996. Adquisición y Procesamiento de Datos de GPR en un Campo de Pruebas. In: VII Simposium de Geofísica y Exposición. Asociación Mexicana de Geofísicos de Exploración, Mexico, pp. 281–288. In: https://www.researchgate.net/publication/309922811_Adquisicion_y_Procesamiento_de_Datos_de_GPR_en_un_Campo_de_Pruuebas.
- Briaud, J.L., 2000. The national geotechnical experimentation sites at Texas A&M University: clay and sand. In: Benoit, J., Lutenegger, A.J. (Eds.), *National Geotechnical Experimentation Sites*, Geotechnical Special Publication, 93. American Society of Civil Engineers, pp. 26–51. <https://doi.org/10.1061/9780784404843.ch02>.
- Buehnemann, J., Holliger, K., 1998. Comparison of high-frequency seismic sources at the Grimsel test site, Central Alps, Switzerland. *Geophysics* 63 (4), 1363–1370. <https://doi.org/10.1190/1.1444438>.
- Carrera-Hernández, J.J., Gaskin, S.J., 2007. The Basin of Mexico aquifer system: regional groundwater level dynamics and database development. *Hydrogeol. J.* 15 (8), 1577–1590. <https://doi.org/10.1007/s10040-007-0194-9>.
- Cassidy, N.J., Eddies, R., Dods, S., 2011. Void detection beneath reinforced concrete sections: The practical application of ground-penetrating radar and ultrasonic techniques. *J. Appl. Geophys.* 74 (4), 263–276. <https://doi.org/10.1016/j.jappgeo.2011.06.003>.
- Catapano, I., Di Napoli, R., Soldovieri, F., Bavusi, M., Lopez, A., Dumoulin, J., 2012. Structural monitoring via microwave tomography-enhanced GPR: the Montagnole test site. *J. Geophys. Eng.* 9 (4), S100–S107. <https://doi.org/10.1088/1742-2132/9/4/S100>.
- CONAGUA, 2002. Determinación de la Disponibilidad de Agua en el Acuífero Cuauitlán-Pachuca en los Estados de México e Hidalgo. Comisión Nacional del Agua, Mexico. <https://www.gob.mx/conagua>.
- Dubroeuq, D., 1992. Los tepetates de la región de Xalapa, Veracruz (México): un endurecimiento de origen pedológico. *Terra* 10, 233–240. <https://www.documentation.ird.fr/hor/fdi:38573>.
- Emerson, D.W., Reid, J.E., Clark, D.A., Manning, P.B., 1992. The geophysical responses of buried drums – field tests in weathered Hawkesbury Sandstone, Sydney Basin, NSW. *Explor. Geophys.* 23 (4), 589–617. <https://doi.org/10.1071/EG992589>.
- Everett, M.E., 2013. Near-Surface Applied Geophysics. Cambridge University Press, UK. <https://doi.org/10.1017/CBO9781139084353>.
- Folk, R.L., Ward, W.C., 1957. Brazos River bar [Texas]; a study in the significance of grain size parameters. *J. Sediment. Res.* 27 (1), 3–26. <https://doi.org/10.1306/74D70646-2821-11D7-8648000102C1865D>.
- Galindo Castillo, E., Otazo Sánchez, E.M., Gordillo Martínez, A.J., Arellano Islas, S., González Ramírez, C.A., Reyes Gutiérrez, L.R., 2011. Sobrexplotación del acuífero Cuauitlán-Pachuca: balance hídrico 1990–2010. In: *Avances en Impacto, Tecnología y Toxicología Ambiental*, 1st ed. Universidad Autónoma del Estado de Hidalgo, Hidalgo, pp. 9–32. <https://repository.uaeh.edu.mx/bitstream/handle/123456789/11454>.
- Gama-Castro, J., Solleiro-Rebolledo, E., Flores-Román, D., Sedov, S., Cabadas-Báez, H., Díaz-Ortega, J., 2007. Los tepetates y su dinámica sobre la degradación y el riesgo ambiental: el caso del Glacis de Buenavista, Morelos. *Bol. Soc. Geol. Mex.* 59 (1), 133–145. <https://doi.org/10.18268/bsgm2007v59n1a11>.
- GF Instruments, 2020. Short Guide for Electromagnetic Conductivity Mapping and Tomography. Retrieved from. <http://www.gfinstruments.cz> (last consulted June 5, 2020).
- Grandjean, G., Gourry, J.C., Bitri, A., 2000. Evaluation of GPR techniques for civil engineering applications: study on a test site. *J. Appl. Geophys.* 45 (3), 141–156. [https://doi.org/10.1016/S0926-9851\(00\)00021-5](https://doi.org/10.1016/S0926-9851(00)00021-5).
- Gres-Hernández, G., 2010. Análisis de Espectrogramas de Anomalías Magnéticas Para la Detección de Estructuras. [Bachelor's Thesis, Universidad Nacional Autónoma de México]. https://ru.dgb.unam.mx/handle/DGB_UNAM/TES01000655376.
- Haas, A.G., Viallix, J.R., 1976. Krigage applied to geophysics: the answer to the problem of estimates and contouring. *Geophys. Prospect.* 24 (1), 49–69. <https://doi.org/10.1111/j.1365-2478.1976.tb00384.x>.
- Hernández-García, G., Huizar-Alvarez, R., 2003. Groundwater abstraction in the Zumpango-Pachuca region, Central Mexico, and its environmental effects. *Mater. Geoenviron.* 50 (1), 141–144. http://www.rmj-mg.com/letniki/rmz50/rmz50_01_41-0144.pdf.
- Hidalgo, C., Quantin, P., Elsass, F., 1997. Caracterización mineralógica de los tepetates tipo fragipán del Valle de México. In: Zembrowski, C., Quantin, P., Trujillo, G. (Eds.), *Memorias del III Simposio Internacional: Suelos Volcánicos y Endurecidos*. ORSTOM, Quito, Ecuador, pp. 62–72. <https://www.documentation.ird.fr/hor/fdi:010012913>.
- Houghton, B.F., Wilson, C.J.N., 1989. A vesicularity index for pyroclastic deposits. *Bull. Volcanol.* 51 (6), 451–462. <https://doi.org/10.1007/BF01078811>.
- Huizar-Alvarez, R., Hernández, G., Carrillo-Martinez, M., Carrillo-Rivera, J., Hergt, T., Angeles, G., 2003. Geologic structure and groundwater flow in the Pachuca-Zumpango sub-basin, Central Mexico. *Environ. Geol.* 43 (4), 385–399. <https://doi.org/10.1007/s00254-002-0654-4>.
- Inman, D.L., 1952. Measures for describing the size distribution of sediments. *J. Sediment. Res.* 22 (3), 125–145. <https://doi.org/10.1306/D42694DB-2B26-11D7-8648000102C1865D>.
- Isaacson, J., Hollinger, R.E., Gundrum, D., Baird, J., 1999. A Controlled Archaeological Test Site Facility in Illinois: Training and Research in Archaeogeophysics. *J. Field Archaeol.* 26 (2), 227–236. <https://doi.org/10.1179/jfa.1999.26.2.227>.
- Jervis, J.R., Pringle, J.K., 2014. A study of the effect of seasonal climatic factors on the electrical resistivity response of three experimental graves. *J. Appl. Geophys.* 108, 53–60. <https://doi.org/10.1016/j.jappgeo.2014.06.008>.
- Jol, H.M. (Ed.), 2009. *Ground Penetrating Radar Theory and Applications*. Elsevier, The Netherlands. <https://doi.org/10.1016/B978-0-444-53348-7.X0001-4>.
- Krumbein, W.C., 1936. Application of logarithmic moments to size-frequency distributions of sediments. *J. Sediment. Res.* 6 (1), 35–47. <https://doi.org/10.1306/D4268F59-2B26-11D7-8648000102C1865D>.
- Lafraguia Contreras, J., Gutiérrez López, A., Aguilar Garduño, E., Aparicio Mijares, J., Mejía Zermeno, R., Sánchez Díaz, L.F., 2003. Balance Hídrico en la Cuenca de México, Informe Final. Instituto Mexicano de Tecnología del Agua, Secretaría de Medio Ambiente y Recursos Naturales, Mexico. <http://cenca.imta.mx>.
- Lai, W.W.L., Derobert, X., Annan, P., 2018. A review of Ground Penetrating Radar application in civil engineering: a 30-year journey from Locating and Testing to Imaging and Diagnosis. *Ndt & E Int.* 96, 58–78. <https://doi.org/10.1016/j.ndteint.2017.04.002>.
- Langel, R.A., Hinze, W.J., 1998. *The Magnetic Field of the Earth's Lithosphere: the Satellite Perspective*. Cambridge University Press, USA. <https://doi.org/10.1017/CBO9780511629549>.

- MacNae, J.C., 1980. The Cavendish Test Site: A UTEM Survey Plus a Compilation of Other Ground Geophysical Data. Research in Applied Geophysics, No. 12, University of Toronto, Canada. Retrieved from. <https://hdl.handle.net/1807/71941>.
- Marchetti, M., Chiappini, M., Meloni, A., 1998. A test site for the magnetic detection of buried steel drums. *Ann. Geofis.* 41 (3), 491–498. <https://doi.org/10.4401/ag-4355>.
- Molina, C.M., Pringle, J.K., Saumett, M., Evans, G.T., 2016. Geophysical monitoring of simulated graves with resistivity, magnetic susceptibility, conductivity and GPR in Colombia, South America. *Forensic Sci. Int.* 261, 106–115. <https://doi.org/10.1016/j.forsciint.2016.02.009>.
- Orfanos, C., Apostolopoulos, G., 2012. Analysis of different geophysical methods in the detection of an underground opening at a controlled test site. *J. Balk. Geophys. Soc.* 15 (1), 7–18. http://www.balkangeophysoc.gr/online-journal/2012_V15/No_1_March/JBGS_Vol_15_No1_March_2012_p07-18_Orfanos.pdf.
- Parra, J.O., Zook, B.J., Collier, H.A., 1996. Interwell seismic logging for formation continuity at the Gypsy test site, Oklahoma. *J. Appl. Geophys.* 35 (1), 45–62. [https://doi.org/10.1016/0926-9851\(96\)00003-1](https://doi.org/10.1016/0926-9851(96)00003-1).
- Peña, D., Zebrowski, C., 1992. Estudio de los suelos volcánicos endurecidos de las cuencas de México y Tlaxcala. In: Informe del Mapa Morfopedológico de la Vertiente Occidental de la Sierra Nevada. Commission des Communautés Européennes, Paris, pp. 1–98. <https://www.documentation.ird.fr/hor/fdi:38540>.
- Porsani, J.L., Borges, W.R., Rodrigues, S.I., Hiodo, F.Y., 2006. O sítio controlado de geofísica rasa do IAG/USP: Instalação e resultados GPR 2D-3D. *Revista Brasileira de Geofísica* 24 (1), 49–61. <https://doi.org/10.1590/S0102-261X2006000100004>.
- Pringle, J.K., Ruffell, A., Jervis, J.R., Donnelly, L., McKinley, J., Hansen, J., Morgan, R., Pirrie, D., Harrison, M., 2012. The use of geoscience methods for terrestrial forensic searches. *Earth Sci. Rev.* 114 (1–2), 108–123. <https://doi.org/10.1016/j.earscirev.2012.05.006>.
- Quantin, P., Arias, A., Etchevers, J., Ferrera, R., Oleschko, K., Navarro, A., Werner, G., Zebrowski, C., 1993. Tepeates de México: caracterización y habilitación para la agricultura. *Terra* 11, 75. <https://www.documentation.ird.fr/hor/fdi:010012241>.
- Quiroz-Suárez, D., 2020. *Métodos de exploración geofísica somera aplicados para la caracterización de inhumaciones: caso experimental y real* [Master's thesis, Universidad Nacional Autónoma de México]. http://132.248.9.195/ptd2020/octubre/08040_52/Index.html.
- Reford, S.W., Fyon, A., 2000. Airborne Magnetic and Electromagnetic Surveys, Reid-Mahaffy Airborne Geophysical Test Site Survey, Miscellaneous Release - Data (MRD) 55. Geological Setting, Measured and Processed Data, and Derived Products: Ontario Geological Survey, Canada. Retrieved from. http://www.geologyontario.mndm.gov.on.ca/mndmaccess/mndm_dir.asp?type=pub&id=MRD055.
- Richwalski, S.M., Picozzi, M., Parolai, S., Milkereit, C., Baliva, F., Albarello, D., Roy-Chowdhury, K., van der Meer, H., Zschau, J., 2007. Rayleigh wave dispersion curves from seismological and engineering-geotechnical methods: a comparison at the Bornheim test site (Germany). *J. Geophys. Eng.* 4 (4), 349–361. <https://doi.org/10.1088/1742-2132/4/4/001>.
- Rosado-Fuentes, A., Arciniega-Ceballos, A., 2015. Archaeological prospection in Chapingo, Texcoco Region, Mexico. *Revista Geofísica* 65, 89–105. <https://www.revistasipn.org/index.php/regeofi/article/view/255>.
- Roy, P.D., Morton-Bermea, O., Hernández-Álvarez, E., Pi, T., Lozano, R., 2010. Rare earth element geochemistry of the late Quaternary tephra and volcano-clastic sediments from the Pachuca sub-basin, north-eastern basin of Mexico. *Geofis. Int.* 49 (1), 3–15. <http://www.revistas.unam.mx/index.php/geofisica/article/view/40126>.
- Sauck, W., 2009. A decade of lessons learned at a geophysical test site. In: *22nd EGGS Symposium on the Application of Geophysics to Engineering and Environmental Problems 2009*. Society of Exploration Geophysicists, pp. 216–221. <https://doi.org/10.4133/1.3176699>.
- SEMARNAT, 2016. Acuerdo por el que se da a Conocer el Resultado de los Estudios Técnicos de las Aguas Nacionales Subterráneas del Acuífero Cuauitlán-Pachuca, Clave 1508, en el Estado de México, Región Hidrológico-Administrativa Aguas del Valle de México. Published on September 14, 2016 in Diario Oficial de la Federación, Mexico. Retrieved from. <https://www.dof.gob.mx/>.
- SGM, 2002. Carta Geológico-Minera, Ciudad de México E14–2, escala 1: 250,000: Pachuca, Hidalgo, Secretaría de Economía, 1 map. Servicio Geológico Mexicano, Mexico. Retrieved from. <https://www.gob.mx/sgm>.
- Sheriff, R.E., 2002. *Encyclopedic Dictionary of Applied Geophysics*. Society of Exploration Geophysicist, USA. <https://doi.org/10.1190/1.9781560802969>.
- Siles, G.L., Alcérraca-Huerta, J.C., López-Quiroz, P., Carrera Hernández, J., 2015. On the potential of time series InSAR for subsidence and ground rupture evaluation: application to Texcoco and Cuauitlan-Pachuca subbasins, northern Valley of Mexico. *Nat. Hazards* 79 (2), 1091–1110. <https://doi.org/10.1007/s11069-015-1894-4>.
- Spies, B.R., Frischknecht, F.C., 1991. Electromagnetic sounding. In: Nabighian, M.N. (Ed.), *Electromagnetic Methods in Applied Geophysics*, Volume 2, Application, Parts A and B. Society of Exploration Geophysicists, USA, pp. 285–425. <https://doi.org/10.1190/1.9781560802686.ch5>.
- Stein, S., Wyssession, M., 2003. *An Introduction to Seismology, Earthquakes, and Earth Structure*. Blackwell Publishing, Singapore, p. 512. <https://doi.org/10.1017/S0016756803318837>.
- Telford, W.M., Geldart, L.P., Sheriff, R.E., Keys, D.A., 1978. *Applied Geophysics*. Cambridge University Press, USA. <https://doi.org/10.1017/CBO9781139167932>.
- Vázquez-Sánchez, E., Jaimes-Palomera, R., 1989. Geología de la Cuenca de México. *Geofis. Int.* 28 (2), 133–190. <http://revistagi.geofisica.unam.mx/index.php/RGI/article/view/1026>.
- Wentworth, C.K., 1922. A scale of grade and class terms for clastic sediments. *J. Geol.* 30 (5), 377–392. <https://doi.org/10.1086/622910>.
- Williams, B.J., 1972. Tepeate in the Valley of Mexico. *Ann. Assoc. Am. Geogr.* 62 (4), 618–626. <https://doi.org/10.1111/j.1467-8306.1972.tb00890.x>.
- Zebrowski, C., 1992. Los suelos volcánicos endurecidos en América Latina. *Terra* 10, 15–23. <https://www.documentation.ird.fr/hor/fdi:38562>.

2. Mapeo de estructuras someras en un campo de pruebas geofísicas usando gradientes magnético y de inducción electromagnética

(Artículo publicado, citar como: Rosado-Fuentes, A., Arciniega-Ceballos, A., Hernández-Quintero, E., Arango-Galván, C., Salas-Corrales, J. L. & Mendo-Pérez, G. (2023). Mapping near-surface structures in a geophysical test site using magnetic and electromagnetic induction gradients. *Journal of Applied Geophysics*, 215, 105123. <https://doi.org/10.1016/j.jappgeo.2023.105123>)

Este capítulo trata de un estudio que le da continuidad al artículo tratado en el *Capítulo 1: Caracterización geofísica, diseño y construcción del Campo de Pruebas Geofísicas de Teoloyucan para aplicaciones arqueológicas y de ingeniería, Centro de México*, en el cual se aplicaron y complementaron las metodologías de adquisición y procesamiento de datos de los métodos de MG y EMI para mapear e identificar las estructuras someras enterradas en el TGTS y determinar similitudes y diferencias entre las anomalías detectadas. Las características de las estructuras se encuentran detalladas en Rosado-Fuentes *et al.* [2021]. La profundidad promedio a la base de las estructuras 1 a 14 es de 1.02 m. Para las estructuras 15 a 17 las profundidades son de 2.05 m, 1.66 m y 1.55 m, respectivamente.

Para el estudio de MG se utilizan dos sensores iguales de vapor de cesio orientados y configurados de la misma forma, separados verticalmente una distancia fija de 1 m y realizando medidas simultáneas de campo geomagnético total. Al emplear MG se minimizan las fuentes regionales, los errores en la orientación de los sensores, la deriva instrumental por efectos térmicos y la variación diurna. Por lo tanto, con MG no es estrictamente necesario tener una estación base. Los sensores empleados miden en un pequeño ángulo sólido alrededor de la orientación paralela y perpendicular al campo geomagnético; fuera de este ángulo sólido son zonas de sombra donde la señal se pierde [Everett, 2013; Langel y Hinze, 1998; Telford *et al.*, 1978].

Para el estudio de EMI se utiliza un instrumento mono-frecuencial que consta de una bobina transmisora (Tx) y una receptora (Rx) separadas una distancia horizontal fija y conocida (s) medida entre los centros de las bobinas. Si el plano de ambas bobinas es perpendicular al terreno, ambas generan un dipolo horizontal (HD) y su configuración se denomina coplanar vertical (VCP) o modo bajo (low mode). Si el plano de ambas bobinas es paralelo al terreno, ambas generan un dipolo vertical (VD) y su configuración se denomina coplanar horizontal (HCP) o modo alto. La función de respuesta normalizada depende de s y de las propiedades electromagnéticas del subsuelo. Se calcula con las impedancias de las bobinas o con la relación de acoplamiento de las magnitudes de los campos magnéticos secundario (H_s) y primario (H_p), i.e. H_s/H_p . Su parte imaginaria, conocida como cuadratura, está asociada con la conductividad eléctrica aparente (σ_a), mientras que su parte real, conocida como en fase,

está asociada con la susceptibilidad magnética aparente (χ_a). Ambas propiedades pueden ser determinadas simultáneamente con el equipo empleado. Respectivamente, la cuadratura del modo HCP y VCP tiene mayor sensibilidad a la parte media y somera de la profundidad de exploración. Por su parte, la fase del modo HCP y VCP tiene mayor sensibilidad a la parte media y profunda de la profundidad de exploración, respectivamente. En este caso, la configuración de bobinas HCP mapea el espesor del subsuelo donde se encuentran todas las estructuras. El espesor mapeado por la configuración VCP cubre las estructuras 1 a 14, mientras que las estructuras 15 a 17 se extienden más allá del espesor mapeado. Por lo expresado anteriormente, se esperaba que la cuadratura del modo HCP mostrara claramente las anomalías generadas por los objetos enterrados ya que su máxima sensibilidad coincide con la profundidad del techo y base de la mayoría de los objetos. No obstante, los objetos de una escala relativamente menor, en comparación con el volumen de material que influye en la toma de datos, generan anomalías pequeñas que a menudo pasan desapercibidas [De Smedt *et al.*, 2014; Everett, 2013; GF Instruments, 2020; Guillemoteau *et al.*, 2019; Klose *et al.*, 2018; McNeill, 1980; McNeill y Bosnar 1999; Simpson *et al.*, 2010; Spies y Frischknecht, 1991].

2.1 Resumen del artículo

Se aplicaron las técnicas MG y EMI para mapear y diferenciar la respuesta geofísica de las 17 estructuras enterradas a menos de 2.50 m de profundidad en el TGTS. Para mejorar la respuesta de las estructuras someras se desarrolló e incluyó el gradiente de inducción electromagnética (EMIG) y se complementaron las metodologías de adquisición y procesamiento de las técnicas MG y EMI. Esto incluye adquirir y sumar dos levantamientos geofísicos adquiridos mediante transectos paralelos pero perpendiculares entre sí, calcular el EMIG y seccionar los mapas para tener mapas de acercamiento a áreas más pequeñas. La comparación de los mapas de los levantamientos ortogonales entre sí muestra una clara distinción en la distribución de las propiedades físicas del subsuelo como resultado de la dirección de adquisición, la orientación de los transectos y la orientación y rumbo de los sensores. En comparación con la técnica EMI, la técnica EMIG se destaca por presentar resultados claramente notables para la conductividad eléctrica aparente, aunque limitados para la parte en fase de la señal. Para MG y EMIG, los mapas de acercamiento a áreas más pequeñas dan mejores resultados que los mapas del área total del TGTS. Además, sumando los mapas de los levantamientos ortogonales entre sí da los mejores resultados, seguido de los mapas cuyos transectos están orientados este-oeste y por último los mapas cuyos transectos están orientados sur-norte. La mayoría de las estructuras mapeadas presentan valores bajos-medios de MG y valores medios-altos de EMIG. La propuesta metodológica es consistente entre las estructuras de concreto y aquellas que simulan cavidades de aire, y entre las estructuras hechas con varios materiales y geometrías complejas. En algunos casos las estructuras no tienen un contraste significante con el terreno circundante y en otros casos las anomalías están desplazadas en menos de 1.50 m. Con este estudio se demuestra la conveniencia de calcular el EMIG y los beneficios de aplicar la metodología utilizada para recuperar características someras que se pasarían por alto o estarían enmascaradas con las metodologías tradicionalmente usadas.

2.2 Resumen de los resultados del artículo

- La metodología aplicada en la adquisición y procesado de datos consiste en realizar, con diferentes configuraciones de sensores, levantamientos de transectos paralelos pero ortogonales entre sí y sumar los mapas.
- Se aplica un filtro de rechazo de coseno direccional en los maps sur-norte de MG y en todos los de la componente en fase de EMI para remover patrones de anomalías paralelas a los transectos de adquisición que se pueden ampliar con el procesado de datos, enmascarando y malinterpretando los resultados.
- Los intervalos de valores en los mapas sur-norte y este-oeste de MG son, respectivamente, de -260 a 97 nT/m y de -173 a 99 nT/m .
- Los mapas sur-norte y este-oeste, respectivamente, muestran intervalos de valores de conductividad eléctrica aparente de 68 a 123 mS/m y de 60 a 98 mS/m para la configuración de bobinas VCP y de 76 a 112 mS/m para ambos mapas de la configuración HCP.
- Los mapas sur-norte y este-oeste, respectivamente, muestran rangos de valores de fase de 0.19 a 4.95 ppt y de 0.19 a 2.67 ppt para la configuración VCP y de 1.43 a 1.66 ppt y 0.87 a 1.11 ppt para la configuración HCP.
- Coincidencias de estos levantamientos al comparar con los resultados de la caracterización del sitio (Capítulo 1):
 - La conductividad aparente se mantiene en el mismo rango mientras que el rango de la fase se amplia sutilmente en 1 ppt .
 - Los valores máximos de conductividad aparente se concentran en la parte central-este y los mínimos en la esquina suroeste.
 - La parte en fase es máxima en la parte central del TGTS y mínima en la esquina sureste.
 - Los picos de valores de campo magnético total se muestran aislados y concentrados en la esquina sureste, coincidiendo con la zona de valores mínimos de la fase de EMI.
 - Los mapas de las configuraciones VCP y HCP se asemejan entre sí y no muestran claramente los entierros del TGTS.
- Comparativa entre los resultados de los levantamientos sur-norte y este-oeste:
 - A pesar de que los rangos de valores son similares, se observan diferencias importantes en la distribución de los valores entre los levantamientos sur-norte y este-oeste.
 - En los levantamientos de MG, estas diferencias se atribuye a la orientación y rumbo de los sensores y a la dirección de adquisición de los transectos.

- Observaciones similares para la técnica EMI por Guillemoteau y Tronicke [2015] asocia las diferencias al rumbo de los sensores y a que los modos HCP y VCP son afectados por la dirección de adquisición.
 - En nuestro estudio se confirman esas observaciones y se amplían para el levantamiento MG.
- Sin conocer previamente la ubicación de los entierros, los resultados muestran anomalías que son clasificadas como falsos positivos al comparar estos resultados con los mapas de caracterización previa a la construcción del TGTS.
 - Comparando la suma y resta de los levantamientos sur-norte y este-oeste para resaltar anomalías y mejorar la interpretación, la suma da mejores resultados y disminuye la cantidad de falsos positivos.
 - Sin conocer la ubicación de los entierros, como comúnmente sucede en estudios geofísicos, no sería posible diferenciar las anomalías generadas por los entierros de los falsos positivos. Para ello se tendrían que probar otras técnicas como filtros digitales, establecer un valor umbral sobre las anomalías o correlacionando los resultados de diferentes métodos.
 - En este caso, los filtros pasa-bajas, pasa-altas o filtros diferenciables no mejoran el mapeo de las estructuras en los mapas MG y EMI.
 - Algunas anomalías observadas en los mapas no reflejan las estructuras enterradas y algunas se encuentran desfasadas de su centro en menos de 1.50 m.
 - Algunas estructuras no presentan un contraste significativo con su entorno.
 - En general, sumar los levantamientos ortogonales da mejores resultados que los levantamientos individuales, independientemente si en el análisis se considera la ubicación de las estructuras o no.
 - Gradiente de Inducción Electromagnético (EMIG):
 - Se desarrolla para resaltar fuentes locales y someras con la finalidad de mejorar la identificación y localización de estructuras que se encuentren dentro de los espesores mapeados por la técnica EMI.
 - Funciona con datos adquiridos de forma continua o discreta, calculándose con una operación matemática sencilla y similar a los principios de MG.
 - A diferencia de MG, para poder calcular el EMIG es necesario realizar dos levantamientos con los mismos transectos, dirección de adquisición, orientación del sensor, taza de muestreo y altura del sensor del suelo. La diferencia entre los levantamientos es la configuración de las bobinas (HCP, VCP u otra), la distancia s o una combinación de las anteriores.

- Cada levantamiento mapea un espesor diferente del subsuelo, desde el suelo hasta la profundidad igual al rango de profundidad efectiva que depende de la configuración de bobinas usado.
- Procesando convencionalmente los datos, se calculan los rangos de profundidad efectiva, se definen los espesores del subsuelo mapeado y se calcula la diferencia entre ellos.
- El EMIG ($\Delta EMIG$), para conductividad aparente (σ_a) o susceptibilidad magnética (χ_a), es calculado como el gradiente vertical entre el mallado de los mapas de los levantamientos normalizado por la diferencia entre los rangos de profundidad efectiva de los levantamientos (Δh). Siendo D_s y S_s , respectivamente, los levantamientos con mayor y menor rango de profundidad efectiva, el EMIG se calcula con la siguiente ecuación:

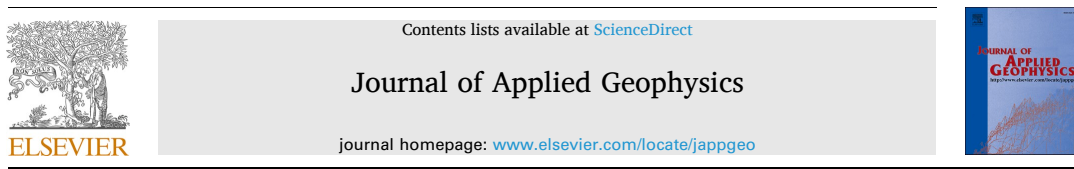
$$\Delta EMIG_{\sigma_a, \chi_a} = \frac{D_s - S_s}{\Delta h} \quad (2.1)$$

- Se generan los mapas de EMIG de los levantamientos sur-norte y este-oeste y posteriormente se sumaron como se realizó anteriormente.
- Sin previo conocimiento de la ubicación de los entierros, la mayoría son claramente visibles en el mapa de conductividad con valores relativamente altos. Pocos entierros son identificados en el mapa de la fase. Estos últimos son similares a los mapas EMI del modo VCP para la fase.
- Si se considera la ubicación de los entierros en el análisis, la mayoría de las estructuras son visibles y pueden ser asociadas a las anomalías observadas, aunque algunas siguen mostrándose desplazadas en $< 1.50 \text{ m}$ del centro de los entierros.
- En los mapas EMIG, las estructuras 2 y 7 son las menos claras.
- En general, los mejores resultados se obtienen en la suma de los mapas, luego en los mapas este-oeste y posteriormente en los mapas sur-norte.
- Los picos en los mapas de MG son atribuidos a desechos antropogénicos y en los mapas EMIG se atribuyen a la presencia de características someras que no reflejan las estructuras del TGTS.
- Mapas de acercamiento a áreas más pequeñas:
 - Se crean para visualizar cada entierro de forma individual y tener mayor detalle de su efecto local.
 - Mejora la identificación y localización de las estructuras que los mapas de toda el área del TGTS, en especial para el caso de los mapas EMIG de la fase.
 - Nuevamente se muestran diferencias significativas en la distribución de las propiedades físicas medidas entre los mapas de levantamientos ortogonales entre sí.

- En general, para MG los mejores resultados se observan en los mapas este-oeste, seguidos de la suma y luego de los sur-norte. Para EMIG primero sobresalen los mapas de la suma, seguidos de los este-oeste y finalmente los sur-norte.
- La mayoría de las estructuras se muestran con valores bajos-medios en MG y medios-altos de conductividad aparente y fase.
- Las estructuras 6, 7, 8 y 12 muestran menos contraste magnético con su entorno, lo mismo ocurre con las estructuras 2 y 7 en los mapas EMIG de conductividad y la estructura 8 en los mapas EMIG de fase.
- Cambiar el material de relleno de tepetate a arena mejora el contraste de las estructuras con su entorno, mantiene los mismos valores de MG, aumenta el valor de conductividad y disminuye el valor de la fase.
- Hay consistencia en los resultados de las diferentes estructuras de concreto y aire (huecas). Estas se ven con valores bajos de MG y en general con valores medios-altos de conductividad y fase, exceptuando el valor relativamente alto de MG de la estructura 9.
- En general las estructuras 14, 16 y 17 muestran valores variables de MG y EMIG que reflejan los diferentes materiales con las que se construyeron, el espesor del material de relleno y la geometría de las estructuras. Las anomalías de la estructura 16 están dominadas por los cubos de concreto y basalto.

2.3 Artículo publicado

Journal of Applied Geophysics 215 (2023) 105123



Mapping near-surface structures in a geophysical test site using magnetic and electromagnetic induction gradients

Alejandro Rosado-Fuentes^{a,*}, Alejandra Arciniega-Ceballos^b, Esteban Hernández-Quintero^b, Claudia Arango-Galván^b, José Luis Salas-Corrales^b, Gerardo Mendo-Pérez^a

^a Posgrado en Ciencias de la Tierra, Universidad Nacional Autónoma de México, 04510 CDMX, Mexico

^b Instituto de Geofísica, Universidad Nacional Autónoma de México, 04510 CDMX, Mexico

ARTICLE INFO

Keywords:
Magnetic
Electromagnetic induction
Gradient
Test site
Near-surface

ABSTRACT

We applied Magnetic Gradiometry (MG) and Electromagnetic Induction (EMI) techniques to map and differentiate the geophysical response of 17 buried structures at <2.50 m deep in the Teoloyucan Geophysical Test Site (TGTS). To enhance the response of near-surface structures, we include the Electromagnetic Induction Gradient (EMIG) and complement MG and EMI acquisition and processing methodologies. This includes, acquiring and adding together orthogonal-transect surveys, computing the EMIG and sectioning area maps into close-up maps. The orthogonal-transect surveys clearly show distinct distributions of the physical properties resulting from the acquisition direction, the orientation of the transects and from the orientation and heading of the sensors. Compared with EMI, EMIG provides remarkable results for apparent conductivity although limited for in-phase data. For MG and EMIG, close-up maps yield better results than area maps. Also, adding the orthogonal-transect survey grids gives better results, followed by the E-W transect surveys and then by the S-N transect surveys. Most of the mapped structures present low-medium MG values and medium-high EMIG values. The proposed methodology is consistent for concrete and air-cavity structures, and for structures made with various materials and complex geometries. In some cases, the structures do not have enough contrast with their surrounding terrain and in others, the anomalies are shifted in <1.50 m. In this study, we demonstrate the convenience of computing the EMIG and the benefits of applying the used methodology to retrieve near-surface features that would be overlooked with common-practice methodologies.

1. Introduction

Geophysical test sites are frequently built to replicate and simulate features encountered in different scenarios in diverse areas of geophysical exploration. Their main purpose is to investigate the geophysical response of the ground by targets whose properties and attributes are well known. Test sites are suitable to validate the acquisition, processing and interpretation of geophysical data in a specific controlled environment. Moreover, they are useful to provide students and technicians experience and expertise in the use of geophysical techniques. Magnetic Gradiometry (MG) and Electromagnetic Induction (EMI) are non-destructive near-surface mapping techniques that can map large areas rapidly and effectively, saving resources. They are widely implemented individually, together or along with other geophysical techniques in geological, agricultural, forensic, engineering, archaeological, cultural heritage and other Earth Science investigations

(Allred et al., 2004; Kvamme, 2006; Pringle et al., 2008; Pueyo Anchuela et al., 2015; Rucker, 2010; Silván-Cárdenas et al., 2021; Wamalwa et al., 2011).

In this work we applied MG and EMI techniques in Teoloyucan Geophysical Test Site (TGTS), a facility that comprises 17 buried subsurface structures similar to those encountered in engineering and archaeological contexts in Mexico (Fig. 1). The attributes and properties of the buried structures cover several material composition and geometries and are well characterized by Rosado-Fuentes et al. (2021). Following this study, in this work we apply and complement an acquisition and processing methodology for near-surface studies in engineering and archaeological contexts. Our aim is to map and identify near-surface structures and to determine similarities and differences between the generated anomalies. We first briefly introduce the theoretical basis of the applied methods and present the Electromagnetic Induction Gradient (EMIG), which enhances anomalies and is based on a

* Corresponding author.
E-mail address: arosadof@ciencias.unam.mx (A. Rosado-Fuentes).

simple math calculation that follows the principle of the MG. Then, we describe TGTS and the characteristics of the geophysical surveys. Finally, we apply and complement a methodology of data acquisition and processing that consists in making, with different coil configurations, orthogonal-transect surveys with the same geophysical technique, adding the orthogonal-transect grids together, computing the EMIG and making close-up maps. Our approach gives exceptional results and can be replicated elsewhere in near-surface geophysical studies. We demonstrate that common-practice methodologies overlook most of the near-surface structures and that by computing the EMIG and following the applied methodology most of the structures can be retrieved.

2. Magnetic gradiometry

Magnetic methods measure the Earth's geomagnetic field as the sum of the principal field, the field generated by sources in the magnetosphere and ionosphere, and the lithospheric field. The residual field can be obtained by a diurnal correction or by applying the magnetic gradiometry (MG) method (Langel and Hinze, 1998; Telford et al., 1990). MG surveys enhance local and near-surface sources revealing finer details.

This method minimizes regional sources, errors in orientation, effects of thermal drift and diurnal variation (Everett, 2013; Hinze et al., 2013; Milsom, 2003; Telford et al., 1990), eliminating the need for magnetic base observations (Hinze et al., 2013). Gradiometers are formed by two equally configured sensors separated by a vertical or horizontal fixed distance that records simultaneous readings in each sensor (Everett, 2013; Hinze et al., 2013; Langel and Hinze, 1998; Telford et al., 1990). The vertical gradient is given by

$$\frac{\partial F}{\partial z} = \frac{F_2 - F_1}{\Delta z} \quad (1)$$

where F_1 and F_2 are the readings at the higher and lower sensor positions, respectively. The gradient is normalized by the vertical distance between the sensors, Δz . Generally, an elevation difference of 1.0 m suffices (Everett, 2013; Telford et al., 1990).

Cesium vapor magnetometers operate by quantum phenomena like optical pumping, Zeeman effect and precession of the magnetic moments of electrons (Everett, 2013; Hinze et al., 2013; Telford et al., 1990). A detailed explanation of its operation can be found in Everett (2013), Hrvovic and Hollyer (2005) and Telford et al. (1990). Vapor

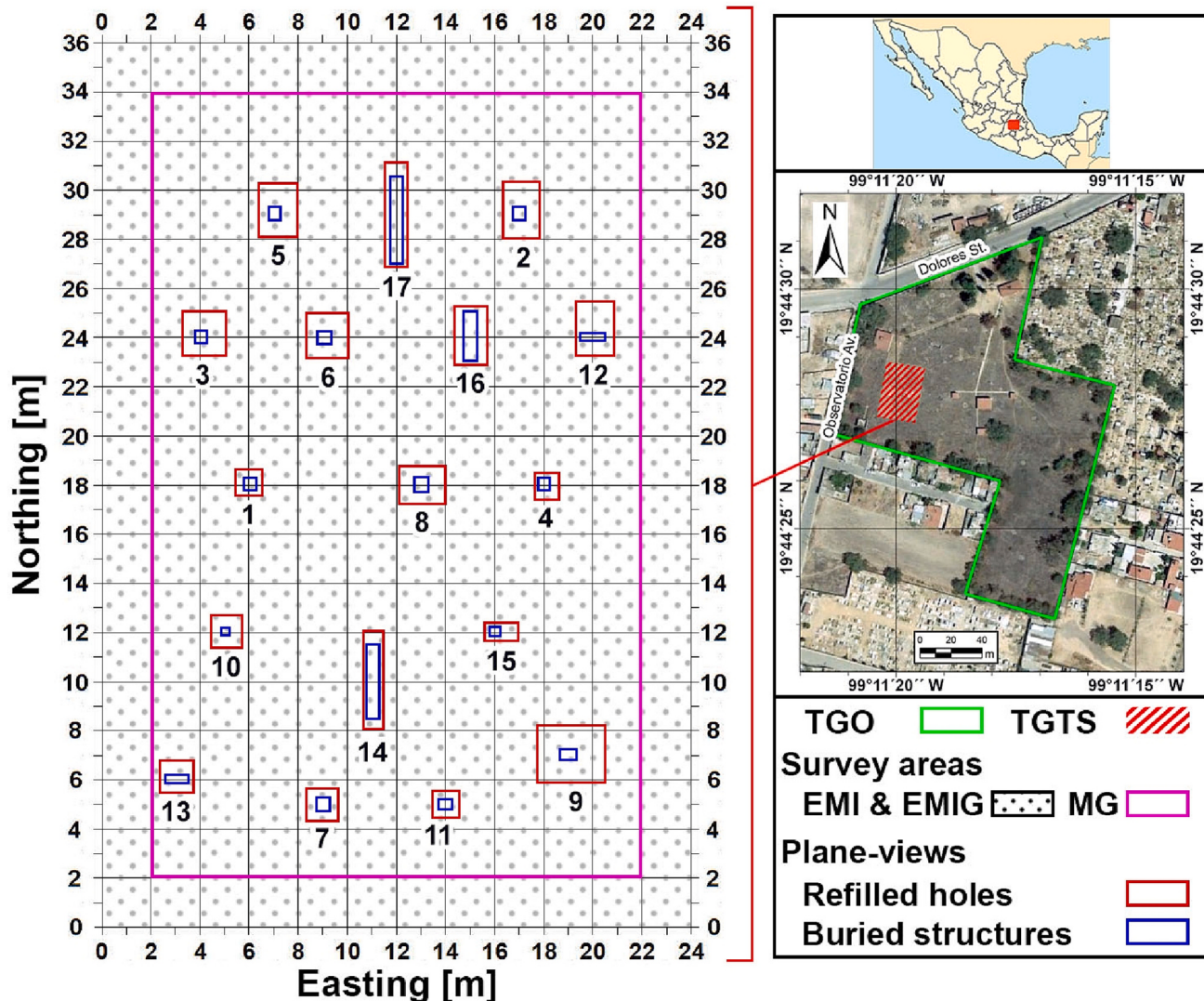


Fig. 1. Right panel shows the location of Teoloyucan Geomagnetic Observatory (TGO) and of Teoloyucan Geophysical Test Site (TGTS) with a green polygon and a red striped area, respectively. Left panel shows a close-up of TGTS with the plan views of the 17 buried structures (blue boxes) and refilled holes (red boxes), along with their identification number; their location and areas were taken from Rosado-Fuentes et al. (2021). Purple and black dotted boxes indicate the areas covered by the Magnetic Gradiometry (MG) and Electromagnetic Induction (EMI) & Electromagnetic Induction Gradient (EMIG) surveys, respectively. (For interpretation of the references to color in this figure legend, the reader is referred to the web version of this article.)

magnetometers are direction sensitive and have shadow zones where the signal is lost. When the sensor is oriented a few degrees out of the direction of the geomagnetic field or its perpendicular direction, the signal is lost and measurements cannot be acquired. However, this limitation can be overcome with mechanical orientation of the sensor, multi-vapor-cell configurations and split-beam technology (Hinze et al., 2013; Milsom, 2003).

3. Electromagnetic induction

The electromagnetic induction (EMI) method is governed by low-frequency time-varying electromagnetic fields originated near the surface that are induced into the subsurface according to induction phenomenon. A mono-frequency EMI sensor operates at low-induction-number (LIN) when its transmitter (Tx) to receiver (Rx) coil center distance (s) is less than the skin depth (δ), i.e. $s/\delta \ll 1$ (Everett, 2013; GF Instruments, 2020; McNeill, 1980; Spies and Frischknecht, 1991). If both the Tx and Rx coils are perpendicular to the ground, i.e. vertical coplanar (VCP); they each form, individually, a horizontal dipole, HD mode or low mode. If both the Tx and Rx coils are parallel to the ground, i.e. horizontal coplanar (HCP); they each form, individually, a vertical dipole or VD mode or high mode (Everett, 2013; Spies and Frischknecht, 1991). The orientation of the EMI instrument can be aligned parallel, P-mode, or perpendicular, T-mode, with respect of the transect direction (Everett, 2013). Regardless of the coil configuration and orientation, a controlled current flow in Tx, generally between 1 and 3 A, generates an in-phase primary magnetic field (H_p) that imposes an electromotive force (emf) in the soil. The ground restores its equilibrium by generating a back-emf that develops eddy current inducing a phase-shifted secondary magnetic field (H_s). The phase shift depends on the electrical properties of the ground, particularly on the electrical conductivity (σ). If the phase shift is 90°, H_s is completely out of phase with H_p and the ground is completely electrically conductive. If the phase shift is 0°, the ground is perfectly resistive and H_s is completely in-phase with H_p . In general, and considering that the air has low conductivity and magnetic susceptibility, H_s is out-of-phase and attenuated with respect of H_p , which indicates the energy-dissipating induction phenomenon. The primary field depends on the physical characteristics and geometric properties of the Tx loop, which are known and controlled by the operator. The secondary field depends on the geometry, position and electrical conductivity of the target. H_s and H_p induce a current in the Rx coil that is corrected by removing H_p . The normalized response function is calculated with the impedances of the coils or by operating the coupling ratio of the magnitudes of the secondary to primary magnetic fields, i.e. H_s/H_p . In general, the EMI method assumes that the magnetic permeability is equal to its free space value. If $r/s \ll 1$, where r is the radius of loop Tx and s is the Tx-Rx dipole center distance and at LIN condition, the normalized response function depends on s and the electromagnetic properties of the subsoil. Its imaginary part, also known as the quadrature, is 90° out-of-phase with the current in Tx. In a first order approximation, the apparent conductivity (σ_a) of the ground, measured in Siemens per meter (S/m) (Everett, 2013; GF Instruments, 2020; McNeill, 1980; Spies and Frischknecht, 1991), is linearly related to the quadrature response of the normalized response function as

$$\sigma_a = \frac{4}{\mu_0 \omega s^2} \left| \text{Im} \left(\frac{H_s}{H_p} \right)_{h,v} \right| \quad (2)$$

where s is the Tx-Rx dipole center distance, μ_0 is the magnetic permeability in vacuum, ω is the angular frequency, Im denotes the imaginary part of the coupling ratio of the magnitudes of the secondary to primary magnetic fields and the sub-indexes h and v stand for HCP or VCP modes, respectively (Everett, 2013; McNeill, 1980). The real part of the normalized response function is in-phase with the current in Tx. The apparent magnetic susceptibility (x_a) of the ground is approximated by the in-phase response of the normalized response function as (Everett,

2013; GF Instruments, 2020; Spies and Frischknecht, 1991)

$$x_a = 2 \times 0.001 \times \text{Re} \left(\frac{H_s}{H_p} \right)_{h,v} \quad (3)$$

where Re denotes the real part of the coupling ratio of the magnitudes of the secondary to primary magnetic fields, the sub-indexes h and v stand for HCP or VCP modes, respectively, number 2 accounts for measuring a half-space (De Smedt et al., 2014) and the factor 0.001 converts the output in parts per thousand (ppt) (Simpson et al., 2010). The in-phase response is less than the quadrature response at LIN conditions (McNeill and Bosnar, 1999) and it can serve as an indicator of artificial metal objects and help distinguish artificial structures from natural geology seen in apparent conductivity maps (GF Instruments, 2020). The relative contribution to H_s depends on the materials located at different depths in the subsoil. The sensitivity function can be calculated for the in-phase and out-of-phase components, each presenting different distributions. For the quadrature component, the VCP and HCP modes are more sensitive to the shallowest and middle parts of the exploration depth, respectively. For the in-phase component, the VCP and HCP modes are more sensitive to the middle and upper parts of the exploration depth, respectively. Additionally, the HCP mode might contain negative sensitivity values. Consequently, the surveyed area maps a plane parallel to the surface whose values represent the contribution of a large volume of subsurface materials from the surface to the effective depth, which depends on the Tx-Rx dipole center distance and the selected coil configuration mode (Guillemoteau et al., 2019; Klose et al., 2018; McNeill, 1980; McNeill and Bosnar, 1999; Milsom, 2003). More robust calculations of apparent conductivity and permeability based on a full non-linear homogeneous half-space theory have been proposed in Huang and Won (2001), Guillemoteau et al. (2016), and Hanssens et al. (2019). Such approaches take into account the height of the sensor, which critically affect the H_s response, they are not restricted to the HCP and VCP coil geometries and, for the case of the out-of-phase response, provide more robust evaluation of the electrical conductivity in conductive environments.

3.1. Electromagnetic induction gradient

In an effort to enhance local and near-surface sources and to better identify and locate structures within the subsurface mapped thicknesses, we developed the Electromagnetic Induction Gradient (EMIG) technique governed by a simple math calculation that follows the principle of MG and it is feasible to apply it to continuous or discrete data sets. Contrary to MG where you have two identical instruments configured and oriented in the same manner acquiring data at two different heights, the EMIG operates by doing two surveys following the same transects, acquiring the data in the same direction and with the same instrument orientation and sampling rate. In both surveys the height of the instrument from the ground does not change. The difference between the two surveys relies in the coil configurations used (HCP, VCP or else), the Tx-Rx dipole center distance or a combination of both. In either case each survey will map different subsurface thicknesses, from the surface to a depth equal to its effective depth range. Once the apparent conductivity and in-phase maps are generated following any chosen methodology, with the coil configuration and the Tx-Rx dipole center distance we can calculate the effective depth range of each survey, define the subsurface mapped thickness and determine the depth difference between the effective depth ranges of both surveys. The EMIG (ΔEMI), for apparent conductivity (σ_a) or magnetic susceptibility (x_a), is obtained by calculating the vertical spatial gradient between the grids of both surveys and is normalized by the depth difference between the effective depth ranges of each survey. The EMIG follows the equation

$$\Delta EMI_{\sigma_a, x_a} = \frac{D_s - S_s}{\Delta h} \quad (4)$$

where D_s and S_s are the readings of the surveys with the deepest and shallowest effective depth range, respectively, and Δh is the depth difference between the effective depth ranges of each survey. The apparent conductivity and in-phase values in an EMI study are obtained with scalar Eqs. 2 and 3, mainly with the coupling ratio of the magnitudes of the secondary to primary magnetic fields. Therefore, the ratio is a scalar magnitude proportional to the electrical apparent conductivity or magnetic susceptibility of the subsoil (De Smedt et al., 2014; Everett, 2013; McNeill, 1980). In the same manner, an EMIG value can be calculated following the scalar Eq. 4 since it operates with scalar apparent conductivity and in-phase values from the readings of two surveys with different effective depth range, one being deeper than the other one.

4. Test site description and geophysical surveys

TGTS covers an area of 864.00 m² (24.00 m E by 36.00 m N), inside Teoloyucan Geomagnetic Observatory (TGO), UNAM, N of Mexico City (Fig. 1 right). The geomagnetic sensors at TGO are located in the buildings at the center of the terrain. The test site is situated in the W central portion of TGO (red striped area in Fig. 1 right), warehouses are at least 8.00 m away from its SW and NW corners. The site is a flat overgrown with grass and weed area delimited every 2.00 m with half-buried concrete cylinders of 0.15 m in diameter and 0.30 m in height. TGTS lithological section indicates that the site is composed by a hard-consolidated horizon of volcanic origin named *tepetate*, that can be translated as a rock-like soil horizon (Zebrowski, 1992). This horizon particularly shows four main well graded coarse soil layers named, from the surface down, soil, soil-*tepetate*, beige-brown *tepetate* and dark brown *tepetate*. Pyroclastic materials from the Sierra de Tepotzotlan originated both *tepetates* in this sequence. From the site characterization done prior to the construction of TGTS, this sequence presents magnetic gradient, apparent conductivity and in-phase values ranges of 120.00–420.00 nT/m, 70.00–120.00 mS/m and 1.14–1.63 ppt, respectively (Rosado-Fuentes et al., 2021). The geophysical characterization of the area presents a smooth distribution of the geophysical properties and the subsoil is composed by four geophysical layers that coincide with the lithological layers. On the other hand, these smooth changes in geomagnetic and electromagnetic properties observed in TGTS (Rosado-Fuentes et al., 2021) fulfill the requirements established by the International Association of Geomagnetism and Aeronomy to operate a Geomagnetic Observatory (Jankowski and Sucksdorff, 1996).

TGTS is composed by 17 buried structures at <2.00 m deep whose characteristics cover a range of features in geometry, stratigraphic sequences and material composition. They were built using Pre-Hispanic materials like *adobe* (i.e. mudbrick, made with a mixture of mud and organic material), wood, basalt, *tezontle* (i.e. dark-red porous volcanic scoria material) and current materials like concrete, reinforced concrete, plastic containers and PVC pipes. The holes dug to build the structures were refilled and compacted with the *tepetate* extracted during the excavation, except for structure 3 that is refilled with sand. Cubic structures, from 1 to 8, are made of concrete, brick, *adobe*, tile basalt, tile *tezontle*, and wood. Structure 1 is the only one including metal parts, it is made of reinforced concrete. Cylindrical bodies include structure 11, made of concrete, and structures 12 and 13, made with different PVC sealed pipes dispositions. Structures 9 and 10 are plastic containers simulating, respectively, a void and a water cavity that can be refilled or changed through a tube connected to its lid. Structures 14 and 15 simulate horizontal and vertical stratigraphic sequences, respectively; both are built using cubes made of the materials mentioned above. Finally, structures with irregular geometry, 16 and 17, are made of concrete. Structures 1–8, 10 and 15 have a square plan view, while structures 9, 11–14 and 16–17 have a rectangular plan view. The plan view of the structures and the holes for the construction are shown in Fig. 1 left in blue and red boxes, respectively. Details of the dimensions,

depth and thickness of the refilled materials and the structures can be consulted in Rosado-Fuentes et al. (2021). MG and EMI & EMIG surveys were carried out in TGTS, the surveyed areas for each method are shown in Fig. 1.

4.1. MG

Two total field MG surveys were conducted in TGTS on March 4, 2019 using two Geometrics G-858 cesium vapor magnetometers oriented vertically and separated 1.0 m from each other, the lower sensor was in average 0.45 m from the ground surface. Total magnetic field measurements in both surveys were taken every second, approximately every 0.5 m, along parallel transects separated every 1.00 m and cover an area of 640.0 m² (20.0 m E by 32.0 m N); preventing the effects of the concrete bodies that delimit the site (purple box in Fig. 1 left). One survey consists of 33 E–W parallel transects with 1140 measured points, starting in the SE corner of the site and moving N. The other survey consists of 21 S–N parallel transects with 1220 measured points, starting in the SE corner of the test site and moving W. The geomagnetic external activity reported by Kyoto Dst Geomagnetic Index is available at the World Data Center for Geomagnetism, Kyoto, Japan and averages −18.9 nT, with a variation of 11.0 nT. The Postdam Kp Index values are available at the GeoForschungsZentrum, Postdam, Germany and are <2.7 nT, with an average value of 1.4 nT. Both indexes reflect a quiet geomagnetic day without undesirable effects due to natural external variations. TGO data indicates a total field diurnal variation of <27.0 nT for the day of the survey and <4.5 nT during the data acquisition period. After corrections, data was interpolated using the Kriging method (Haas and Viallix, 1976) and reduced to the magnetic pole (RTP).

4.2. EMI & EMIG

Four T-mode EMI surveys were conducted in TGTS covering the full area (black dotted area in Fig. 1 left) using a CMD-2 conductivity meter by GF Instruments equipped with a GPS. CMD-2 effective depth range for VCP and HCP modes is 1.50 m and 3.00 m, respectively, its Tx-Rx dipole center distance is 1.89 m (GF Instruments, 2020) and the average instrument clearance above the ground surface is 1.00 m. Using the manufacturer's Tx-Rx dipole center distance, the calculated effective depth ranges for the imaginary component of the VCP and HCP mode, using the cumulative response sensitivity function are 1.43 m and 3.00 m, respectively (McNeill, 1980; McNeill and Bosnar, 1999; Milsom, 2003). The in-phase component sensitivity function shows different distributions and changes of sign for standard coil configurations, in particular for VCP and HCP modes (Guillemoteau et al., 2019; Klose et al., 2018). The sensor measures the quadrature and in-phase components of the normalized response function simultaneously in S/m while the in-phase reading is automatically converted to ppt (Everett, 2013; GF Instruments, 2020). VCP and HCP mode coil configuration surveys were acquired along S–N parallel transects starting in the SE corner of the site and moving W and along E–W parallel transects starting in the SE corner of the site and moving N. The S–N and E–W surveys for the VCP mode consist of 1234 and 1164 measured points, respectively, and for the HCP mode of 1173 and 1162 measured points, respectively. In all the surveys the transects were separated every meter and the sampling rate was 1 Hz, making a measurement approximately every 0.5 m. Data processing includes removing incomplete acquisition points, averaging data points with the same geographical coordinates, changing the units to mS/m and transforming data to TGTS relative coordinates (Northing and Easting). Using the effective depth ranges provided by the manufacturer for the coil configurations employed, the depth difference between the effective depth ranges of each survey is $\Delta h = 1.50$ m. We used this value to calculate the EMIG of the S–N and E–W surveys (Eq. 4), in our case D_s and S_s are the survey maps for the HCP and VCP modes, respectively. All the data was interpolated using the Kriging method (Haas and Viallix, 1976).

5. Results and interpretation

The S–N MG map and all the EMI in-phase maps showed regular line patterns parallel to the acquisition transects. This corrugation appearance can be enhanced with the processing methodology applied by the analyst, masking near-surface anomalies and misinterpreting the results. To de-corrugate the data without changing the distribution of the physical properties, we applied a directional cosine rejection filter that follows the formula

$$L(\theta) = \left| \cos^n \left(\alpha - \theta + \frac{\pi}{2} \right) \right| \quad (5)$$

where n is the degree of the cosine function, α is the filtering direction in degrees relative to the North and θ is the wavenumber direction. This filter was applied to reject only wavelengths in the direction of the acquired transects (Cheyney et al., 2012; Fedi and Florio, 2003; Geosoft, 2007). It should be noted that this filter influences NNW and NNE trends (Ferraccioli et al., 1998) and we used $n = 2$ (Fedi and Florio, 2003).

The S–N and E–W MG data shows values ranging, respectively, from –260 nT/m to 97 nT/m (left map in Fig. 2) and from –173 nT/m to 99 nT/m (central map in Fig. 2). The apparent conductivity data ranges of the VCP mode for the S–N and E–W surveys are, respectively, 68–123 mS/m and 60–98 mS/m (top left and central maps in Fig. 3) and for both HCP modes the data range is 76–112 mS/m (middle left and central maps in Fig. 3). The in-phase data ranges of the VCP mode for the S–N and E–W surveys are, respectively, 0.19–4.95 ppt and 0.19–2.67 ppt (top left and central maps in Fig. 4). The in-phase data ranges of the S–N and E–W HCP mode are, respectively, 1.43–1.66 ppt and 0.87–1.11 ppt (middle left and central maps in Fig. 4). Comparing these data ranges with the site characterization values obtained prior to the construction of TGTS, the apparent conductivity remains in the same range while the in-phase values have widened by almost 1 ppt. The apparent conductivity maps show the highest and lowest values at the central E and SW corner sections, respectively (top and middle, left and central maps in Fig. 3) and the maximum and minimum values for the in-phase maps are concentrated at the central and SE corner sections, respectively (top and middle, left and central maps in Fig. 4). Also, isolated magnetic peaks in the SE corner match a minimum in-phase value area. These characteristics are also observed in the MG and EMI maps of the site characterization done prior to the construction of TGTS (Rosado-Fuentes et al., 2021).

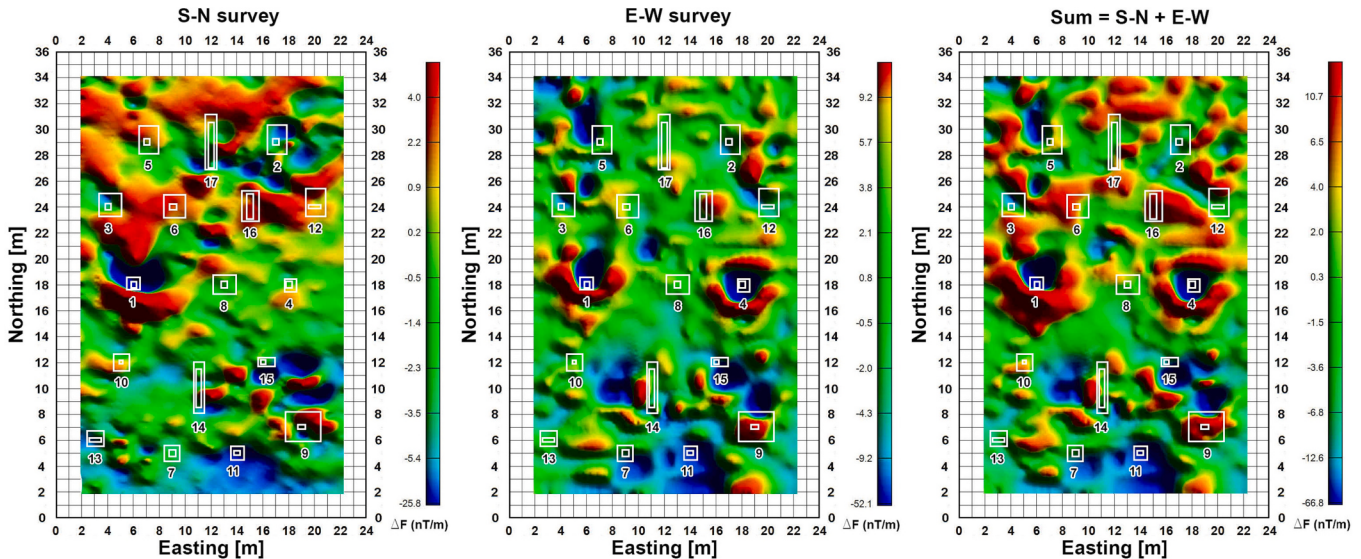


Fig. 2. S–N (left), E–W (central) and Sum (right) Magnetic Gradiometry (MG) survey maps for TGTS. The plan views of the buried structures and the holes dug during construction are shown with white boxes along with their identification number. Color bars in each panel indicate the value range of the vertical magnetic gradient. (For interpretation of the references to color in this figure legend, the reader is referred to the web version of this article.)

Although the ranges shown in this study are fairly similar in all MG and EMI maps, significant differences can be observed in the distribution of the values between the S–N and E–W surveys. These differences can clearly be seen around structure 4 in the MG and EMI conductivity maps and around structure 12 in the EMI in-phase maps. For the magnetic results shown in Fig. 2, since we measured the magnitude of the total magnetic field, it would not be expected to have differences in the values nor their distribution between the S–N and E–W surveys. These differences can be explained with the physics of the sensor which is an optically pumped simple self-oscillating split-beam Cesium-133 vapor magnetometer. In these type of sensors, the value of the magnetic field is obtained by detecting and measuring light modulation and its frequency, which change when the direction of the magnetic field changes because the self-orientating frequency shifts. If the heading of the sensor changes, the direction of the magnetic field with respect of the sensor will change, shifting the self-orientating frequency and changing the value of the magnetic field (Everett, 2013; Hinze et al., 2013; Hrvic and Hollyer, 2005; Telford et al., 1990). Therefore, the differences observed on the S–N and E–W magnetic surveys is mainly attributed to the sensor orientation and heading, and to the acquisition direction of the transects. The differences on the values and the distribution of the EMI results shown in Figs. 3 and 4 have been observed by Guillemoteau and Tronc (2015). These differences are linked to the heading of the sensor because the standard loop-loop geometries show 3D sensitivity functions with non-circular symmetries for both conductivity (Guillemoteau et al., 2017) and in-phase (Klose et al., 2018) readings. Guillemoteau and Tronc (2015) show that the standard popular EMI coil configurations, in particular the VCP and HCP modes, are affected by the direction of data acquisition. Here we confirm such observations and expand them to MG surveys. However, the contributions of anisotropic effects should not be completely discarded, and needs to be studied further in detail but is out of the scope of the present study.

As mentioned before, for the quadrature component, the VCP and HCP modes are more sensitive to the shallowest and middle parts of the exploration depth, respectively. Most of the targets are between 0.5 m and 1.0 m deep, this depth coincides with the maximum sensitivity of the HCP mode. We expected the HCP map to show clearly the anomalies of the targets. However, HCP maps show a lot of resemblance to the VCP maps, without clearly enhancing the targets. For the in-phase component, the VCP and HCP modes are more sensitive to the middle and upper parts of the exploration depth, respectively, and the HCP mode

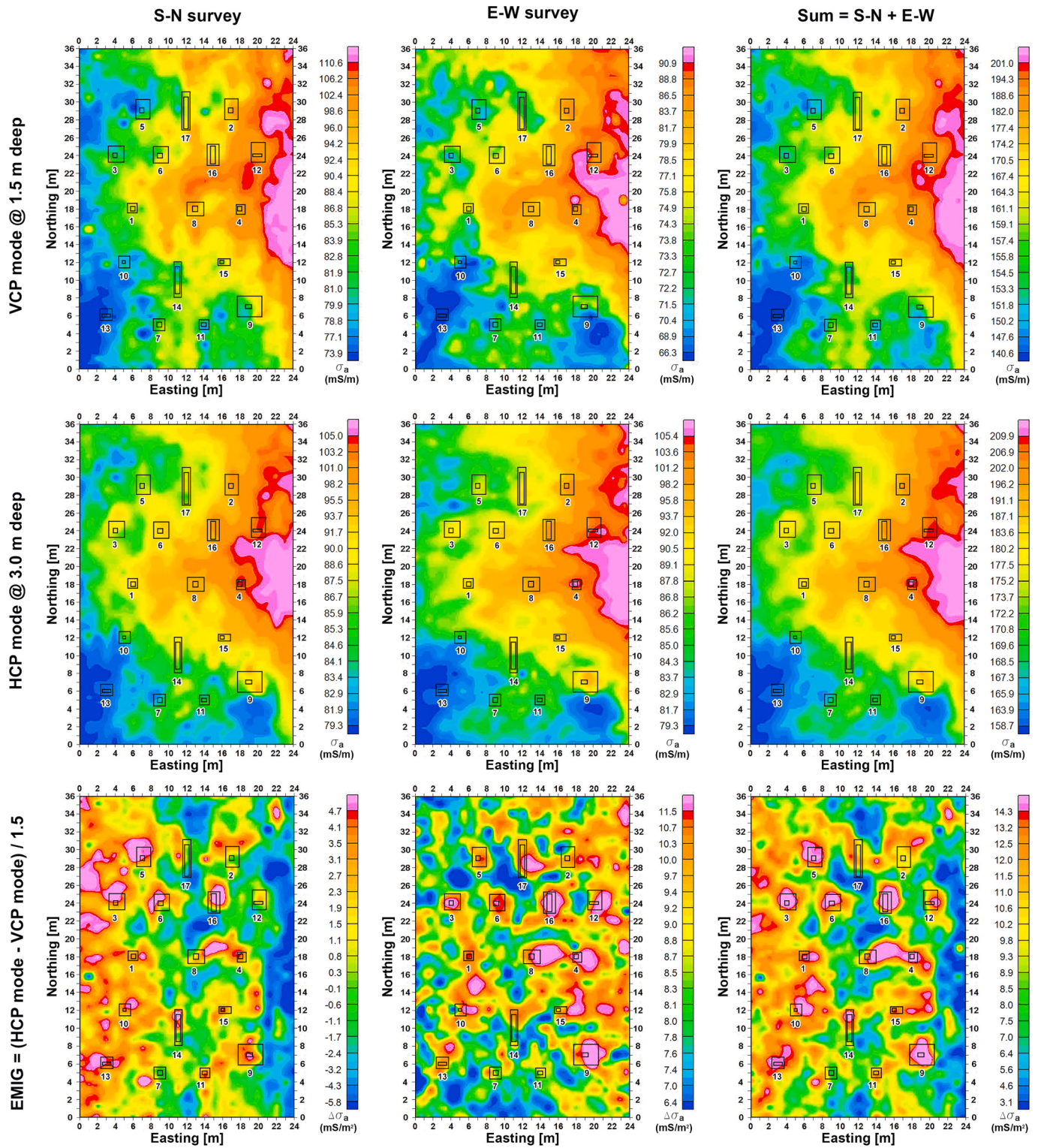


Fig. 3. Teoloyucan Geophysical Test Site (TGTS) S–N (left), E–W (central) and Sum (right) Electromagnetic Induction (EMI) apparent conductivity survey maps for the VCP (top) and HCP (middle) mode acquisition and the Electromagnetic Induction Gradient (EMIG) calculation (bottom). The plan views of the buried structures and the holes dug during construction are shown with black boxes along with their identification number. Color bars in each panel indicate the conductivity value range. (For interpretation of the references to color in this figure legend, the reader is referred to the web version of this article.)

might contain negative sensitivity values. Therefore, we expected the VCP mode to better map the targets, in particularly structure 1. Similarly to the quadrature component, HCP and VCP maps closely resemble each other but they do not clearly show the anomalies of the targets. To enhance the anomalies generated by the buried structures and to

improve the interpretation, the S–N and E–W survey grids were added together, i.e. Sum grid = S–N survey grid + E–W survey grid (right map in Fig. 2 for the MG map and right top and middle maps in Figs. 3 and 4, respectively, for EMI conductivity and in-phase maps). [Guillemeau and Troncicke \(2015\)](#) show, especially for the configurations using

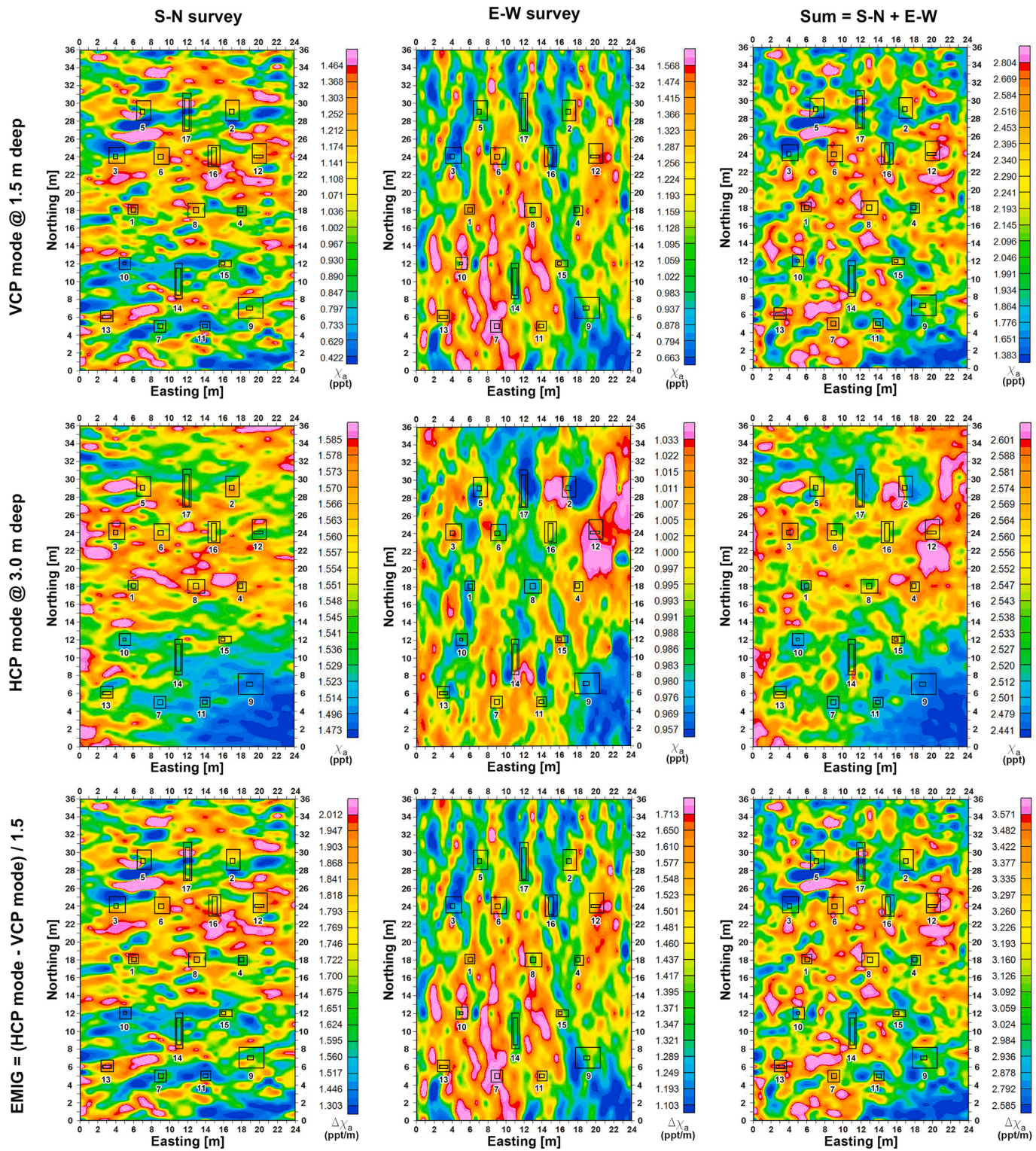


Fig. 4. Teoloyucan Geophysical Test Site (TGTS) S–N (left), E–W (central) and Sum (right) Electromagnetic Induction (EMI) in-phase survey maps for the VCP (top) and HCP (middle) mode acquisition and the Electromagnetic Induction Gradient (EMIG) calculation (bottom). The plan views of the buried structures and the holes dug during construction are shown with black boxes along with their identification number. Color bars in each panel indicate the in-phase value range. (For interpretation of the references to color in this figure legend, the reader is referred to the web version of this article.)

vertical coils which induce eddy current patterns in a preferential direction, that acquiring orthogonal-transect surveys and adding the grids can provide maps that are more in agreement with the true lateral distribution of EMI properties and with better signal to noise ratio. A similar procedure can be generated by subtracting the survey grids

(Simpson et al., 2009), but in our case the sum generates better results. On the other hand, the buried structures are not mapped better after applying low-pass, high-pass or derivative filters to the MG and EMI maps. The only exception is applying a high-pass filter using a cut-off wavenumber of 5 cycles/m in the E–W EMI apparent conductivity

HCP mode map. Note that the applied methodology, on both MG and EMI data, enhances anomalies that could be classified as false positives, especially if the location of the buried objects is unknown and if there were no characterization maps of the site prior to the development of TGTS. In our analysis, the value range of the physical properties and the location and shape of the anomalies were compared to the characterization maps (Rosado-Fuentes et al., 2021) to differentiate between false positives and anomalies that are related to the buried targets. With the comparison, some anomalies were ruled out since they are present in the site since its characterization and before TGTS was built. For both methods, the number of false positives decreases by adding the orthogonal-transect surveys, operating as a filter. Therefore, we can attribute isolated false positives in the MG maps (Fig. 2) to very shallow garbage debris, <0.50 m deep (Rosado-Fuentes et al., 2021) and in the EMIG maps to the presence of subsurface features that do not reflect the buried structures. In case there are no previous characterization maps of the site nor the knowledge of the location of the targets, as commonly happens in geophysical exploration studies, it would not be possible to differentiate these anomalies by semblance. Therefore, other differentiation techniques would have to be applied, e.g. digital filtering, establishing a threshold value on the anomalies or by correlating the results from different methods.

Table 1 outlines the results of the S–N, E–W and Sum survey maps for the MG (Fig. 2) and EMI conductivity and in-phase maps (top and middle maps in Figs. 3 and 4, respectively) for two main cases. In the first case, we assume that there is no previous knowledge about the location of the buried structures. If the features seen on the map reflect a buried structure, we highlight the cell of that structure with gray; if not, we leave the cell blank. In the second case, we know in advance the

location of the target. Thus, we can corroborate if the anomalies shown on the maps correspond to a buried structure or not. If the anomaly corresponds to a buried structure, we symbolize the cell of that structure with a check-mark; if it does not correspond to a buried structure, we symbolize the cell of that structure with an x-mark. There are some anomalies without a clear indication that they may or may not correspond to a buried structure, regardless if the feature shown on the maps is shifted from the center of the target; for these cases we mark the cell of the structure with an approximation-symbol. Note that having previous knowledge of the location of the buried structures leads to find the majority of them in all maps (Table 1). Such are the cases for structure 14 in the MG (Fig. 2) and EMI conductivity (top and middle maps in Fig. 3) maps and structure 10 in the EMI in-phase maps (top and middle maps in Fig. 4). Observe in the top and middle maps in Figs. 3–5 that some anomalies seem to be shifted from the center of the targets in <1.50 m. Some structures do not present enough contrast from the surroundings soils, like structure 13 in the MG and EMI conductivity maps and structure 7 in the EMI in-phase maps (Table 1). In brief, the Sum maps give better results than the individual survey maps, whether or not the location of the buried structures is included in the analysis (Table 1 and Sum maps in Figs. 2–4).

The depth to the base of structures 1–14 is around 1.02 m deep in average. For structures 15–17 the depth to their bases is 2.05 m, 1.66 m and 1.55 m deep, respectively. This means that the HCP mode maps a subsurface thickness where all the 17 features are embedded, and the VCP mode maps a subsurface thickness where structures 1–14 are embedded and structures 15–17 extend beyond the mapped depth. Since the used EMI device senses the contribution of a large volume of subsurface materials, several cubic meters, delimited by configuration-

Table 1

Outline of the results of the S–N, E–W and Sum survey maps for the Magnetic Gradiometry (MG) (Fig. 2) and Electromagnetic Induction (EMI) conductivity and in-phase maps (top and middle maps in Figs. 3 and 4, respectively) for two main cases. For the first case, assuming there is no previous knowledge about the location of the buried structures, we highlighted the cell of the target with gray if the features shown on the map reflect the buried structure. For the second case, having previous knowledge of the location of targets, we symbolize with a check-mark or an x-mark if the features shown on the map correspond or not, respectively, to a buried structure. If there is no clear indication that the features shown on the map correspond or not to a target, we mark those cells with an approximation-symbol.

Structure	MG			EMI Conductivity						EMI In-phase					
				VCP mode			HCP mode			VCP mode			HCP mode		
	S - N	E - W	Sum	S - N	E - W	Sum	S - N	E - W	Sum	S - N	E - W	Sum	S - N	E - W	Sum
1	✓	✓	✓	X	X	X	X	X	X	≈	X	✓	X	≈	≈
2	≈	≈	X	X	≈	X	X	X	X	≈	X	≈	✓	✓	✓
3	≈	≈	≈	X	≈	✓	≈	≈	≈	≈	≈	✓	≈	✓	≈
4	≈	✓	✓	X	✓	X	✓	✓	✓	X	X	≈	X	≈	≈
5	X	≈	≈	≈	≈	≈	X	≈	X	✓	X	✓	X	✓	≈
6	X	X	X	X	≈	X	X	X	X	≈	X	≈	X	≈	X
7	X	≈	≈	X	≈	X	≈	X	≈	X	X	X	X	X	X
8	X	X	X	≈	X	≈	X	X	X	✓	≈	≈	≈	≈	≈
9	✓	✓	✓	≈	X	≈	≈	✓	✓	≈	X	≈	X	X	X
10	≈	X	≈	X	X	X	X	X	X	≈	✓	✓	≈	≈	✓
11	X	≈	≈	≈	≈	✓	X	X	X	≈	≈	≈	≈	X	≈
12	X	≈	X	X	X	X	≈	X	X	≈	≈	✓	≈	X	≈
13	X	X	X	X	X	X	X	X	X	✓	X	✓	≈	X	≈
14	✓	≈	≈	✓	≈	≈	≈	≈	≈	≈	X	≈	≈	≈	X
15	✓	✓	✓	≈	X	≈	X	X	X	≈	X	≈	X	≈	≈
16	X	✓	≈	≈	X	≈	X	X	X	≈	≈	≈	X	≈	X
17	✓	X	≈	X	X	X	X	X	X	✓	X	✓	≈	≈	≈

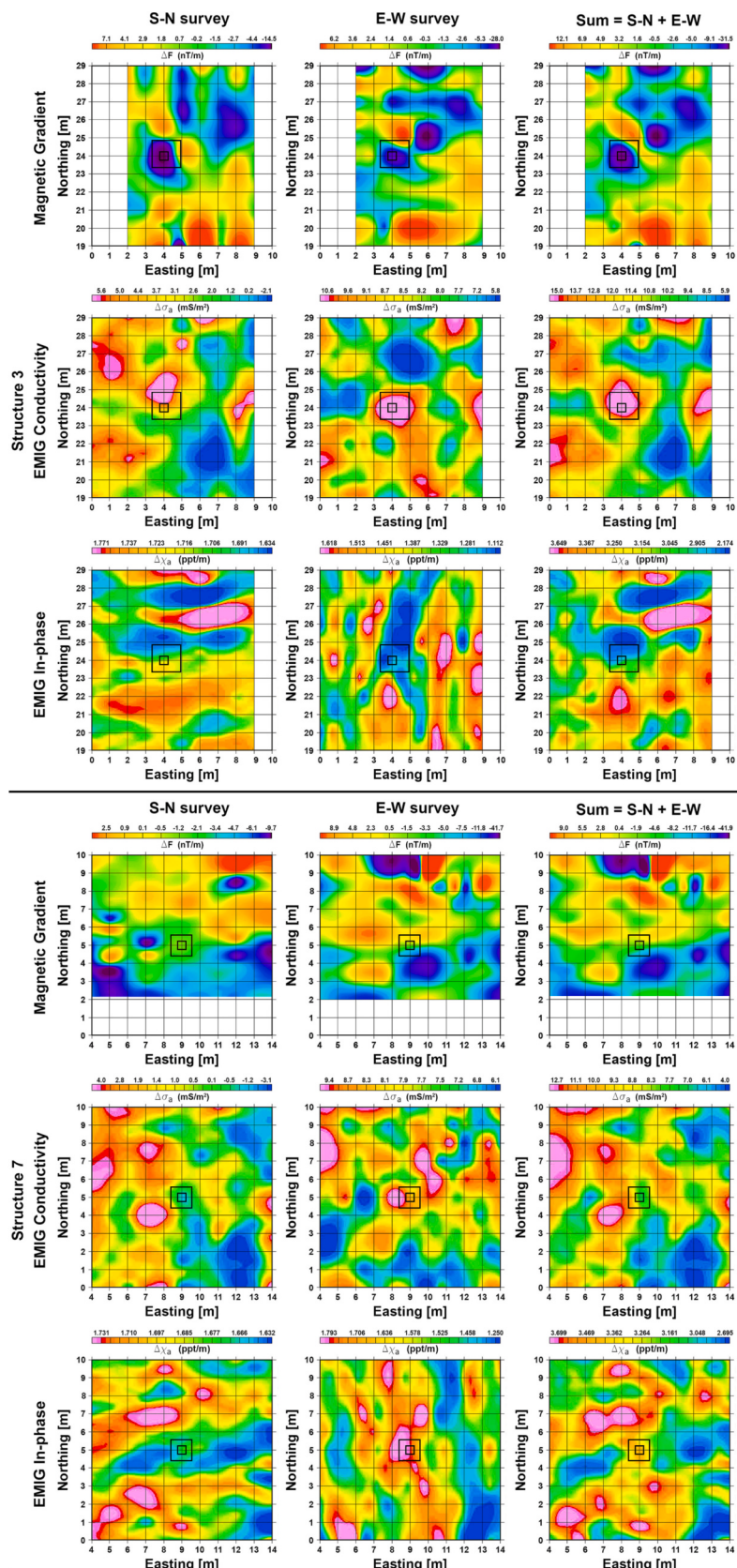


Fig. 5. S–N (left), E–W (central) and Sum (right) close-up maps for Magnetic Gradiometry (MG) (1st and 4th rows), Electromagnetic Induction Gradient (EMIG) apparent conductivity (2nd and 5th row) and EMIG in-phase (3rd and 6th row) measurements for structures 3 (top three rows) and 7 (bottom three rows). The plan views of the buried structures and the holes dug during construction are shown with black boxes. Color bars in each panel indicate the value range of the measured physical property. (For interpretation of the references to color in this figure legend, the reader is referred to the web version of this article.)

dependent depth of investigation and lateral footprint, the relatively small scale targets generate small data anomalies and consequently often go unnoticed. One way to enhance such small anomalies is to decrease the relatively large effect of the background medium. For this, we generated the S–N and E–W vertical gradient EMIG survey maps by using Eq. 4 and later added the grids as done before (bottom maps in Figs. 3 and 4). Additionally, close-up maps were generated to visualize each target individually and have more detail of their local effect. As an example, Fig. 5 shows the MG and EMIG conductivity and in-phase close-up maps for structures 3 and 7. The rest of the close-up maps can be consulted in the Supplementary data: Figs. S1, S2 and S3 for MG, Figs. S4, S5 and S6 for EMIG conductivity and Figs. S7, S8 and S9 for EMIG in-phase values.

Table 2 outlines the results of the S–N, E–W and the Sum surveys for the EMIG area maps (bottom maps in Figs. 3 and 4) and for the EMIG and MG close-up maps (Fig. 5 and Figs. S1–S9 in Supplementary data). Shaded cells and mark-symbols are described above for Table 1. For the area maps, without previous knowledge of the location of the buried structures most are clearly visible in the EMIG conductivity maps as high gradient values (Table 2 and bottom maps in Figs. 3). Contrary, in the EMIG in-phase maps few structures are visible and the maps are similar to the EMI VCP mode in-phase maps (Table 2 and top and bottom maps in Fig. 4). Considering the location of the targets, most of the buried structures are visible or can be associated to anomalies shown in the maps, although some seem to be shifted from the center of the targets in <1.50 m (Table 2 and bottom maps in Figs. 3 and 4). In all EMIG maps, structures 2 and 7 are the least clear. Regardless if the location of the buried structures is considered in the analysis, the best results are obtained by the Sum maps, then by the E–W maps and finally by the S–N maps.

MG and EMIG close-up maps reflect the structures better than the

area maps, especially in the case of the EMIG in-phase maps (Fig. 5 and Figs. S1–S9 in Supplementary data). As shown in the MG and EMI maps, S–N and E–W close-up maps show significant differences in the distribution of the values. In general, the best results in MG maps are obtained by the E–W maps, followed by the Sum maps and finally by the S–N maps. For EMIG maps, the Sum maps are better, followed by the E–W maps and finally by the S–N maps. Note that some anomalies still seem to be shifted from the center of the targets in <1.50 m. Most of the structures are shown as low-medium MG values and medium-high conductivity and in-phase EMIG values.

Structures 6–8 and 12 show the less magnetic contrast with their surroundings (Fig. 5 and Figs. S1 and S2 in Supplementary data), so does structures 2 and 7 in the EMIG conductivity maps (Fig. 5 and Fig. S4 in Supplementary data) and structure 8 in the EMIG in-phase map (Fig. S8 in Supplementary data). The results indicate that by changing the refilling material from *tepetate*, structure 2, to sand, structure 3, enhances the contrast of the anomaly with its surroundings, maintains the same MG value, increases the conductivity value and decreases the in-phase value (Fig. 5 and Figs. S1, S4 and S7 in Supplementary data). The anomalies of the concrete structures are consistent with each other, they are seen as low MG values and, in general, medium-high conductivity and in-phase EMIG values (Fig. 5 and Figs. S1, S2, S4, S5, S7 and S8 in Supplementary data). The same is observed in structures with air, except for the high MG value of structure 9 (Figs. S2, S3, S5, S6, S8 and S9 in Supplementary data). In general, structures 14, 16 and 17 show varying MG and EMIG values that account for the different materials used in their construction, the thickness of the refilling material or the geometry of the structures. The anomalies of structure 16 are mostly controlled by its concrete and basalt cubes (Figs. S3, S6 and S9 in Supplementary data).

We believe that the results and the interpretation shown in this study

Table 2

Outline of the results of the S–N, E–W and the Sum surveys for the Electromagnetic Induction Gradient (EMIG) area maps (bottom maps in Figs. 3 and 4) and the EMIG and Magnetic Gradiometry (MG) close-up maps (Fig. 5 and Figs. S1–S9 in Supplementary data) for two main cases. For the first case, assuming there is no previous knowledge about the location of the buried structures, we highlighted the cell of the target with gray if the features shown on the map reflect the buried structure. For the second case, having previous knowledge of the location of targets, we symbolize with a check-mark or a x-mark if the features shown on the map correspond or not, respectively, to a buried structure. If there is no clear indication that the features shown on the map correspond or not to a target, we mark those cells with an approximation-symbol.

Structure	Area maps									Close-up maps								
	Electromagnetic Induction Gradient - EMIG									MG								
	Conductivity			In-phase			Conductivity			In-phase			S-N	E-W	Sum	S-N	E-W	Sum
	S-N	E-W	Sum	S-N	E-W	Sum	S-N	E-W	Sum	S-N	E-W	Sum	S-N	E-W	Sum	S-N	E-W	Sum
1	≈	✓	✓	✓	x	✓	≈	✓	✓	≈	x	✓	✓	✓	✓	✓	✓	✓
2	x	x	≈	x	x	x	x	x	≈	≈	x	≈	≈	≈	≈	≈	≈	≈
3	✓	✓	✓	✓	≈	✓	✓	✓	✓	≈	✓	✓	✓	✓	✓	✓	✓	✓
4	✓	✓	✓	x	x	≈	✓	✓	✓	≈	x	✓	✓	✓	✓	✓	✓	✓
5	✓	✓	✓	✓	≈	x	✓	✓	✓	≈	x	≈	≈	≈	≈	≈	≈	≈
6	✓	✓	✓	x	≈	≈	✓	✓	✓	x	≈	≈	≈	≈	≈	x	x	x
7	x	≈	x	x	x	x	≈	≈	≈	x	≈	x	x	x	x	≈	≈	≈
8	≈	✓	✓	x	✓	≈	≈	✓	✓	x	✓	✓	x	x	x	≈	≈	≈
9	✓	✓	✓	≈	x	≈	✓	✓	✓	≈	x	≈	x	✓	✓	✓	✓	✓
10	✓	✓	✓	≈	✓	≈	✓	✓	✓	≈	✓	✓	✓	✓	✓	≈	x	≈
11	✓	x	✓	x	≈	≈	✓	x	✓	≈	≈	≈	≈	✓	✓	✓	✓	✓
12	✓	✓	✓	x	≈	≈	≈	≈	≈	x	✓	✓	✓	✓	x	≈	≈	≈
13	✓	≈	✓	✓	✓	x	✓	≈	≈	✓	✓	✓	✓	x	≈	✓	≈	≈
14	✓	✓	✓	x	≈	≈	x	≈	✓	✓	✓	✓	≈	≈	≈	≈	≈	≈
15	✓	x	≈	≈	≈	≈	x	≈	✓	x	≈	✓	✓	✓	✓	✓	✓	✓
16	✓	✓	✓	✓	≈	≈	✓	✓	✓	✓	✓	✓	✓	✓	✓	✓	≈	≈
17	x	✓	≈	≈	✓	x	✓	x	✓	≈	✓	✓	x	✓	✓	✓	✓	✓

can be enhanced by replicating the surveys with higher sampling rate and reducing the transect spacing to 0.50 m instead of 1.00 m. We also want to test surveys following a grid that has a different orientation than the S–N and E–W grids mentioned in this study. Additionally, we continue applying different geophysical techniques in TGTS in order to investigate and compare the capabilities of the techniques to retrieve the response of very shallow buried structures like those encountered in engineering and archaeological contexts.

6. Conclusions

In this study we applied conventional MG and EMI surveys and a novel Electromagnetic Induction Gradient (EMIG) technique to map and identify the 17 buried structures in TGTS, Central Mexico. The aim is to determine the differences and similarities of the geophysical response of the 17 buried structures and to complement an acquisition and processing technique for near-surface studies in engineering and archaeological contexts. The presented data acquisition and processing methodology mainly consists in acquiring orthogonal-transect surveys and adding the grids together. This methodology has proven to give maps that are more in accordance with the expected distribution of EMI properties (Guillemoteau and Tronicek, 2015). In this study we prove that this methodology also works with MG surveys, and we complement it by calculating the EMIG and making close-up maps.

The magnetic and electromagnetic properties of the subsoil have not changed significantly since the site characterization studies that were made prior to the construction of the site (Rosado-Fuentes et al., 2021). We showed how most of the buried structures are overlooked when using conventional MG and EMI data. Also, the comparison of orthogonal-transect surveys reflects notable differences in the sensors' responses that are shown as distinct distribution of the values of the physical properties of the subsoil. Such distributions are due to the acquisition direction, the orientation of the transects and to the orientation and heading of the sensors (Figs. 2–4). The possible contribution of anisotropic effects of the buried structures should not be discarded, they have to be studied in detail but are out of the scope of the present study. The EMIG technique has remarkable results in the conductivity maps but presents limited results in the in-phase maps (Figs. 3 and 4). This could be explained by the fact that the in-phase component depth sensitivity of standard coil configurations have different distributions and complex changes of sign (Guillemoteau et al., 2019; Klose et al., 2018) in contrast with the positive and more alike distributions of the out-of-phase component depth sensitivity (McNeill, 1980; McNeill and Bosnar, 1999). Similarly to MG, the EMIG enhances near-surface and local sources. With the applied methodology, we demonstrate that most of the buried structures could be retrieved, regardless if the location of the target is considered in the analysis and if redundant information is generated. In area and close-up maps, better results are obtained from the Sum maps, followed by the E–W maps and finally by the S–N maps. However, close-up maps retrieve the location of the structures better than the area maps (Figs. 2–5, Figs. S1–S9 in Supplementary data and Tables 1 and 2).

In general, the anomalies do not reflect differences between the structures and the excavated and refilling areas. Most of the structures are shown as low-medium MG values and medium-high EMIG conductivity and in-phase values, few do not generate enough contrast with their surroundings and some anomalies seem to be shifted from the center of the targets in <1.50 m. Our results are consistent among concrete and air-cavity structures. Anomaly variations reflect the different materials composition, the thickness of the refilling material or the complex geometry of structures 14, 16 and 17. Also, the anomalies of structure 16 are governed by its basalt and concrete cubes. In terrains like TGTS, refilling the construction hole with sand instead of *tepetate* enhances the anomaly, maintains similar magnetic values, increases conductivity and decreases in-phase values (Figs. 2–5 and S1–S9 in Supplementary data).

Our results demonstrate that the applied methodology yields better MG, EMI and EMIG results than common-practice approaches. Therefore, we strongly recommend to replicate it in near-surface studies elsewhere. Our research team continues to carry out geophysical surveys in TGTS to study and compare the response of the buried structures. The site is available for educational, industrial and academic use upon request to the authors and the Institute of Geophysics, Universidad Nacional Autónoma de México.

Funding statement

This work was supported by Dirección General de Asuntos de Personal Académico (DGAPA), Universidad Nacional Autónoma de México through DGAPA-PAPIIT projects IN105716 and IN108219. Author Rosado-Fuentes received a grant from CONACYT under Grant Agreement No. 620517/336033.

CRediT authorship contribution statement

Alejandro Rosado-Fuentes: Conceptualization, Data curation, Formal analysis, Funding acquisition, Investigation, Methodology, Project administration, Resources, Supervision, Validation, Visualization, Writing – original draft, Writing – review & editing. **Alejandra Arciniega-Ceballos:** Funding acquisition, Project administration, Resources, Supervision, Conceptualization, Writing - review & editing. **Esteban Hernández-Quintero:** Conceptualization, Investigation, Methodology, Resources, Validation, Writing – review & editing. **Claudia Arango-Galván:** Conceptualization, Investigation, Resources, Validation, Writing – review & editing. **José Luis Salas-Corralles:** Investigation, Resources, Validation, Writing – review & editing. **Gerardo Mendo-Pérez:** Validation, Writing – review & editing.

Declaration of Competing Interest

The authors have no competing financial interests or personal relationships to declare that are relevant to the content of this article or that could have appeared to influence the work reported in this paper.

Data availability

The datasets that support the findings of this article are available from the corresponding author upon request.

Acknowledgements

The authors acknowledge the Instituto de Geofísica, Universidad Nacional Autónoma de México for supporting this idea and allowing us to continue our near-surface geophysics research in Teoloyucan Geophysical Test Site within the Teoloyucan Geomagnetic Observatory. Author Rosado-Fuentes, A. thanks Posgrado en Ciencias de la Tierra, UNAM and Grupo MARQ for their support. We thank the anonymous reviewers for their useful comments and the review of this paper.

Appendix A. Supplementary data

Supplementary data to this article can be found online at <https://doi.org/10.1016/j.jappgeo.2023.105123>.

References

- Allred, B.J., Fausey, N.R., Peters, L., Chen, C., Daniels, J.J., Youn, H., 2004. Detection of buried agricultural drainage pipe with geophysical methods. *Appl. Eng. Agric.* 20 (3), 307–318. <https://doi.org/10.13031/2013.16067>.
- Cheyney, S., Hill, I., Linford, N., Fishwick, S., 2012. New approach to directional filtering of near-surface magnetic data. *Near Surf. Geophys.* 10 (5), 359–367. <https://doi.org/10.3997/1873-0604.2012035>.

- De Smedt, P., Saey, T., Meerschman, E., De Reu, J., De Clercq, W., Van Meirvenne, M., 2014. Comparing apparent magnetic susceptibility measurements of a multi-receiver EMI sensor with topsoil and profile magnetic susceptibility data over weak magnetic anomalies. *Archaeol. Prospect.* 21 (2), 103–112. <https://doi.org/10.1002/arp.1467>.
- Everett, M.E., 2013. Near-surface Applied Geophysics. Cambridge University Press. <https://doi.org/10.1017/CBO9781139088435>.
- Fedi, M., Florio, G., 2003. Decorrelation and removal of directional trends of magnetic fields by the wavelet transform: Application to archaeological areas. *Geophys. Prospect.* 51 (4), 261–272. <https://doi.org/10.1046/j.1365-2478.2003.00373.x>.
- Ferraccioli, F., Gambetta, M., Bozzo, E., 1998. Microlevelling procedures applied to regional aeromagnetic data: an example from the Transantarctic Mountains (Antarctica). *Geophys. Prospect.* 46 (2), 177–196. <https://doi.org/10.1046/j.1365-2478.1998.00080.x>.
- Geosoft, 2007. Montaj Magmap Filtering: 2D Frequency Domain Processing of Potential Field Data. Tutorial and User Guide. Geosoft Inc.
- GF Instruments, 2020. Short Guide for Electromagnetic Conductivity Mapping and Tomography. GF Instruments, S.R.O. Retrieved from <http://www.gfinstruments.cz>. Accessed October 15, 2022.
- Guillemoteau, J., Tronicke, J., 2015. Non-standard electromagnetic induction sensor configurations: evaluating sensitivities and applicability. *J. Appl. Geophys.* 118, 15–23. <https://doi.org/10.1016/j.jappgeo.2015.04.008>.
- Guillemoteau, J., Simon, F.X., Lück, E., Tronicke, J., 2016. 1D sequential inversion of portable multi-configuration electromagnetic induction data. *Near Surface Geophysics* 14 (5), 423–432. <https://doi.org/10.3997/1873-0604.2016029>.
- Guillemoteau, J., Christensen, N.B., Jacobsen, B.H., Tronicke, J., 2017. Fast 3D multichannel deconvolution of electromagnetic induction loop-loop apparent conductivity data sets acquired at low induction numbers. *Geophysics* 82 (6), E357–E369. <https://doi.org/10.1190/geo2016-0518.1>.
- Guillemoteau, J., Simon, F.X., Hulin, G., Dousteyssier, B., Dacko, M., Tronicke, J., 2019. 3-D imaging of subsurface magnetic permeability/susceptibility with portable frequency domain electromagnetic sensors for near surface exploration. *Geophys. J. Int.* 219 (3), 1773–1785. <https://doi.org/10.1093/gji/ggz382>.
- Haas, A.G., Viallix, J.R., 1976. Krigeage applied to geophysics: the answer to the problem of estimated and contouring. *Geophys. Prospect.* 24 (1), 49–69. <https://doi.org/10.1111/j.1365-2478.1976.tb00384.x>.
- Hanssens, D., Delefortrie, S., Bobe, C., Hermans, T., De Smedt, P., 2019. Improving the reliability of soil EC-mapping: Robust apparent electrical conductivity (rECa) estimation in ground-based frequency domain electromagnetics. *Geoderma* 337, 1155–1163. <https://doi.org/10.1016/j.geoderma.2018.11.030>.
- Hinze, W.J., Von Frese, R.R.B., Saad, A.H., 2013. Gravity and Magnetic Exploration: Principles, Practices, and Applications. Cambridge University Press. <https://doi.org/10.1017/CBO9780511843129>.
- Hrvoic, I., Hollyer, G.M., 2005. Brief review of quantum magnetometers. In: GEM Systems Technical Papers.. Retrieved from <https://www.gemsys.ca>. Accessed May 15, 2023.
- Huang, H., Won, I.J., 2001. Conductivity and susceptibility mapping using broadband electromagnetic sensors. In: Symposium on the Application of Geophysics to Engineering and Environmental Problems 2001 (pp. EEM3-EEM3). Society of Exploration Geophysicists. <https://doi.org/10.4133/1.2922875>.
- Jankowski, J., Sucksdorff, C., 1996. IAGA guide for magnetic measurements and observatory practice. International Association of Geomagnetism and Aeronomy (IAGA). Retrieved from <https://www.iaga-aiga.org/>. Accessed October 20, 2022.
- Klose, T., Guillemoteau, J., Simon, F.X., Tronicke, J., 2018. Toward subsurface magnetic permeability imaging with electromagnetic induction sensors: Sensitivity computation and reconstruction of measured data. *Geophysics* 83 (5), E335–E345. <https://doi.org/10.1190/geo2017-0827.1>.
- Kvamme, K.L., 2006. Integrating multidimensional geophysical data. *Archaeol. Prospect.* 13 (1), 57–72. <https://doi.org/10.1002/arp.268>.
- Langel, R.A., Hinze, W.J., 1998. The magnetic field of the Earth's lithosphere: the satellite perspective. Cambridge University Press. <https://doi.org/10.1017/CBO9780511629549>.
- McNeill, J.D., 1980. Electromagnetic terrain conductivity measurements at low induction numbers. Technical Note TN-6, 5–15. Geonics Limited. Retrieved from <http://www.geonics.com/pdfs/technicalnotes/tn6.pdf>. Accessed October 20, 2022.
- McNeill, J.D., Bosnar, M., 1999. Application of 'Dipole-Dipole' Electromagnetic Systems for Geological Depth Sounding. Technical Note TN-31, 1–1. Geonics Limited7. Retrieved from <http://www.geonics.com/pdfs/technicalnotes/tn31.pdf>. Accessed November 20, 2022.
- Milsom, J., 2003. *Field Geophysics, the Geological Field Guide Series*, , 3rd ednvol. 25. John Wiley and Sons.
- Pringle, J.K., Jervis, J., Cassella, J.P., Cassidy, N.J., 2008. Time-Lapse Geophysical Investigations over a simulated Urban Clandestine Grave. *J. Forensic Sci.* 53 (6), 1405–1416. <https://doi.org/10.1111/j.1556-4029.2008.00884.x>.
- Pueyo Anchuela, Ó., Casas Sainz, A.M., Pacoví Juan, A., Gil Garbí, H., 2015. Assessing karst hazards in urbanized areas. Case study and methodological considerations in the mantle karst front from Zaragoza city (NE Spain). *Eng. Geol.* 184, 29–42. <https://doi.org/10.1016/j.engeo.2014.10.025>.
- Rosado-Fuentes, A., Arciniega-Ceballos, A., Hernández-Quintero, E., Arango-Gálván, C., Salas-Corrales, J.L., Mendo-Pérez, G., 2021. Geophysical characterization, design and construction of the Teoloyucan Geophysical Test Site for archaeological and engineering applications, Central Mexico. *J. Appl. Geophys.* 194, 104459 <https://doi.org/10.1016/j.jappgeo.2021.104459>.
- Rucker, D.F., 2010. The application of magnetic gradiometry and electromagnetic induction at a former radioactive waste disposal site. *Waste Manag. Res.* 28 (4), 364–372. <https://doi.org/10.1177/0734242X09357079>.
- Silván-Cárdenas, J.L., Caccavari-Garza, A., Quinto-Sánchez, M.E., Madrigal-Gómez, J.M., Coronado-Juárez, E., Quiroz-Suarez, D., 2021. Assessing optical remote sensing for grave detection. *Forensic Sci. Int.* 329, 111064 <https://doi.org/10.1016/j.forsciint.2021.111064>.
- Simpson, D., Van Meirvenne, M., Saey, T., Vermeersch, H., Bourgeois, J., Lehock, A., Cockx, L., Vitharana, U.W.A., 2009. Evaluating the multiple coil configurations of the EM38DD and DUALEM-21S sensors to detect archaeological anomalies. *Archaeol. Prospect.* 16 (2), 91–102. <https://doi.org/10.1002/arp.349>.
- Simpson, D., Van Meirvenne, M., Lück, E., Rühlmann, J., Saey, T., Bourgeois, J., 2010. Sensitivity of multi-coil frequency domain electromagnetic induction sensors to map soil magnetic susceptibility. *Eur. J. Soil Sci.* 61 (4), 469–478. <https://doi.org/10.1111/j.1365-2389.2010.01261.x>.
- Spies, B.R., Frischknecht, F.C., 1991. Electromagnetic sounding. In: Nabighian, M.N. (Ed.), *Electromagnetic Methods in Applied Geophysics*, Volume 2, Application, Parts A and B. Society of Exploration Geophysicists, pp. 285–425. <https://doi.org/10.1190/1.9781560802686.ch5>.
- Telford, W.M., Geldart, L.P., Sheriff, R.E., 1990. *Applied Geophysics*. Cambridge University Press. <https://doi.org/10.1017/CBO9781139167932>.
- Wamala, A.M., Serpa, L.F., Doser, D.I., 2011. Investigations of ground water flow associated with the Saratoga warm springs and the Tecopa Hot Springs near Death Valley, California, using magnetic and conductivity methods. *Tectonophysics* 502 (3–4), 267–275. <https://doi.org/10.1016/j.tecto.2010.12.001>.
- Zebrowski, C., 1992. Los suelos volcánicos endurecidos en América Latina. *Terra* 10, 15–23. Retrieved from <https://horizon.documentation.ird.fr/>. Accessed May 15, 2023.

2.4 Material suplementario

Supplemented Material

Article title:

Mapping near-surface structures in a geophysical test site using magnetic and electromagnetic induction gradients

Journal name: **Journal of Applied Geophysics**

Authors and affiliation:

Alejandro Rosado-Fuentes^{1*} (arosadof@ciencias.unam.mx, ORCID: 0000-0001-5898-3968)
Arciniega-Ceballos, Alejandra² (ORCID: 0000-0002-0180-5447)
Hernández-Quintero, Esteban² (ORCID: 0000-0001-5766-2572)
Arango-Galván, Claudia² (ORCID: 0000-0002-2988-5303)
Mendo-Pérez, Gerardo¹ (ORCID: 0000-0002-5239-4377)
Salas-Corrales, José Luis²

1 Posgrado en Ciencias de la Tierra, Universidad Nacional Autónoma de México, 04510, CDMX, Mexico

2 Instituto de Geofísica, Universidad Nacional Autónoma de México, 04510, CDMX, Mexico

* corresponding author

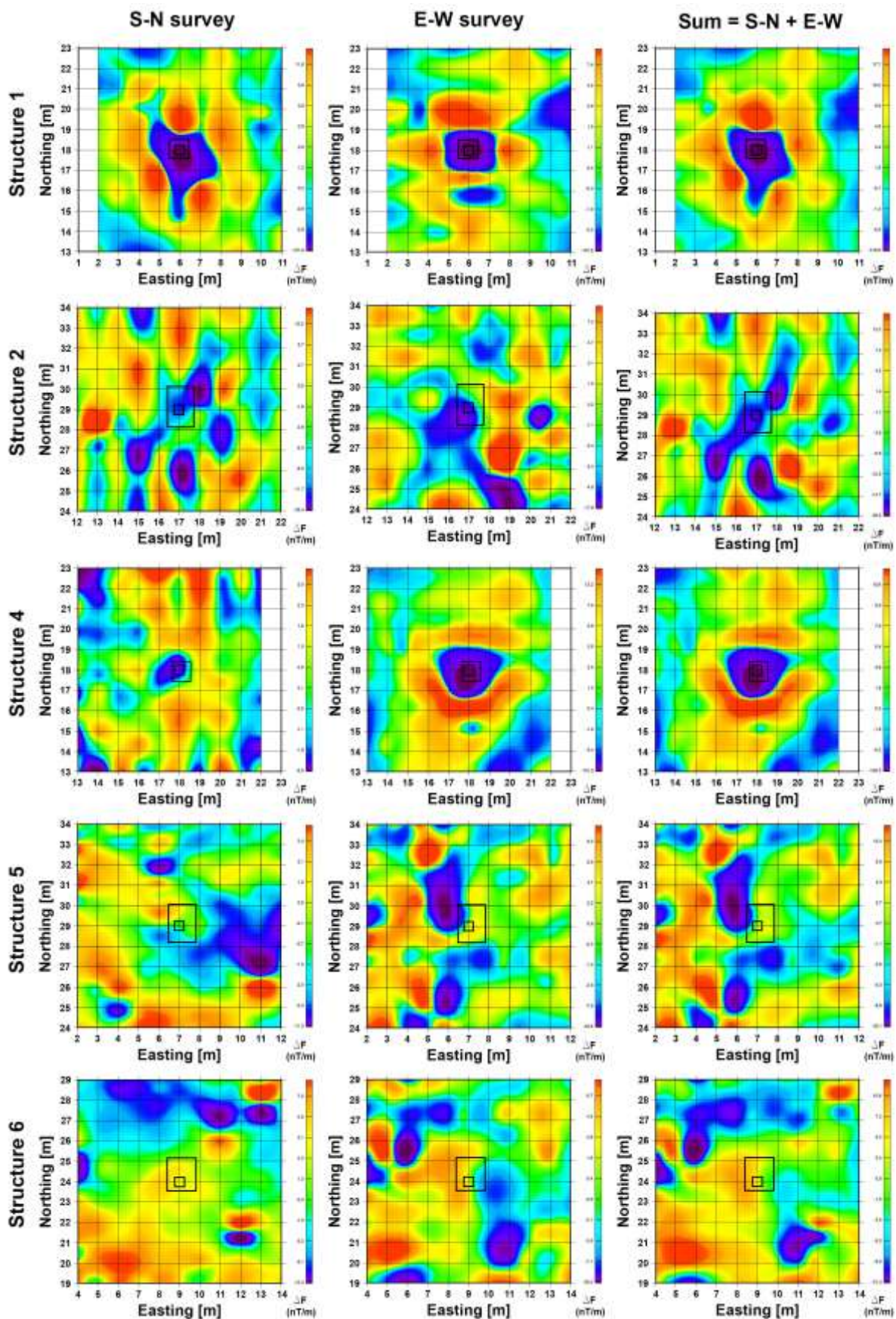


Figure S1. S-N (left), E-W (central) and Sum (right) Magnetic Gradiometry (MG) close-up maps for structures 1-2 and 4-6. The plan views of the buried structures and the holes dug during construction are shown with black polygons. Color bars in each panel indicate the magnetic gradient value range.

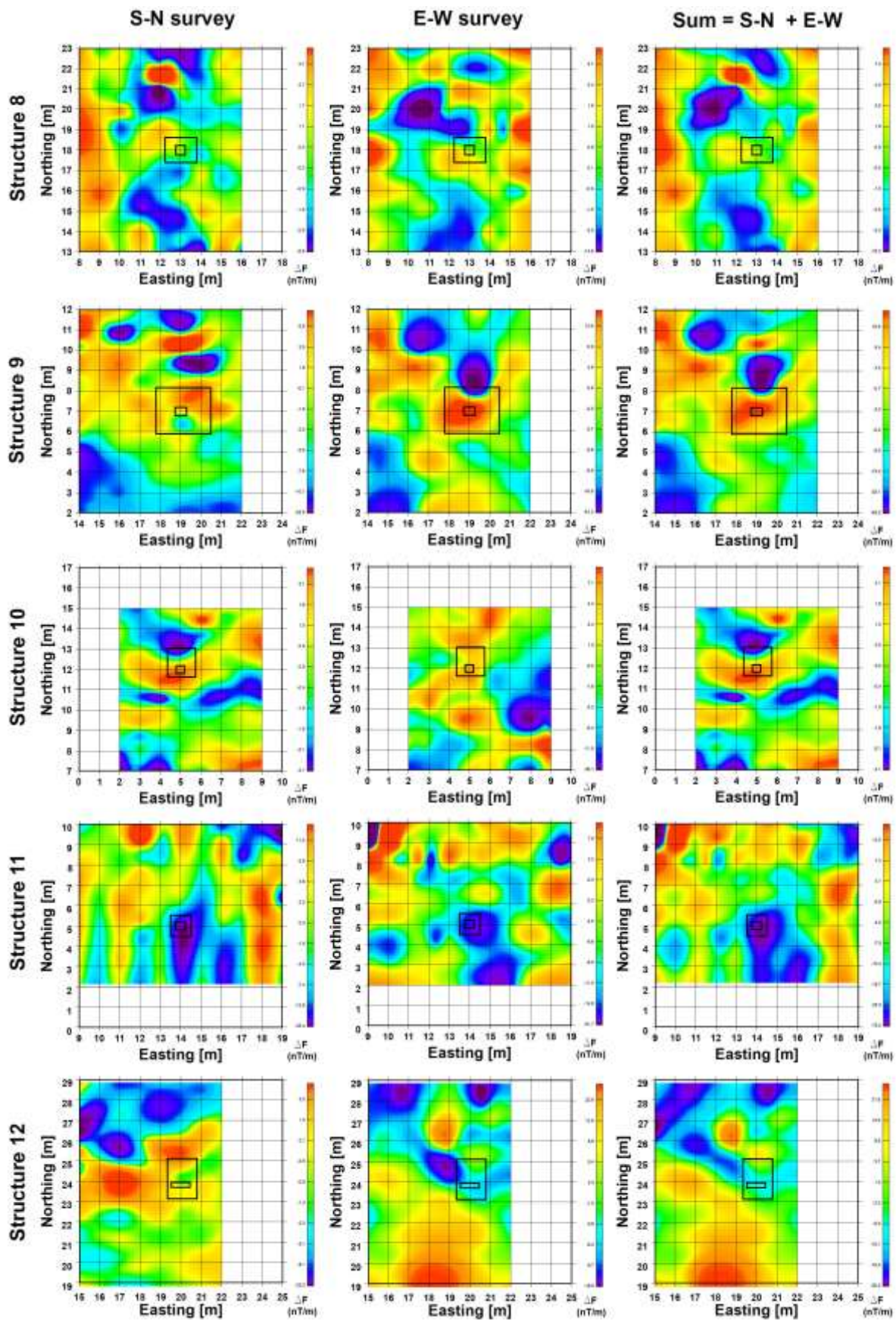


Figure S2. S-N (left), E-W (central) and Sum (right) Magnetic Gradiometry (MG) close-up maps for structures 8-12. The plan views of the buried structures and the holes dug during construction are shown with black polygons. Color bars in each panel indicate the magnetic gradient value range.

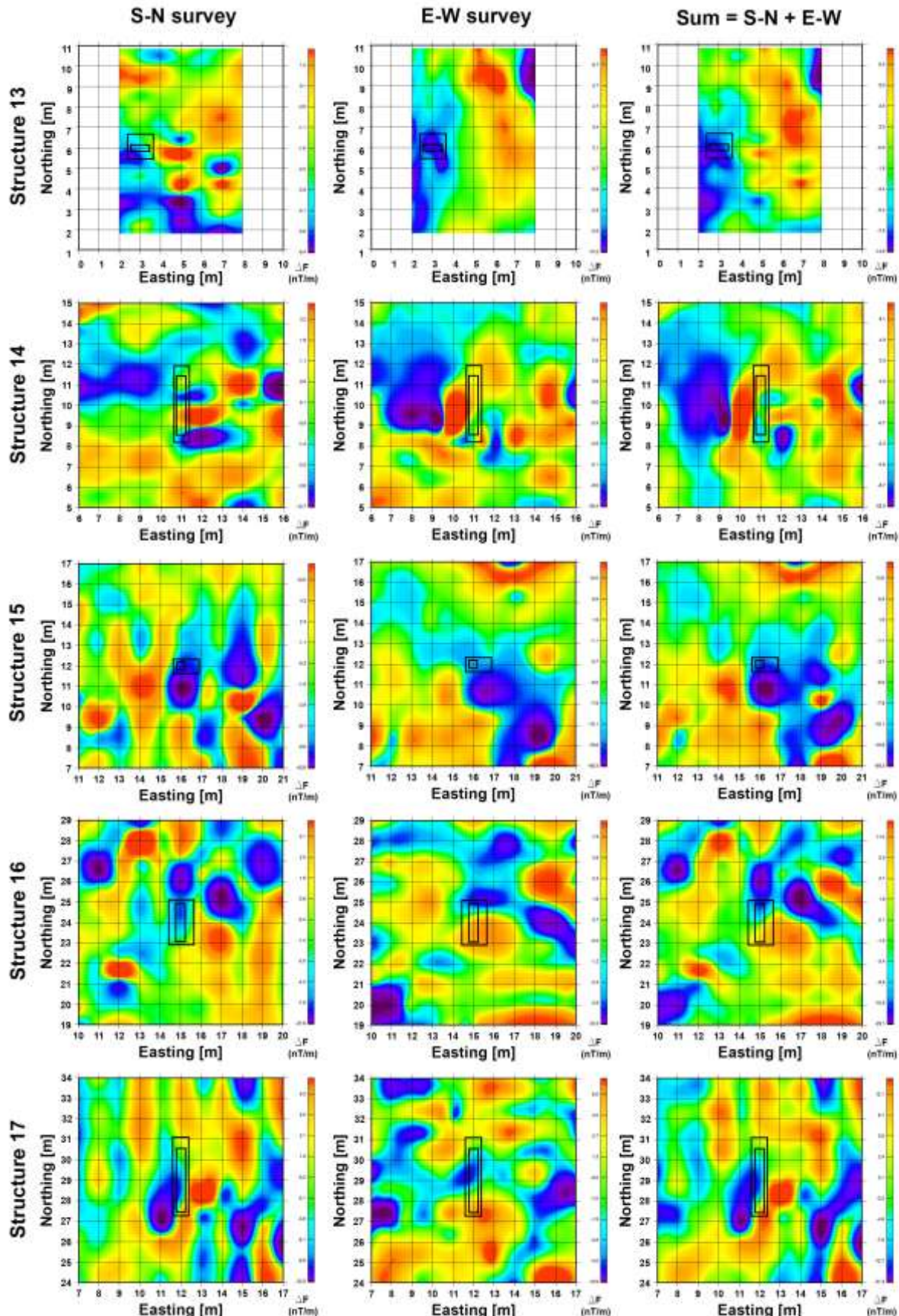


Figure S3. S-N (left), E-W (central) and Sum (right) Magnetic Gradiometry (MG) close-up maps for structures 13-17. The plan views of the buried structures and the holes dug during construction are shown with black polygons. Color bars in each panel indicate the magnetic gradient value range.

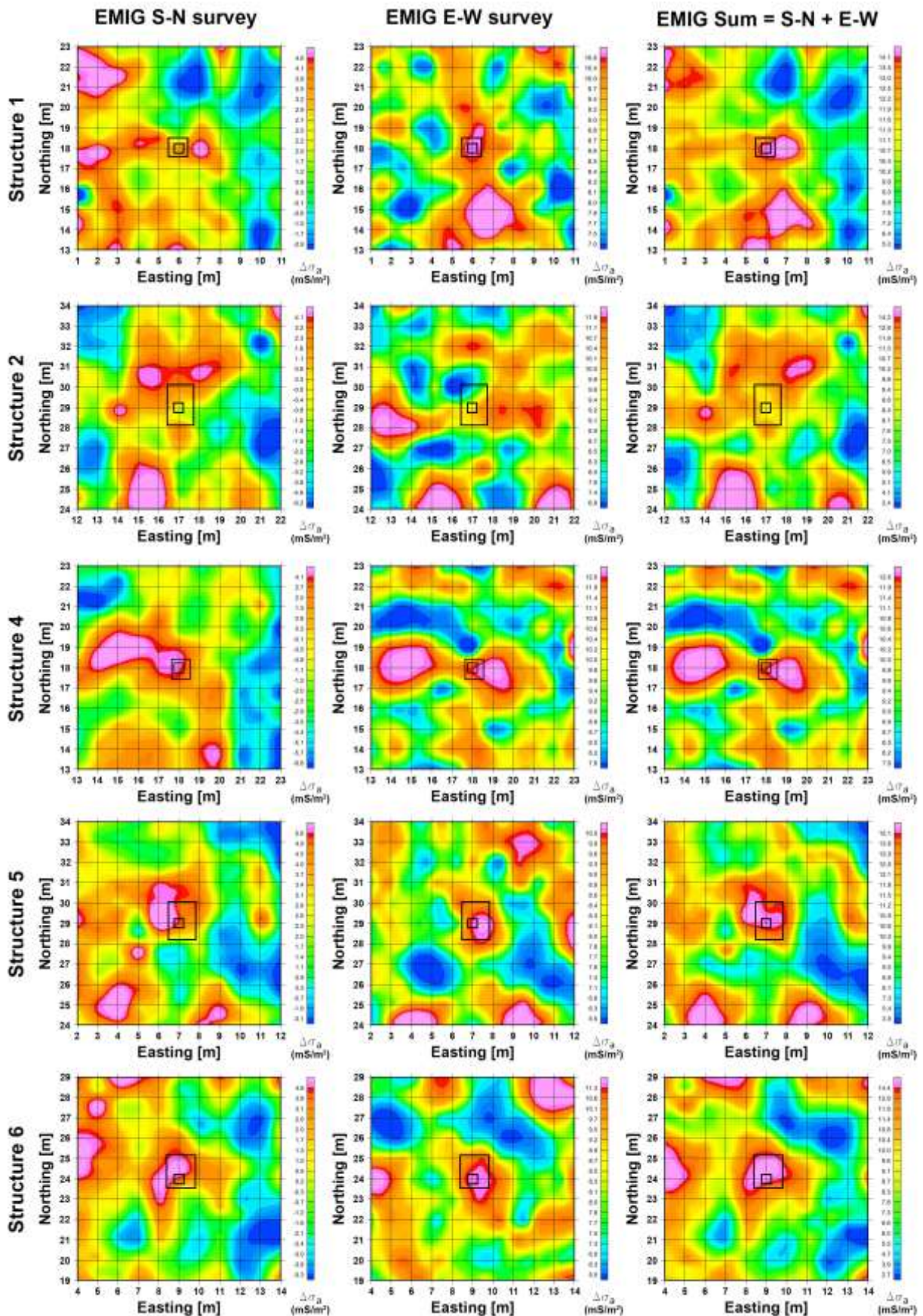


Figure S4. S-N (left), E-W (central) and Sum (right) Electromagnetic Induction Gradient (EMIG) conductivity close-up maps for structures 1-2 and 4-6. The plan views of the buried structures and the holes dug during construction are shown with black polygons.

Color bars in each panel indicate the conductivity gradient value range.

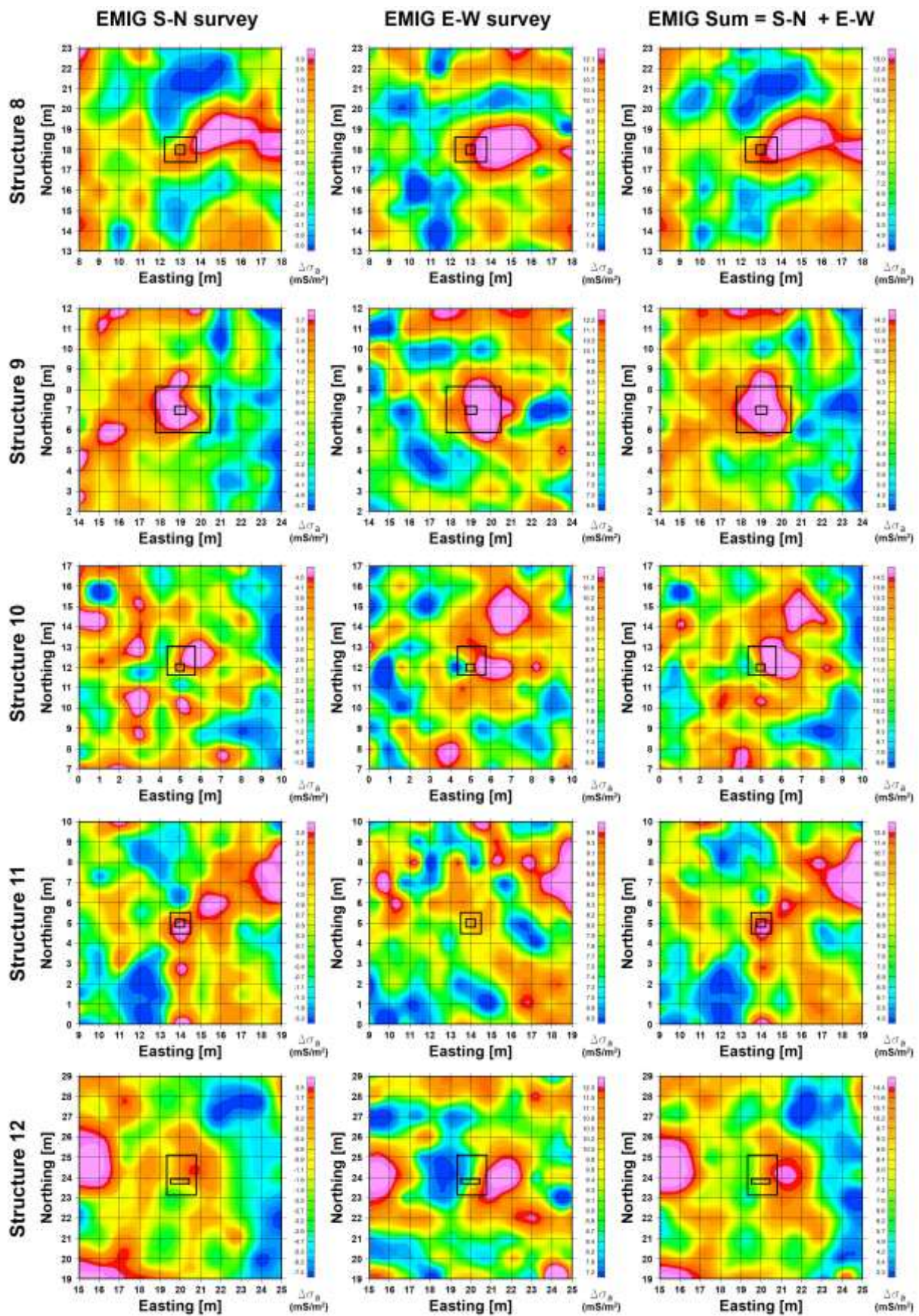


Figure S5. S-N (left), E-W (central) and Sum (right) Electromagnetic Induction Gradient (EMIG) conductivity close-up maps for structures 8-12. The plan views of the buried structures and the holes dug during construction are shown with black polygons. Color bars in each panel indicate the conductivity gradient value range.

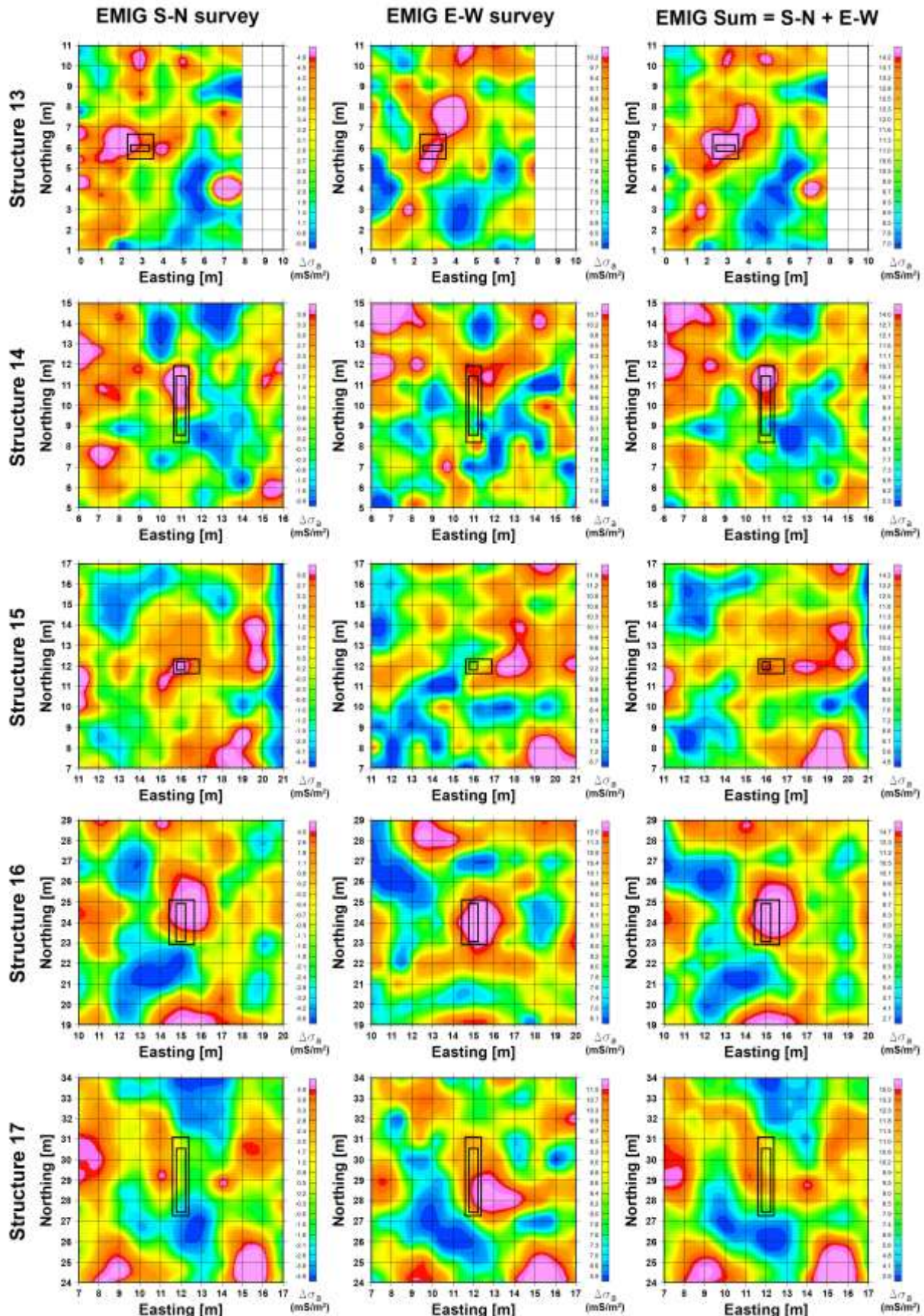


Figure S6. S-N (left), E-W (central) and Sum (right) Electromagnetic Induction Gradient (EMIG) conductivity close-up maps for structures 13-17. The plan views of the buried structures and the holes dug during construction are shown with black polygons. Color bars in each panel indicate the conductivity gradient value range.

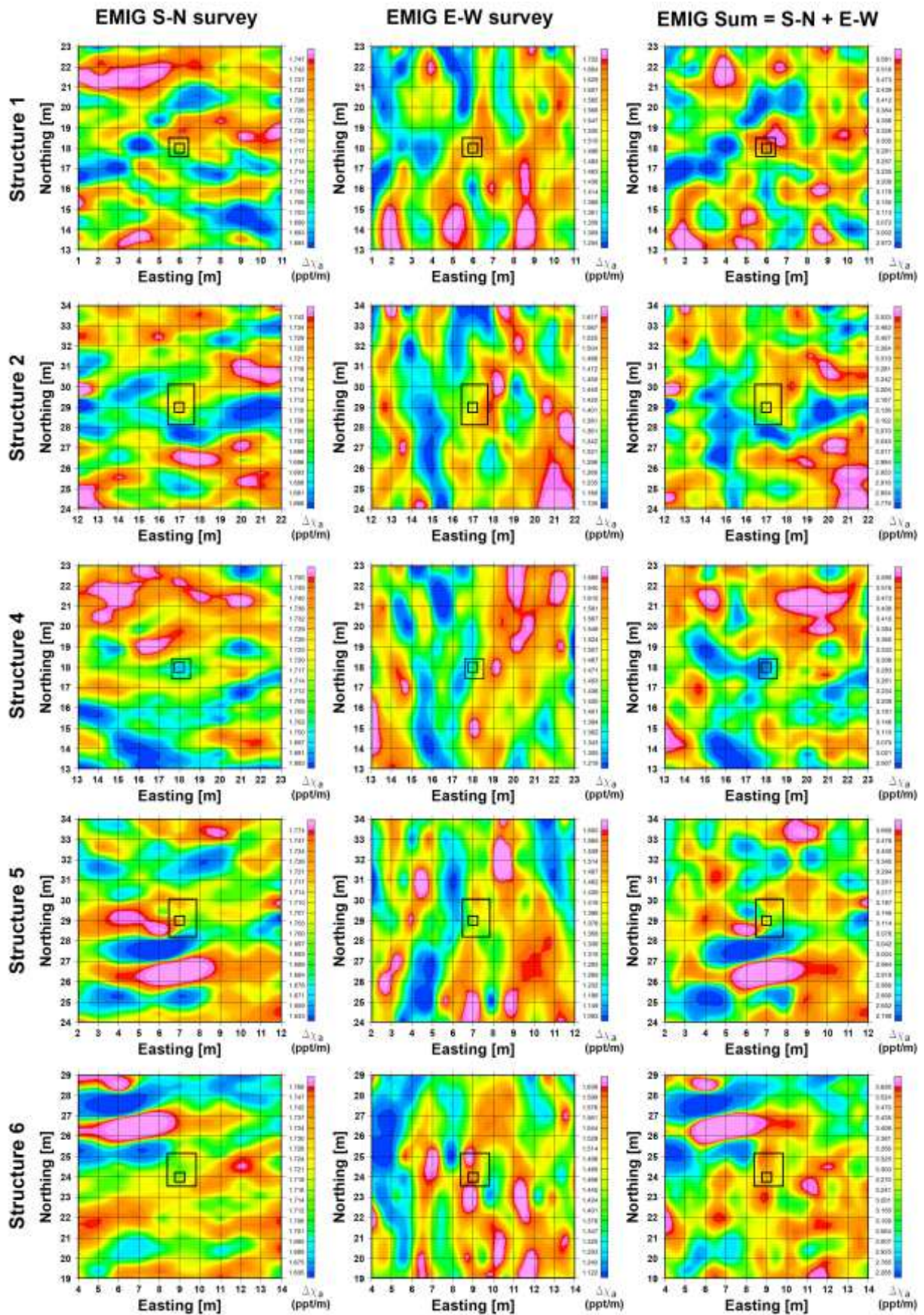


Figure S7. S-N (left), E-W (central) and Sum (right) Electromagnetic Induction Gradient (EMIG) in-phase close-up maps for structures 1-2 and 4-6. The plan views of the buried structures and the holes dug during construction are shown with black polygons.

Color bars in each panel indicate the in-phase gradient value range.

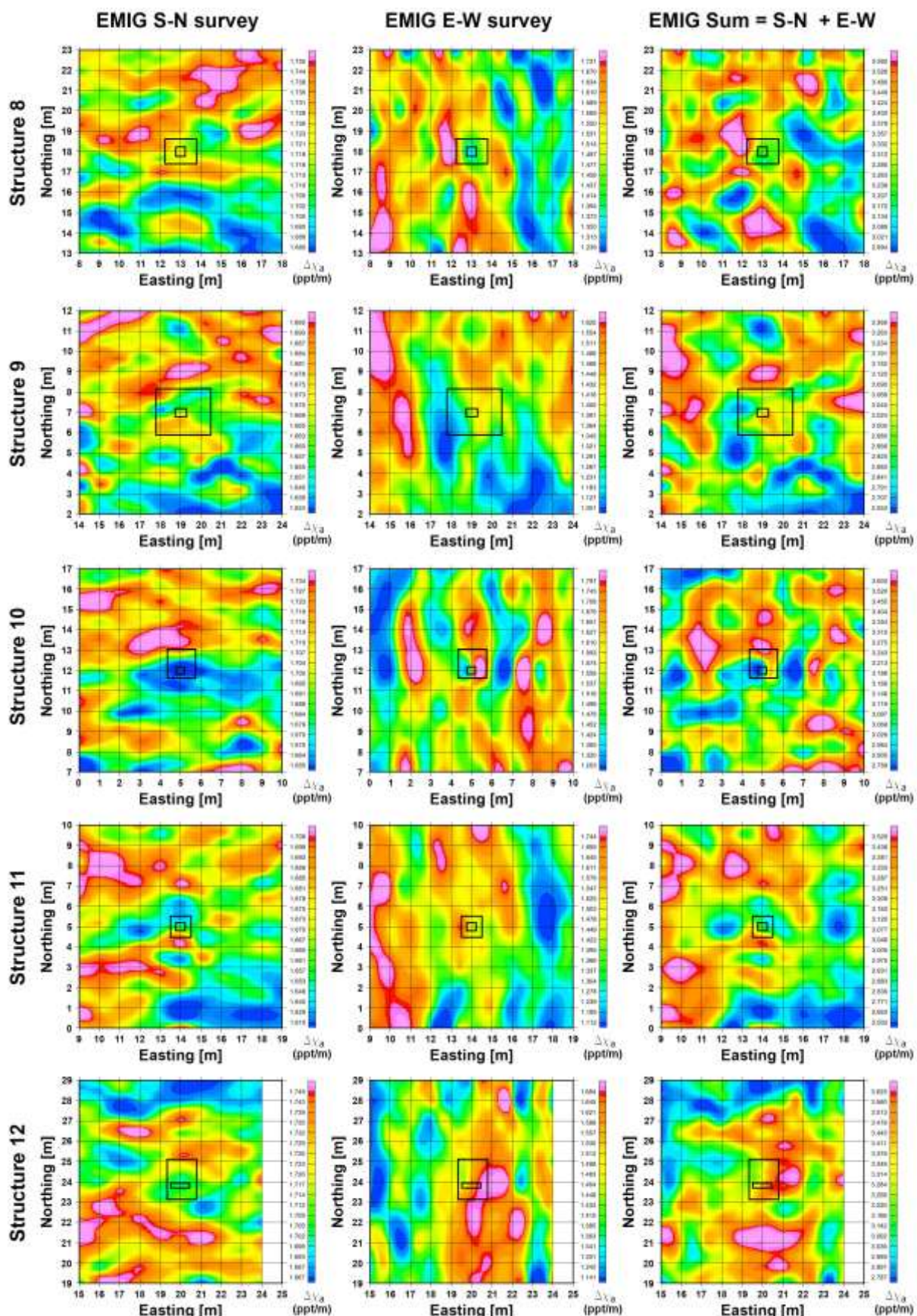


Figure S8. S-N (left), E-W (central) and Sum (right) Electromagnetic Induction Gradient (EMIG) in-phase close-up maps for structures 8-12. The plan views of the buried structures and the holes dug during construction are shown with black polygons. Color bars in each panel indicate the in-phase gradient value range.

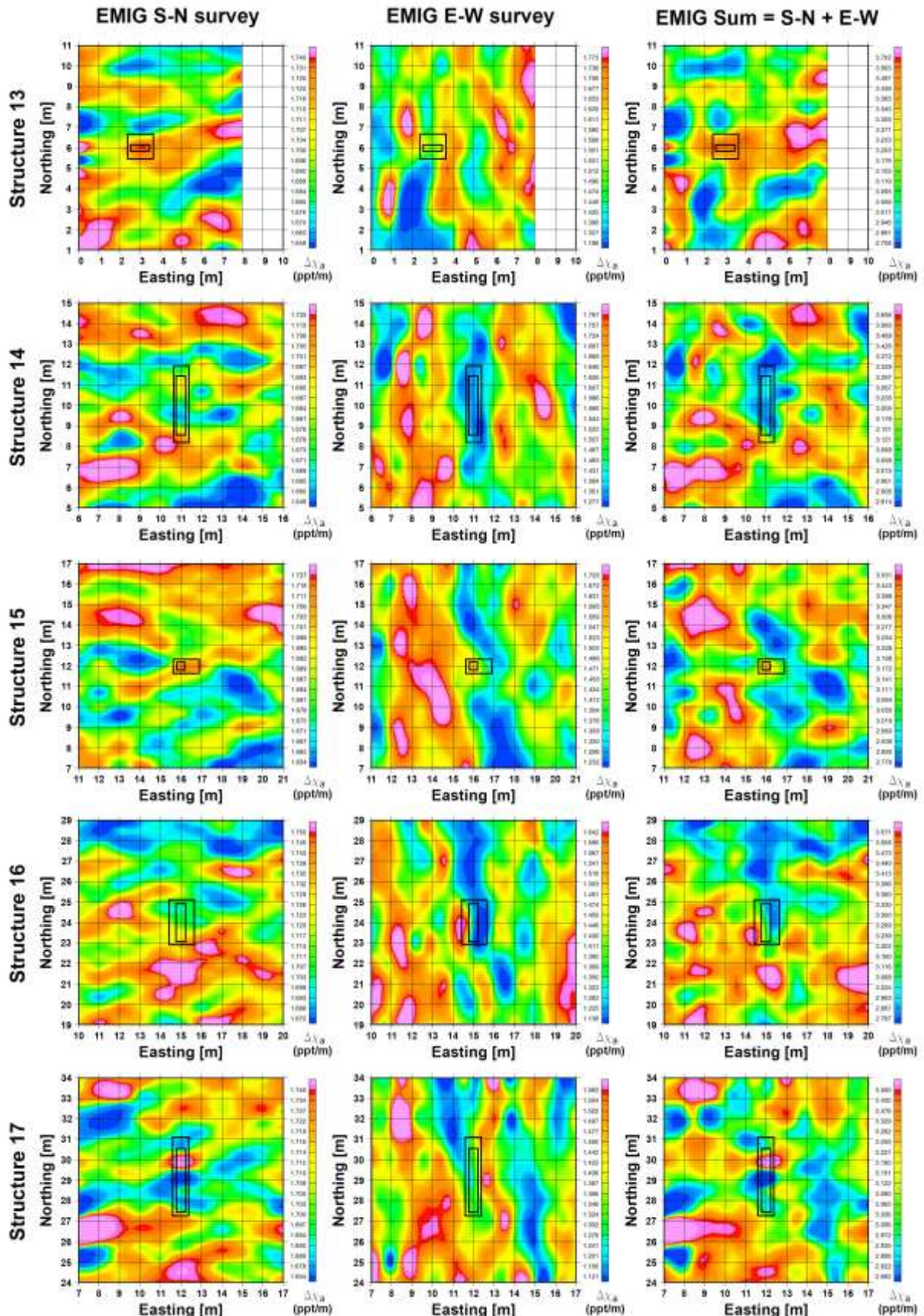


Figure S9. S-N (left), E-W (central) and Sum (right) Electromagnetic Induction Gradient (EMIG) in-phase close-up maps for structures 13-17. The plan views of the buried structures and the holes dug during construction are shown with black polygons. Color bars in each panel indicate the in-phase gradient value range.

3. Mediciones de velocidad de onda de corte y periodo fundamental del sitio en la parte occidental de la Cuenca de la Ciudad de México después del sismo de magnitud Mw 7.1 de 2017 en Puebla-Morelos, México

(Artículo publicado, citar como: Wood, C. M., Woodfield, L., Rahimi, S., Rosado-Fuentes, A., Sánchez-Sesma, F. J., Cruz-Jiménez, H., Mayoral, J. M. & de la Rosa, D. (2023). Shear Wave Velocity and Site Period Measurements for the Western Portion of the Mexico City Basin Following the Mw7.1 2017 Puebla-Morelos, Mexico, earthquake. *Earthquake Spectra*, 39(1), 505-527. <https://doi.org/10.1177/87552930221120834>)

El sismo Puebla-Morelos del 19 de septiembre de 2017 de magnitud 7.1 se originó en la Placa de Cocos a 57 km de profundidad y con un mecanismo de falla normal [SSN, 2017]. El sismo presentó un espectro amplio de períodos en donde la mayoría se encontraba entre los 0.15 y 1.00 s [Franke *et al.*, 2019]. A pesar de que el sismo se originó a aproximadamente 120 km de la CDMX, en la ciudad colapsaron 38 construcciones, 340 fueron clasificadas como de alto riesgo y 273 se clasificaron de seguridad incierta [GEER, 2017]. La mayoría se concentraron en la parte occidental de la Cuenca con alturas entre cinco y ocho pisos y un periodo fundamental entre 0.5 y 0.8 s [Franke *et al.*, 2019]. De acuerdo a las Normas Técnicas Complementarias por Diseño Sísmico (NTC-DS), la mayoría de las construcciones se ubican en la Zona de Transición (Zona II) y en la Zona de Lago (Zonas IIIa y IIIb) [GDF, 2004]. La primera está conformada por depósitos de suelo duro y roca erosionada mientras que la segunda están conformada principalmente por un depósito muy blando de arcilla lacustre no consolidada cuyo espesor aumenta desde el borde de la Cuenca hacia el centro y su velocidad de corte (V_s) es en general $< 100 \text{ m/s}$. La arcilla lacustre a menudo se encuentra sobre capas finas de limo arenoso muy denso o depósitos de arcilla rígida más gruesa [Mayoral *et al.*, 2016; Pestana *et al.*, 2002; Wood *et al.*, 2019]. Los períodos fundamentales del sitio (T_s) para las Zonas II, IIIa y IIIb son, respectivamente, $T_s < 1.0 \text{ s}$, $1.0 \text{ s} < T_s < 1.5 \text{ s}$ y $1.5 \text{ s} < T_s < 2.5 \text{ s}$ [GDF, 2004].

El riesgo sísmico de la CDMX está estrechamente correlacionada con el efecto de la doble resonancia, es decir, cuando la frecuencia fundamental de la construcción (T_b) coincide con la frecuencia fundamental del sitio (T_s) y la frecuencia dominante de las ondas sísmicas (T_{sw}) [Franke *et al.*, 2019; Mayoral *et al.*, 2019]. La mayoría de los daños causados por el sismo del 2017 se atribuyen al efecto de la doble resonancia y a la amplificación y duración del movimiento del suelo. Estos son efectos de sitio controlados principalmente por la capa de arcilla lacustre blanda y por las ondas sísmicas que quedan atrapadas en ella [Franke *et al.*, 2019; GEER, 2017; Mayoral *et al.*, 2019]. El origen de estos efectos se debe en parte a la variable y compleja formación y litoestratificación del subsuelo de la Cuenca del Valle de México, en

particular a la capa de arcilla lacustre blanda no consolidada y al panorama hidrológico de la Cuenca [Mayoral *et al.*, 2019; Pestana *et al.*, 2002; Seed *et al.*, 1988]. No obstante, es necesario mencionar que otros factores, como la condición, edad, diseño y calidad de las construcciones, también influyeron en los daños ocasionados.

Se ha demostrado que las propiedades de la arcilla lacustre cambian constantemente dentro de la Cuenca debido a la extracción excesiva de agua. Esto cambia el período fundamental del sitio a medida que se consolida la arcilla, dando como resultado un acortamiento en los períodos fundamentales del sitio [Arroyo *et al.*, 2013; Wood *et al.*, 2019]. La complejidad e incertidumbre en poder determinar las tasas de extracción y recarga de agua hacen difícil predecir el cambio del período fundamental. Las propiedades dinámicas de esta capa de arcilla se pueden investigar con diversos métodos. Dado que esta capa mantiene un comportamiento lineal a altos niveles de deformación [Mayoral *et al.*, 2016, 2008], es conveniente caracterizarla sísmicamente con técnicas no invasivas de ondas superficiales que presentan un perfil de V_s unidimensional (1D) a niveles bajos de deformación [Pandey *et al.*, 2016], que sean rápidas y cuyo costo-beneficio sea favorable [Lin y Chang, 2004; Xu y Wang, 2021].

Para reducir la vulnerabilidad sísmica es útil tener mayor conocimiento de la litoestratigrafía del subsuelo y los efectos de sitio locales en la CDMX, así como su variación dentro de la Cuenca. Esto conlleva a la necesidad de realizar más investigaciones en toda la Cuenca sobre las propiedades dinámicas de la capa de arcilla lacustre, sus variaciones a lo largo del tiempo y su impacto en el período fundamental. Por ello, para este estudio se muestrearon 25 sitios, principalmente en las Zonas de Transición y de Lago, en la parte occidental de la Cuenca con el fin de realizar una caracterización litoestratigráfica, identificar posibles discrepancias o cambios entre los períodos fundamentales de sitio y la zonificación sísmica, y estudiar la profundidad, espesor y rigidez de la capa de arcilla lacustre. La mayoría de los sitios se ubican en parques o áreas públicas, dos en la Zona I, siete en la Zona II, once en la Zona IIIa, cuatro en la Zona IIIb y uno en la Zona IIId. En cada sitio se utilizaron geófonos verticales y sismómetros de banda ancha para aplicar las técnicas sísmicas de análisis multicanal de ondas superficiales (MASW) lineal [Lin y Chang, 2004; Park *et al.*, 2005a, 1999], arreglo multicanal de microtremores (MAM) pasivo con arreglo en L y circular [Aki, 1957; Asten y Henstridge, 1984; Harjes y Henger, 1973; Park *et al.*, 2005b; Tokimatsu *et al.*, 1992] y cociente espectral H/V (HVSR) [Lermo y Chávez-García, 1993, 1994; Nakamura, 1989; Sánchez-Sesma *et al.*, 2011].

Se generaron curvas de dispersión de ondas Rayleigh con MASW y ambos arreglos de MAM y ondas Love con el arreglo circular de MAM; mientras que con HVSR se determina el período fundamental del sitio. En un proceso de inversión conjunta [Joh, 1966; Wathelet, 2008] ponderada entre las curvas de dispersión (80 %) y la frecuencia fundamental (20 %) se determina un modelo 1D de V_s del subsuelo que mejor ajuste los datos experimentales. Una vez determinados los parámetros de las capas del subsuelo más superficiales, por lo general una capa de alta V_s , éstos se fijan mientras que las interfases y V_s del resto de las capas se determinan con un proceso de inversión sin restricciones. La mediana de los modelos generados

es el modelo V_s final. Cabe mencionar que debido a que las técnicas de ondas superficiales no son únicas, las incertidumbres de la profundidad y V_s de las capas debajo de la arcilla lacustre son a menudo mayores que otras capas [Wood *et al.*, 2019].

3.1 Resumen del artículo

Se realizó una caracterización dinámica en 25 sitios ubicados en la parte occidental de la Cuenca de la Ciudad de México, la cual sufrió daños severos durante el sismo de magnitud Mw 7.1 de 2017 en Puebla-Morelos, México. Se utilizaron métodos activos y pasivos de ondas sísmicas superficiales y el método de cociente espectral H/V para generar perfiles 1D de (V_s) de los primeros 60 m de profundidad del subsuelo. Se compararon los periodos fundamentales medidos con los mapas de periodo sísmico desarrollados en 2004 y 2020 y con valores computados utilizando el programa Sistema de Acciones Sísmicas de Diseño (SASID) como lo establece la versión 2020 de las Normas Técnicas de Construcción por Diseño Sísmico (NTC-DS). La discrepancia más notable en la predicción del periodo fundamental, de acuerdo al mapa del 2004, se muestra en la frontera entre las Zonas II y IIIa, en donde los periodos fundamentales fueron sobreestimados. Estas estimaciones se mejoraron en el mapa del 2020 y muestran una estrecha similitud con los valores computados con SASID. También se determinó que la V_s , profundidad y espesor de la capa de arcilla lacustre son altamente variables dentro de la Cuenca. Los sitios más blandos se localizan entre los lechos de los lagos con V_s entre 45 y 57 m/s. Los sitios ubicados hacia el borde norte del lecho del lago tienen una mayor V_s , entre 80 y 100 m/s. El espesor de la capa de arcilla varía significativamente en el lado occidental de la Cuenca, oscilando entre aproximadamente 3 y 34 m. En general, los resultados de este estudio muestran una buena concordancia con el modelo incorporado en el programa SASID. Los resultados enfatizan la necesidad de monitorear periódicamente los cambios que ocurren en la capa de arcilla lacustre a lo largo del tiempo, complementan el desarrollo de modelos que mejoren nuestra comprensión de la propagación de ondas dentro de la Cuenca y confirman la necesidad de actualizar y mejorar las Normas de la Ciudad de México.

3.2 Resumen de los resultados del artículo

- Los periodos determinados con HVSR concuerdan con los intervalos de los períodos fundamentales de las NTC-DS 2004 [GDF, 2004] y Lermo *et al.* [2020], sin embargo si hay algunas diferencias notables.
- Se comparan el periodo fundamental determinado con HVSR con los valores de los mapas de zonificación sísmica de las NTC-DS del 2004 [GDF, 2004] y su actualización del 2020 [Lermo *et al.*, 2020] para identificar discrepancias entre ellos.
- Comparación de períodos fundamentales con las NTC-DS 2004 [GDF, 2004]:
 - 15 sitios (60 %) están dentro de los rangos establecidos, 8 sitios (32 %) tienen discrepancias y en 2 (8 %) no se pudo determinar.
 - La discrepancia más notable se muestra en la parte suroeste del área de estudio. Los períodos de los sitios 1 y 2 son 0.89 y 0.95 s, respectivamente, fuera del límite de 1.0 s.
 - Las diferencias más claras se observan en la Zona IIIa, donde varios sitios presentan períodos fundamentales por debajo de los valores mínimos establecidos.
 - En la Zona II, el valor del sitio 20 es ligeramente superior al periodo máximo para dicha zona.
- Comparación de períodos fundamentales con las NTC-DS 2020 [Lermo *et al.*, 2020]:
 - 18 sitios (72 %) están dentro de los rangos establecidos, 5 sitios (20 %) tienen discrepancias y en 2 (8 %) no se pudo determinar.
 - En la parte norte de la zona de estudio se encuentra el sitio 23, en el cual se determinó un periodo fundamental de 3.38 s. Para esta zona, el mapa de zonificación contempla un rango de 2.5 a 3.0 s.
 - La discrepancia mostrada alrededor de los sitios 1 y 2 comparada con la versión 2004 de las NTC-DS se corrige al desplazar el límite de 1.0 s hacia el este.
 - En general, este mapa de zonificación mejora las estimaciones del período fundamental, aunque presenta algunas discrepancias con los determinados en el estudio.
- Comparación de períodos fundamentales con SASID [GCM, 2017]:
 - Desde 2017 es necesario obtener el espectro de diseño sísmico y el periodo fundamental del SASID. Con este programa se obtienen los períodos fundamentales teóricos, mismos que se comparan con los obtenidos por HVSR.
 - Existe una estrecha similitud entre los períodos teóricos y los experimentales. Un ajuste lineal arroja una pendiente de 0.936 con un coeficiente de correlación de 0.929.

- Esta comparativa sugiere que los sitios 1, 2 y 5 están situados en la Zona II en lugar de la Zona IIIa, el sitio 20 está en la Zona IIIa en lugar de la Zona II y el sitio 23 está en la Zona IIIc en lugar de la Zona IIId.
- Los resultados obtenidos con las comparativas muestran la necesidad de continuar actualizando y mejorando la zonificación de la CDMX.
- De acuerdo a los perfiles 1D de V_s , los primeros 60 m de profundidad de la parte occidental de la Cuenca se pueden clasificar en cinco capas principales cuya profundidad y espesor varía a lo largo de la zona de estudio.
 - Corteza: de espesor < 3 m y con un rango de V_s entre 100 y 200 m/s.
 - Arcilla lacustre muy blanda: con un rango de V_s entre 45 y 100 m/s.
 - Suelo blando: con un rango de V_s entre 100 y 200 m/s.
 - Suelo rígido: con un rango de V_s entre 300 y 415 m/s.
 - Semiespacio: con un rango de V_s entre 420 y 580 m/s.
- No todas las capas están presentes en todos los sitios estudiados. En los sitios 16, 17, 22 y 24 la capa de arcilla lacustre no se observa en los perfiles de V_s . Esto se explica por la historia de esos sitios. Los sitios 16 y 17 están asociados a los flujos de lava del volcán Xitle y los sitios 22 y 24 a ladrilleras del siglo XIX. En particular el sitio 22 se ubica en el Parque Hundido, el cual se encuentra varios metros por debajo de las vialidades circundantes. Es posible que la capa de arcilla lacustre haya sido removida en estos sitios para la fabricación de ladrillos.
- La capa crítica es arcilla lacustre blanda no consolidada. En la mayoría de los sitios, a esta capa se le asocia una sola V_s . Sin embargo, hay sitios que tienen capas consecutivas de arcillas cuyas V_s van aumentando con la profundidad. Para estos casos se determinó un valor promedio de V_s para el conjunto de capas de arcilla.
- V_s de la capa de arcilla lacustre blanda no consolidada:
 - Los sitios en el límite noroeste de la Zona II (sitios 18, 19 y 20) tienen V_s entre 80 y 100 m/s.
 - El único sitio en la Zona II entre los lechos norte y sur del lago (sitio 13) tiene una V_s de aproximadamente 61 m/s. Mientras que un sitio cercano dentro de la Zona IIIa (sitio 12) tiene una V_s de aproximadamente 69 m/s. En la misma Zona IIIa pero cerca del límite con la Zona II, el sitio 5 tiene una V_s de aproximadamente 61 m/s.
 - El único sitio en la Zona II al sur del lecho del lago (sitio 15) tiene una V_s de aproximadamente 69 m/s. Un sitio cercano pero dentro de la Zona IIIa (sitio 2) tiene una V_s de aproximadamente 87 m/s.

- Entre los lechos norte y sur del lago, los sitios en las Zonas IIIa (Sitios 4, 6, 7 y 11), IIIb (sitios 21 y 25) y IIId (sitio 23) tienen una V_s de aproximadamente 57 m/s, entre 62 y 65 m/s y de aproximadamente 49 m/s, respectivamente.
- En el lecho sur del lago, los sitios en las Zonas IIIa (sitios 1, 3, 10 y 14) y IIIb (sitios 8 y 9) tienen una V_s entre 54 y 61 m/s y entre 45 y 49 m/s, respectivamente.
- Profundidad a la parte superior de la capa de arcilla lacustre blanda no consolidada:
 - La profundidad varía a lo largo de la parte occidental de la Cuenca, con valores que oscilan entre 0.5 y 6.6 m.
 - Los sitios ubicados en la frontera entre las Zonas II y IIIa tienen las profundidades más grandes, oscilando entre 1.2 y 6.6 m. Mientras que los que están en la Zona IIIa tienen las profundidades más bajas, oscilando entre 1.0 y 2.8 m.
 - De los sitios ubicados en la Zona IIIb, los del norte del lecho del lago tienen mayor profundidad que los del sur. Adicionalmente, la profundidad en los sitios de las Zonas IIIb y IIId al norte del lecho del lago es mayor que los sitios de la Zona IIIa.
- Espesor de la capa de arcilla lacustre blanda no consolidada:
 - El periodo también varía a lo largo de la parte occidental de la Cuenca.
 - Al norte del lecho del lago, en las Zonas IIIb (sitios 21 y 25) y IIId (sitio 23), se observa el espesor más grueso, con valores entre 20.5 y 34.1 m.
 - Los sitios en las Zonas II y IIIa tienen el menor espesor a lo largo de toda la Cuenca, con valores entre 2.8 y 10.5 m. A excepción de los sitios 10, 11 y 12 que se encuentran cerca de la frontera entre las Zonas IIIa y IIIb.
 - Al sur del lecho del lago, en las Zonas II y IIIb, el espesor está entre 4.2 y 14.7 m y entre 9.7 y 15.3 m, respectivamente.
- En general:
 - Los sitios al noroeste del lecho del lago tienen capas de arcilla relativamente rígidas, mientras que en sitios en el lecho sur del lago es muy blanda. Los sitios con las capas de arcilla más blandas se ubican hacia el centro del lago con V_s entre 45 y 50 m/s.
 - Las Zonas II y IIIb tiene la mayor y menor V_s , respectivamente.
 - La capa se sitúa a profundidades mayores en la Zona II que en las Zonas IIIa y IIIb, siendo esta última la Zona en la que se encuentra más somera.
 - El espesor de la capa es significativamente mayor en la Zona IIIb, en comparación con las Zonas II y IIIa.
 - La Zona II tiene el menor espesor aunque también presenta la mayor variabilidad.
 - Estos resultados sugieren que el límite entre las Zonas II y IIIa en los mapas de zonificación deben estar en constante actualización para representar adecuadamente las condiciones del subsuelo.

3.3 Artículo publicado



Research Paper



Shear wave velocity and site period measurements for the western portion of the Mexico City Basin following the Mw7.1 2017 Puebla–Morelos, Mexico, earthquake

Earthquake Spectra
I–23
© The Author(s) 2022
Article reuse guidelines:
sagepub.com/journals-permissions
DOI: 10.1177/87552930211120834
journals.sagepub.com/home/eqs



**Clinton M Wood, M.EERI¹, Landon J Woodfield¹,
Salman Rahimi², Alejandro Rosado-Fuentes³,
Francisco J Sánchez-Sesma, M.EERI⁴,
Hugo Cruz-Jiménez⁴, Juan M Mayoral⁵,
and Daniel de la Rosa⁵**

Abstract

Dynamic site characterization was performed at 25 sites located on the western portion of the Mexico City Basin that were severely damaged during the Mw7.1 2017 Puebla–Morelos, Mexico, earthquake. Testing was conducted using active and passive seismic surface wave methods and the microtremor horizontal-to-vertical spectral ratio method to determine site periods and develop one-dimensional (1D) shear wave velocity (V_s) profiles for the first 60 m of the subsoil. The measured site periods were compared to site period maps developed in 2004 and 2020 along with values computed using the Design Seismic Actions System (SASID) software following the 2020 version of the Complementary Technical Norms for Seismic Design (NTC-DS). The most noticeable biases in the predictions from the 2004 site period map were observed between the boundary of Zone II and Zone IIIa, at which site periods are overestimated. These estimates were improved upon in the 2020 site period map and showed a close similarity with SASID computed site period values. The V_s , depth, and thickness of the lacustrine clay layer were also determined to be quite variable within the basin. The softest sites are located between the lakebeds with a V_s between 45 and 57 m/s. Sites located toward the outer rim of the North lakebed have a higher V_s between 80 and 100 m/s. The thickness of the clay layer varies

¹University of Arkansas, Fayetteville, AR, USA

²Arup, Los Angeles, CA, USA

³Unidad de Posgrado UNAM, Mexico City, Mexico

⁴Instituto de Ingeniería UNAM, Mexico City, Mexico

⁵National Autonomous University of Mexico, Mexico City, Mexico

Corresponding author:

Clinton M Wood, University of Arkansas, 4190 Bell Engineering Center, Fayetteville, AR 72701, USA.
Email: cmwood@uark.edu

significantly in the western side of the Basin with values ranging between approximately 3 and 34 m. Overall, the results of this study indicate good agreement with the model embedded in the SASID software. The results (1) emphasize the need to regularly monitor changes that occur over time in the lacustrine clay layer, (2) complement the development of models that improve our understanding of wave propagation within the Basin, and (3) update and improve Mexico City's Norms.

Keywords

Mexico City, seismic zonation, dynamic site characterization, site period, Puebla–Morelos earthquake, seismic surface wave methods

Date received: 9 March 2022; accepted: 3 August 2022

Introduction

Mexico is one of the most seismically active regions in the world, located at the intersection of five major tectonic plates. The 19 September 2017 moment magnitude 7.1 (Mw7.1) Puebla–Morelos, Mexico, earthquake is the most recent of many devastating earthquakes to occur in the region over the last 50 years. It caused significant loss of life, damage to buildings, lifelines, and infrastructure, as well as being costly to the Mexican economy. This earthquake affected more than 28 million people, 54,000 schools, and 5,700 hospitals (GEER, 2017). This earthquake caused a complete collapse in 38 buildings, 340 buildings to be classified as high-risk buildings, and 273 buildings to be identified as security uncertain (GEER, 2017).

The 2017 Puebla–Morelos, Mexico, earthquake, which occurred on a normal fault, was located approximately 60 km southwest of Puebla and 120 km southeast of Mexico City. The source was located at a depth of approximately 57 km near the point of maximum curvature of the Cocos Plate, which is being subducted beneath the North America Plate (GEER, 2017). Although the epicenter of the earthquake was located 120 km from Mexico City, the western portion of the Mexico City Basin, where the transition zone is located, was significantly affected by this earthquake (Singh et al., 2018). For most earthquakes, the Basin response is generally insensitive to differences in magnitudes, azimuths, and focal depths (Reinoso et al., 1990). This conspicuous behavior is behind the empirical approach adopted for design, which is based on observed ground motions (Rosenblueth et al., 1989) recorded by the Mexico City Accelerometric Network. This approach has been so far successful to establish seismic loads for the current Mexico City seismic code. This type of normal faulting event was considered in the development of the seismic code. Yet, many buildings were damaged or collapsed as ground motions were amplified by the lakebeds and basin structure. This is due to, among other factors, the complex and variable subsurface layering (particularly, the very soft unconsolidated lacustrine clay layer) and hydrological settings of this area (Mayoral et al., 2019; Pestana et al., 2002; Seed et al., 1988). Observations of the damaged buildings have revealed that these structures have resonant frequencies correlating well with the resonant frequency of the site and the predominant frequency of the ground motions (Franke et al., 2019), a phenomenon referred to as double resonance. This indicates that the seismic risk in Mexico City is strongly correlated with the site effects in the area. Therefore, an accurate understanding of the subsurface layering and the local site effects of the Mexico City Basin and its variation within this area will be helpful for reducing the seismic vulnerability in the Basin during future extreme earthquake events.

To understand the geology of the Mexico City Basin as it pertains to the seismic response of the region, the past volcanic activity needs to be considered. The Mexico City Basin started to form 10–13 million years ago from volcanic activity with the Chichinautzin Range, closing off the Basin to the South 130,000 years ago (Jaimes-Viera et al., 2018). At that time, the Basin consisted of alluvial fans and debris flows interbedded with volcanic pumice and ash, known as the Tarango Formation (O’Riordan et al., 2017). The other important factor that has significantly affected the geology of the Mexico City Basin is the formation and disappearance of the lacustrine system within the Basin, composed of six lakes, following the volcanic activity. The former Texcoco Lake and the Xochimilco and Chalco Lakes formed the Mexico City Basin. These three large lakes disappeared over the last 500 years after the Spanish colonization, mainly due to drainage, groundwater extraction, and land reclamation for urban development. Therefore, while the surrounding areas of the Mexico City Basin, known as the transition zone, are comprised of hard soil deposits and weathered rock, the central areas consist mainly of a very soft unconsolidated lacustrine clay deposit formed by sediments carried from the surrounding mountains, which settled extremely slowly in the lakes. These lacustrine clay deposits increase in thickness from the edge of the basin to the center and are often underlined by a thin layer of very dense sandy silt or thicker stiff clay deposits. Harder deposits are observed below the stiff clay (please see Santoyo et al. (2005) for a more detail description of the basin layering).

The lacustrine clay layer in the Mexico City Basin has a shear wave velocity (V_s) generally less than 100 m/s and a variable thickness throughout the Basin (Mayoral et al., 2016; Pestana et al., 2002; Wood et al., 2019). The engineering properties of the lacustrine clay have been extensively investigated in the past (e.g. Díaz-Rodríguez, 2003; Mayoral et al., 2016, 2008; Romo, 1995). As an example, most of the severe damage to buildings and infrastructure during past earthquakes has been attributed to amplification and duration elongation of the seismic waves trapped in this extremely soft clay layer (Mayoral et al., 2019). The response of the high plasticity lacustrine clay is nearly elastic up to shear strain as high as 0.3% (Mayoral et al., 2016; Romo et al., 1988; Seed et al., 1988). This contributes to significant amplification of seismic waves, as observed during the 1985 Michoacán earthquake (Seed et al., 1988). The dynamic properties of the lacustrine clay layer can be investigated using a variety of methods. However, given that the behavior of the clay layer remains linear up to high strain levels, non-invasive seismic surface wave measurements that develop a one-dimensional (1D) V_s profile at low strain levels are ideal candidates for rapid and cost-effective dynamic site characterization of the Basin. Nevertheless, a limited number of researchers have conducted such studies across the Basin (Mayoral et al., 2008, 2016; Wood et al., 2019). In addition, the properties of the lacustrine clay have been shown to be constantly changing within the Basin. This is due to excessive groundwater extraction in the region, which shifts the site period within the Basin as the lacustrine clay consolidates (Arroyo et al., 2013; Wood et al., 2019). This results in the site periods getting shorter with time. The rate of period change is a function of the water extraction and water recharge rate; hence, it is very difficult to predict the site period change over time. In this regard, many studies have utilized the microtremor horizontal-to-vertical spectral ratio (MHVSR) method for site period characterization across the Basin (e.g. Arroyo et al., 2013; Gurler et al., 2000; Lermo and Chávez-García, 1994; Wood et al., 2019). Some of these studies were used to develop the Mexico City’s Complementary Technical Norms for Seismic Design (Normas Técnicas Complementarias para Diseño Por Sismo, NTC-DS) (GDF, 2004) site period map, which can be used for predicting site period geospatially across the Basin. The MHVSR method is a single station method, which typically uses a three-component seismometer to measure background microtremors. The microtremor is

processed in the frequency domain where the squared average of the two horizontal Fourier amplitude spectra (FAS) is divided by the vertical Fourier amplitude spectrum. If a sufficient impedance contrast exists in the subsurface, a peak will form in the frequency-spectral ratio domain. The frequency of this peak has been shown to correspond well with the fundamental site frequency (or period) of a site (Lermo and Chávez-García, 1994).

All these facts highlight the need for more investigations into the dynamic properties of the lacustrine clay layer and its variations over time, and its impacts on the site period across the Basin. Therefore, in this study, dynamic site characterization measurements were performed at 25 sites affected during the 2017 Puebla–Morelos, Mexico, earthquake. The goals of this article are (1) to determine the potential discrepancies or changes in the site periods and seismic zonation within the western portion of the Basin and (2) to closely examine the depth, thickness, and stiffness of the lacustrine clay layer as the main layer governing the site effects in the Basin. The observed building damage following the 2017 Puebla–Morelos, Mexico, earthquake are first briefly discussed. The site locations, seismic surface wave measurements, and data processing are then provided. This is followed by a comparison of the measured site periods with the 2004 and 2020 Mexico City Basin site period contour maps and comparison with the Sistema de Acciones Sísmicas de Diseño (SASID, 2020) software site period values. The variations of the shear wave velocity (V_s) profiles within the Basin are then detailed with a focus on the lacustrine clay layer. Finally, discussion regarding the variation of site period and the properties of the lacustrine clay layer, and its impacts on the site period are provided.

Observed building damage following the 2017 Puebla–Morelos, Mexico, earthquake

Figure 1 presents the damaged building distribution observed by the Civil Engineering Bridge Inspections organized by the Colegio de Ingenieros Civiles de México, A.C. (CICM) following the 2017 Puebla–Morelos, Mexico, earthquake. This damage was classified into three groups: collapse (red bullets), major damage (yellow triangles), and low to moderate damage (blue squares), as labeled in Figure 1 (Franke et al., 2019; GEER, 2017). The mapped building damage is overlaid on the Mexico City map and the 2004 version of the seismic zonation contour map (GDF, 2004) in Figure 1a and b, respectively. This site period contour map is also used in the other sections of this article for comparison purposes since the Basin is divided into three major seismic zones, additionally, Zone III is subdivided into four sections. It has been shown that the 2004 site period map provided the most accurate site period predictions within the Basin following the 2017 event (Wood et al., 2019).

One of the most interesting observations from the 2017 Puebla–Morelos, Mexico, earthquake is that the majority of the severely damaged buildings were concentrated on the western portion of the Basin, in the Transition Zone (Zone II) and Lake Zones (IIIa and IIIb), as observed in Figure 1b. Based on the NTC-DS site period map, these zones have site periods (T_s) of $T_s < 1$ s for Zone II, $1 \text{ s} < T_s < 1.5 \text{ s}$ for Zone IIIa, and $1.5 \text{ s} < T_s < 2.5 \text{ s}$ for Zone IIIb (GDF, 2004). Moreover, according to field observations, the majority of the collapsed or damaged buildings were observed to be between five and eight stories tall (Franke et al., 2019), with an approximate elastic fundamental period (T_b) ranging between 0.5 and 0.8 s. In addition, for the 2017 Puebla–Morelos, Mexico, earthquake, the seismic wave periods (T_{sw}) occurred over a wide spectrum, with the majority being approximately between 0.15 and 1.0 s (Franke et al., 2019). Therefore, based on the fundamental periods of the site (T_s), fundamental periods of the damaged buildings

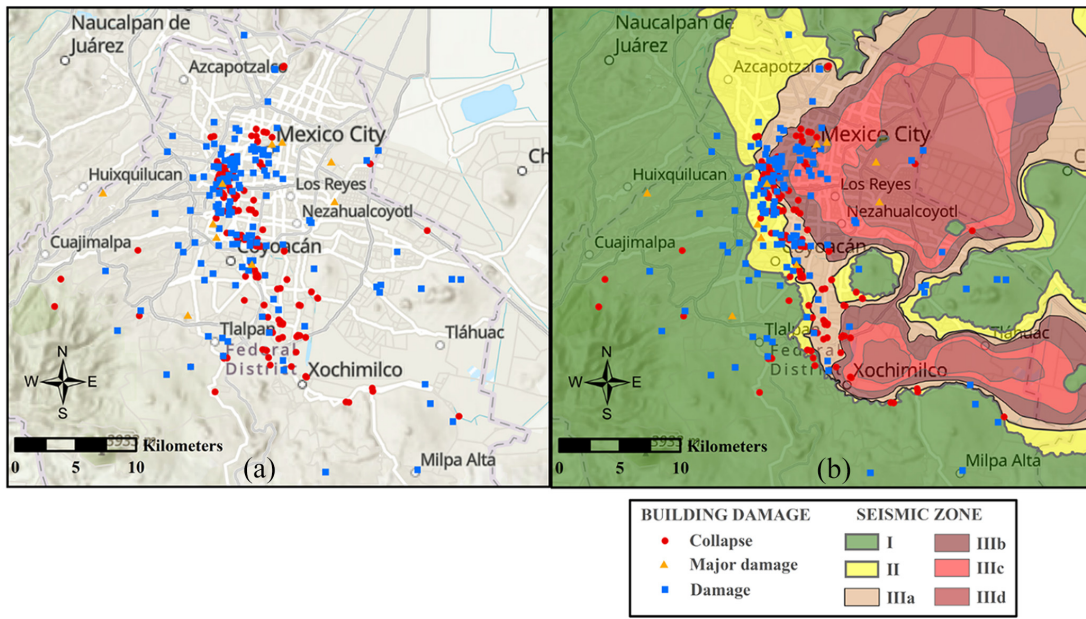


Figure 1. Observed building damage, following the 2017 Puebla–Morelos earthquake, overlaid with the (a) Mexico City map and (b) with the 2004 seismic zonation map (GDF, 2004).

(T_b), and the fundamental periods of the earthquake event (T_{sw}), most of the damage in the buildings was caused by double resonance. This means that most of the damage to the buildings was related to site effects, mainly caused by the very soft lacustrine clay deposit. It is worth highlighting that other factors such as the condition and age of the damaged buildings, and the design and construction quality of the buildings also played a role in the building damage during the 2017 Puebla–Morelos, Mexico, earthquake. More information regarding the observed building damage is provided in the GEER (2017) and Franke et al. (2019).

Site locations and seismic surface wave measurements

Dynamic site characterization was performed at 25 sites along the western edge of the Mexico City Basin, mainly in the Transition Zone (Zone II) and Lake Zones (IIIa and IIIb). The locations of the tested areas across the western portion of the Mexico City Basin along with the 2004 seismic zonation contour map are depicted in Figure 2a and b. In addition, the site name, coordinate, and testing configuration are tabulated in Table 1. The sites were selected based on the mapped building damage following the 2017 Puebla–Morelos earthquake, which were mainly concentrated on the western portion of the Basin, as discussed in detail in the previous section. From the 25 sites tested, two are located in Zone I, seven are located in Zone II, 11 are located in Zone IIIa, four are located in Zone IIIb, and one is located in Zone IIId. The majority of the sites were located in public parks or other public areas around the city. Four different seismic site characterization methods were conducted at each site. These include active Multi-channel Analysis of Surface Waves (MASWs), passive Microtremor Array Measurements (MAMs) using an L-array, passive MAM using a large circular array, and MHVSR. Testing configurations for each site are presented in Table 1. As an example, the seismic surface wave testing configuration for Site 14 is presented in Figure 3.

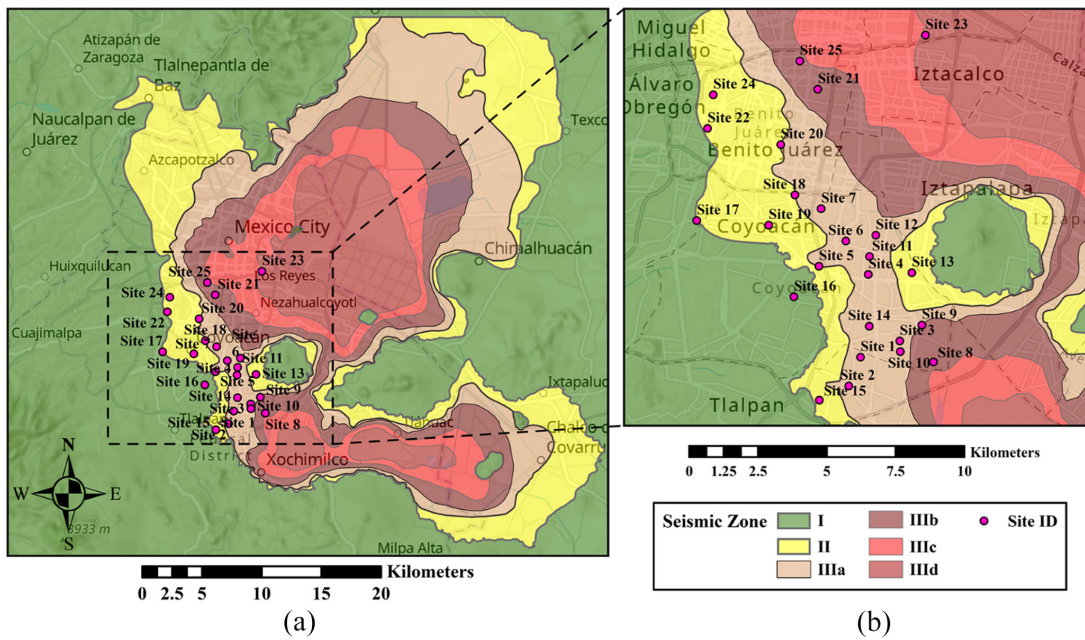


Figure 2. Site locations for seismic surface wave measurements across the western portion of the Basin along with the seismic zonation from the 2004 NTC-DS (GDF, 2004) (a) Complete basin and (b) western edge.

The active MASW testing was performed using Rayleigh-type surface waves using a linear array of 24 vertical geophones spaced 2 m apart (see the blue line in Figure 3). Testing was conducted with source offsets of 5, 10, 20, and 30 m. At each source offset, five vertical strikes from a 5-kg sledgehammer were stacked to increase the signal-to-noise ratio of the data. The passive MAM measurements using an L-shaped array were made at each site using 24 vertical geophones with a 5-m spacing between geophones. The L-arrays consist of two legs at a 90-degree turn, if possible, with one geophone set at the turn peak (see the green L-shape in Figure 3). The length of each leg was kept approximately equal for all sites. However, at some sites, this was not possible due to site constraints. Background noise (microtremors) was recorded for at least 30 min at each site, providing 30 and 60 s records for data processing. The passive MAM measurements using a circular array with a diameter ranging between 50 and 200 m were performed at each site using six, three-component broadband seismometers. Five of the seismometers were arranged evenly around the perimeter of the circle, with the remaining one located at the center of the circle (see the red dots and circle in Figure 3). For each site, the circular array was left to record microtremors simultaneously for at least 1 h. MAM circular array data collected using the seismometers were also used to estimate the site period using the MHVSR technique at each site. Geophysical testing configuration along with the ground view of the field testing of each site is provided in Wood et al. (2020).

Data processing

The first step for the data processing of the MASW data is to transform the raw time-space ($t-x$) domain data into the frequency-wavenumber ($f-k$) domain. Different transformation techniques can be used in this regard (Rahimi et al., 2021). In this study, the frequency domain beam former (FDBF) transformation technique (Zywicki, 1999) was

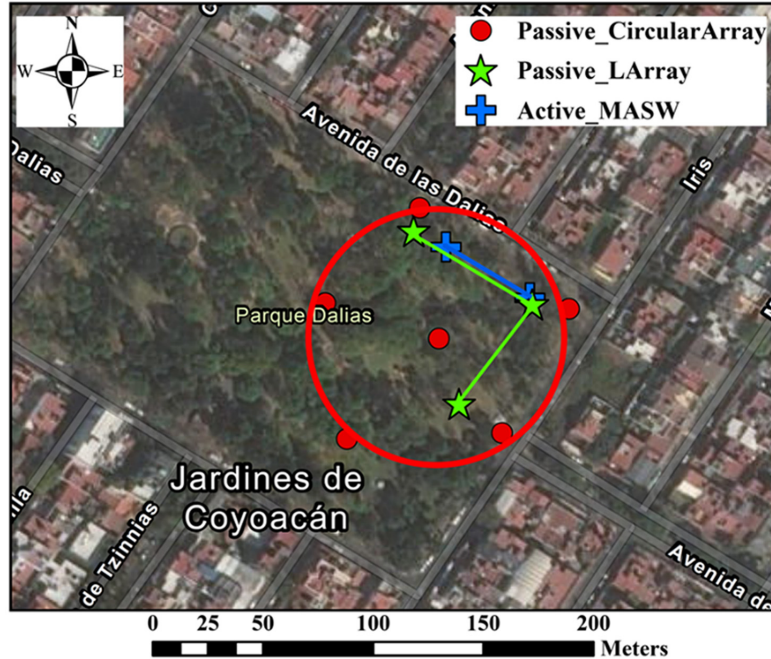


Figure 3. Example of the seismic surface wave testing configurations for Site 14.

utilized along with the multiple source offset method to be able to identify near-field contamination and quantify dispersion uncertainty (Rahimi et al., 2021; Wood and Cox, 2012). At each frequency, the experimental dispersion data were determined by identifying the peak in the f - k spectra. Dispersion data from different source offsets were combined to form a composite dispersion curve. Data corrupted by near-field effects or related to effective or higher modes were then eliminated to identify the fundamental mode of propagation. The mean phase velocity and standard deviation were calculated at each frequency to form a mean dispersion curve with uncertainty. As an example, the final dispersion data generated from the active MASW method using Rayleigh waves (labeled as Active R) for Site 14 are shown with blue in Figure 4a.

The MAM L-array data were processed using the conventional frequency-wavenumber (f - k) method (Harjes and Henger, 1973; Kelly, 1967) to produce Rayleigh wave dispersion curves using the Geopsy software suite (www.geopsy.org). In Geopsy, 60-s time windows were used, and within each time window, 125 frequency bands were processed based on a log distribution between 1 and 30 Hz. Dispersion data from all time windows were then combined to form a composite dispersion curve. The mean phase velocity and standard deviation were calculated for 125 frequency bins to create the final dispersion curve (Himel and Wood, 2021). An example of the dispersion data generated using the MAM L-array method for Site 14 is shown in Figure 4a as magenta dots and labeled as L-array.

The MAM circular array data were processed using two methods: the high-resolution frequency-wavenumber (HRFK) method (Capon, 1969) and the modified spatial autocorrelation (MSPAC) method (Bettig et al., 2001). The HRFK was used for both Rayleigh (HRFK R) and Love (HRFK L) wave data, but the MSPAC was only used to produce Rayleigh wave dispersion data. In the HRFK method, time windows of 180 s were used for data processing. In each time window, peak wavenumber x and y pairs were selected

Table I. Location and experimental configuration for the study sites

Site number	Site name	Latitude	Longitude	Zone ¹	MASW array length	MAM L-array lengths and angle	MAM circular array diameter
1	Floresta Coyoacán	19.303931	-99.129369	IIIa	46 m	60 × 55 m at 90°	68 m
2	La Fuente Park	19.294529	-99.133217	IIIa	46 m	60 × 55 m at 55°	70 m
3	Campestre Coyoacán Park	19.309202	-99.116568	IIIa	46 m	60 × 55 m at 90°	115 m
4	Ejido Culhuacan Park	19.330913	-99.126851	IIIa	46 m	80 × 35 m at 90°	58 m
5	Xotepingo Park	19.333584	-99.142989	IIIa	46 m	60 × 55 m at 90°	74 m
6	Park on Cerro Cubilete street	19.341828	-99.134183	IIIa	46 m	80 × 35 m at 90°	52 m
7	Masayoshi Ohira Park	19.352357	-99.142272	IIIa	46 m	65 × 50 m at 90°	94 m
8	Park on Hacienda Torrecillas Street	19.302363	-99.105545	IIIB	46 m	60 × 55 m at 90°	74 m
9	El Triangulo Park	19.314396	-99.109342	IIIB	46 m	75 × 40 m at 90°	56 m
10	Fraccionamiento Los Sauces	19.305735	-99.116391	IIIa	46 m	60 × 55 m at 90°	90 m
11	Park on Ejido de los Reyes Street	19.336769	-99.126444	IIIa	46 m	75 × 40 m at 90°	50 m
12	Naciones Unidas Park	19.343699	-99.124395	IIIa	46 m	60 × 55 m at 90°	145 m
13	Sports Field at ESIME Culhuacán	19.331476	-99.112617	II	46 m	60 × 55 m at 90°	82 m
14	Italia/Dalias Park	19.314019	-99.126533	IIIa	46 m	60 × 55 m at 90°	112 m
15	Hacienda de San Juan Park	19.289901	-99.142843	II	46 m	60 × 55 m at 90°	90 m
16	Ecológico Huayamilpas Park	19.323619	-99.151115	—	46 m	60 × 55 m at 90°	90 m
17	Parque Tagle	19.348499	-99.182919	—	46 m	60 × 55 m at 90°	104 m
18	Parque Xicoténcatl	19.356837	-99.150813	—	46 m	60 × 55 m at 90°	100 m
19	Plaza de La Conchita	19.346991	-99.159394	II	46 m	60 × 55 m at 81°	64 m
20	Venados Park	19.373266	-99.155449	II	46 m	65 × 50 m at 90°	50 and 200 m
21	José Refugio Ménez Park	19.391333	-99.143364	IIIB	46 m	60 × 55 m at 90°	70 m
22	Hundido Park	19.378554	-99.179385	II	46 m	60 × 55 m at 90°	104 m
23	Ciudad Deportiva "Magdalena Mixhuca" Puerta 2	19.408969	-99.108158	IIID	46 m	65 × 50 m at 90°	110 m
24	Alfonso Esparrza Oteo Park	19.38952	-99.17751	II	46 m	75 × 40 m at 82°	110 m
25	Plaza Las Americas	19.400533	-99.149236	IIIB	46 m	60 × 55 m at 81°	80 m

¹Zone is based on the 2004 NTC-DS map.

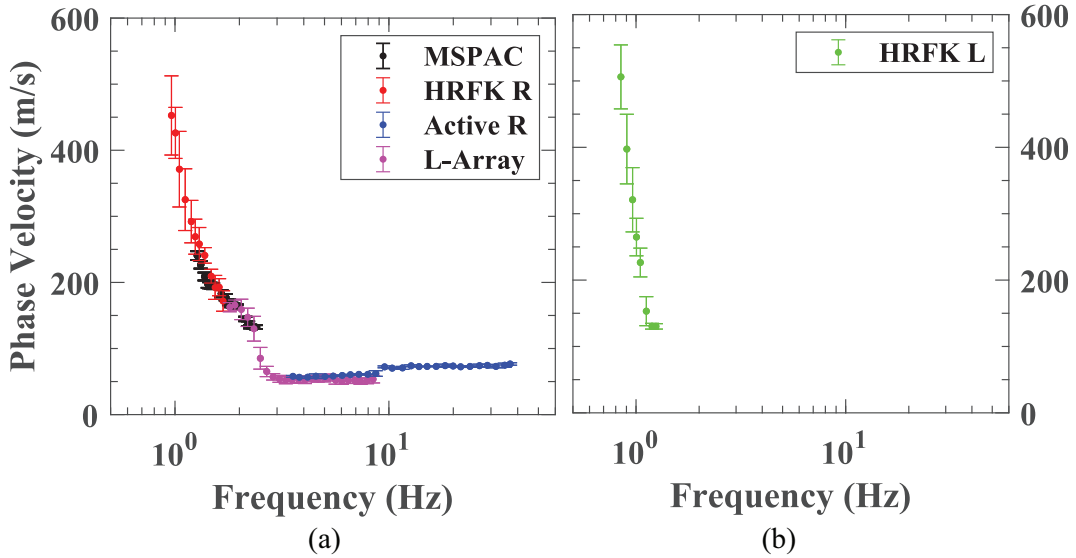


Figure 4. Example of Rayleigh (a) and Love (b) dispersion curves generated for Site 14 using the combination of active and passive methods.

at 125 frequency samples on a log scale between 0.1 and 20 Hz. The raw dispersion curve was then processed to remove outliers and dispersion points beyond the array resolution limits (Wathelet, 2008). The mean phase velocity (Rayleigh and Love) and the standard deviation were then calculated at each bin. In the MSPAC method, receiver pairs were divided into three sets of circular sub-arrays. The recordings were split into 180-s time windows. In each time window, autocorrelation values were calculated for the 125 frequency bins on a log scale from 0.1 to 20 Hz. Dispersion data generated using the HRFK and MSPAC methods for Site 14 using Rayleigh waves are presented in Figure 4a with red and black colors, respectively. In addition, Figure 4b shows an example of Love dispersion data generated using the HRFK for Site 14. The experimental dispersion data generated for the rest of the test sites are provided in Wood et al. (2020).

The raw MHVSR data were processed in general accordance with SESAME European Research Project (2004) guidelines. The raw data were divided into 3 min non-overlapping time windows to allow for uncertainty in the MHVSR results to be estimated. The FAS of each component was estimated for each time window and smoothed using a Konno and Ohmachi (1998) smoothing filter. The squared average of the two horizontal components FAS was divided by the vertical FAS to calculate the amplitude of the MHVSR ratio. The mean frequency peak of the MHVSR and its standard deviation were then computed from all individual time windows. The frequency associated with the peak MHVSR was then determined to be used for the joint inversion process.

The final experimental Rayleigh and Love wave dispersion curves were used along with the MHVSR peak frequency (i.e. site period) in a joint inversion process using the combination of the Geopsy software package (Wathelet, 2008) and WinSASW (Joh, 1996). WinSASW was only used for the inversion of a portion of the dispersion curve that includes a velocity reversal layer (lacustrine clay layer for these sites) below the crustal layers (i.e. a high-velocity layer followed by a low-velocity layer). The Geopsy software was not used for the inversion of this portion of the dispersion curve due to its inability to properly model this condition. Once the near-surface layers were identified using

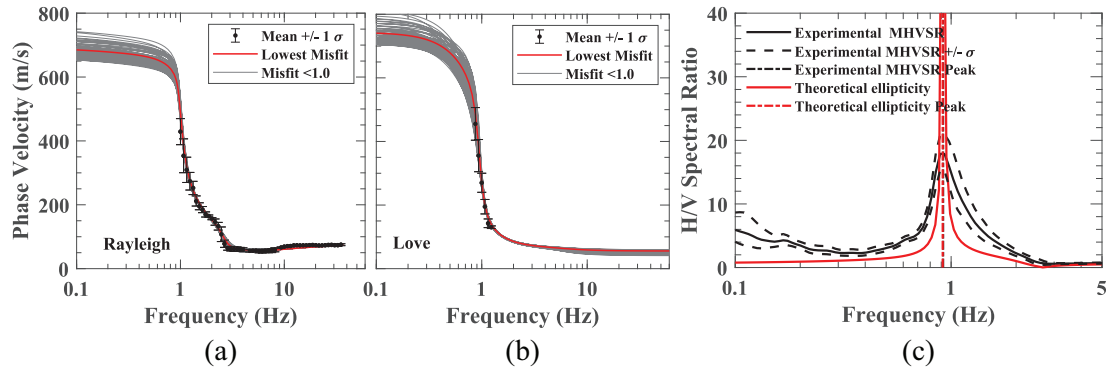


Figure 5. An example of joint inversion results using Rayleigh and Love phase velocity dispersion data and MHVSR peak frequency for Site 14. Rayleigh (a) and Love (b) dispersion target fit with the best 1000 representative dispersion curves with misfit <1.0, and (c) experimental MHVSR curve with theoretical ellipticity curve.

WinSASW (typically only a single higher velocity layer), these layers were locked into the Dinvver parametrization plugin of the Geopsy software, and the parameters for the rest of the layers were set for the inversion process. In the parameters, layer interfaces and shear wave velocity were loosely constrained to allow Dinvver to search for the best V_s profile based on the experimental data. Initial layering was developed based on major changes in the dispersion curve and adjusted as necessary to fit the dispersion data. Parameters were varied to ensure the inversion was not stuck in a local minimum. Weighting factors of 0.8 and 0.2 were used for the dispersion data and MHVSR peak frequency, respectively. A minimum of half a million iterations with different parameterizations was performed for each site to retrieve the 1D V_s profiles. The quality of the fit between the experimental and theoretical data was assessed by the misfit parameter (i.e. collective squared error between the experimental and theoretical data) and visual inspection (Griffiths et al., 2016; Rahimi et al., 2018; Wood and Baker, 2018). The median of the 1000 best V_s profiles was then used as the final V_s profile. For example, the experimental dispersion curve and the theoretical dispersion fit for the models with a misfit value less than 1.0 for Rayleigh and Love waves for Site 14 are provided in Figure 5a and b, respectively. In addition, the fit between the experimental MHVSR peak frequency and the theoretical ellipticity curve is shown in Figure 5c. The experimental dispersion curves and theoretical dispersion fits, along with the fit between the experimental MHVSR peak frequency and the theoretical ellipticity curve for the rest of the tested sites, are provided in Wood et al. (2020).

Figure 6 presents the final V_s profile for Site 14, along with the associated standard deviation ($\sigma \ln(V_s)$), as an example. In this figure, the best V_s profiles with a misfit value less than 1 (gray solid line), the lowest misfit V_s profile (black dotted line), the counted 5% and 95% V_s profiles (dashed blue lines), and the median V_s profile (red solid line) are included. In addition, the location of the lacustrine clay layer is highlighted in this profile. Due to the non-uniqueness of surface wave methods, the uncertainty of the V_s and depth of the layers below the lacustrine clay are often greater than other layers as observed in Figure 6. This should be considered when using these V_s profiles for future studies. The data processing for all 25 sites tested in this study is discussed in detail in Woodfield (2020). For each site, the final 1D V_s profile is provided in Wood et al. (2020).

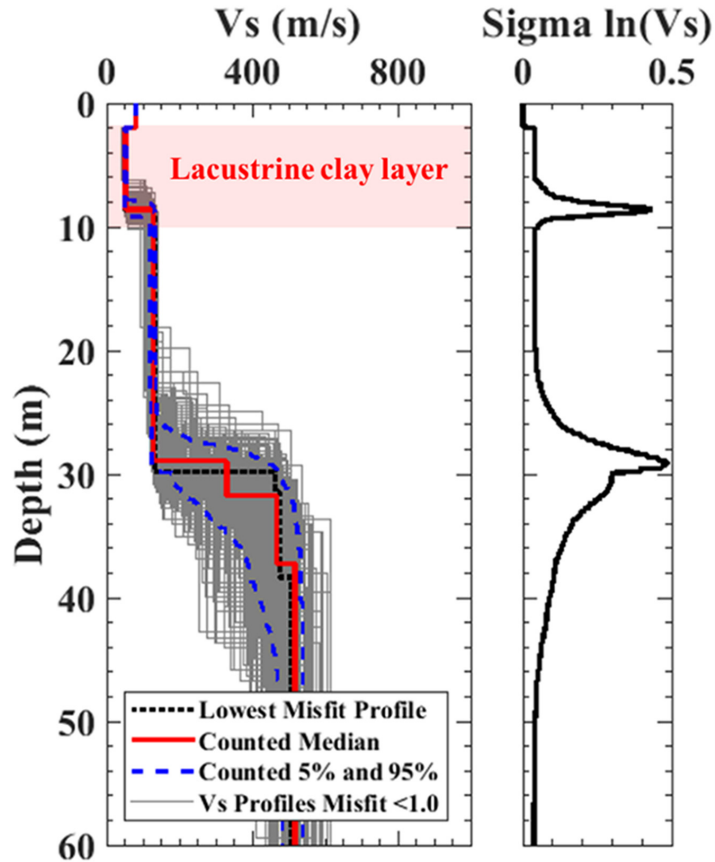


Figure 6. Example of the best representative V_s profiles with misfit less than 1.0 along with its counted median and $\sigma \ln(V_s)$ for Site 14.

In addition, the median/final and minimum misfit V_s profiles are tabulated in Wood et al. (2020) for each site.

MHVSR site period measurements

To identify the potential bias in the estimated site periods from the 2004 NTC-DS (GDF, 2004) contour map (Figure 7a) and updated 2020 Lermo et al. (2020) contour map (Figure 7b), the measured MHVSR site periods are compared to the two contour maps in Figure 7. In this figure, the measured site period from the MHVSR method for the 25 sites tested in this study is shown overlain on Figure 7a and b. For Figure 7a, the measured site periods from the MHVSR agree well with the site period ranges from the 2004 NTC-DS (GDF, 2004) and 2020 Lermo et al. maps. However, a few noticeable differences exist between the measured MHVSR site periods and the intervals from the two contour maps.

Out of the 25 measured sites, site periods from 15 sites (60%) are within the correct 2004 NTC-DS contours (GDF, 2004), 8 sites (32%) show discrepancies, and 2 sites (8%) did not have discernible HVSR site periods. For the Lermo et al. (2020) map, 18 sites (72%) are within the correct contour, 5 sites (20%) show discrepancies, and 2 sites (8%) did not have a discernible HVSR site period. The first noticeable difference for both maps is observed in the northern lake, at which the site periods are between 3.5 and 4.0 s based

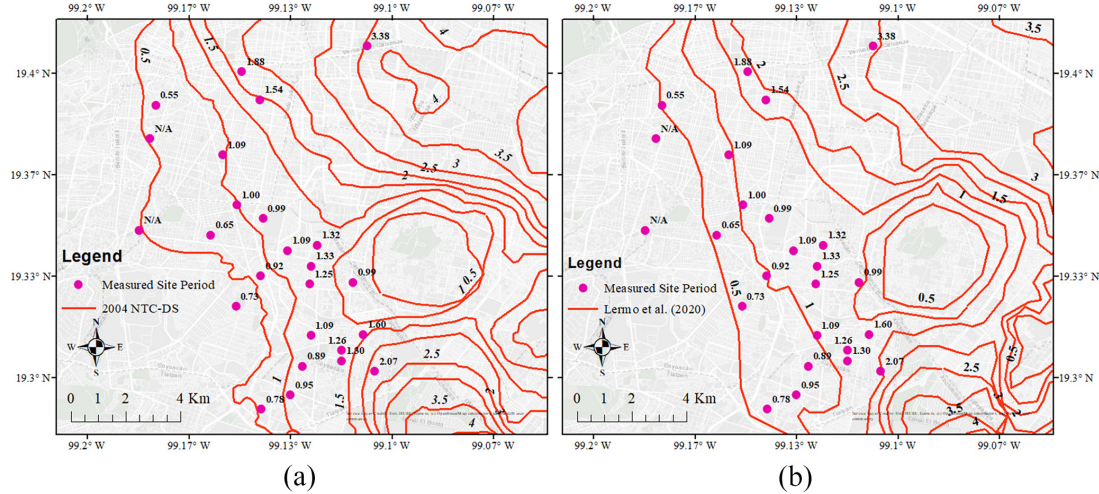


Figure 7. Comparison of the measured site period (in seconds; magenta dots) using MHVSR overlain on (a) the site period contour map from the 2004 NTC-DS (GDF, 2004) and (b) the 2020 Lermo et al. (2020) site period contour map.

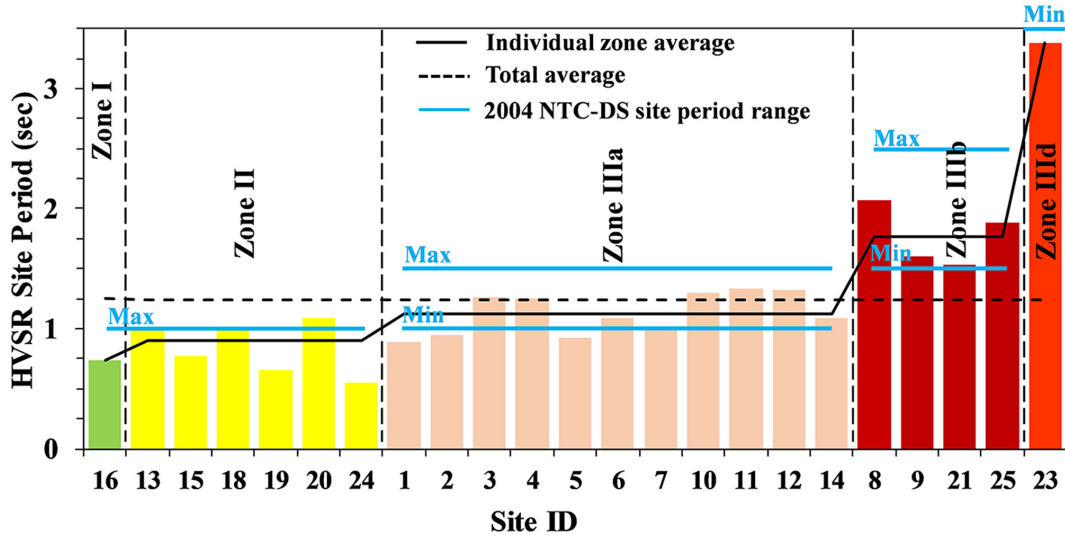


Figure 8. Summary of the measured MHVSR site periods for different seismic Zones according to the 2004 NTC-DS map (GDF, 2004).

on the 2004 NTC-DS map (GDF, 2004) and between 2.5 and 3.0 s for the Lermo et al. (2020) map, while the measured site period for Site 23 in this Zone is 3.38 s.

The most notable deviation from the 2004 site period map is in the south-western portion of the map (Figure 7a), where several deviations from the 2004 site period map ranges are observed. In this regard, the site periods for Sites 1 and 2 are 0.89 and 0.95 s, respectively, which are outside the 1.0 s contour. The Lermo et al.'s (2020) map corrects this area by moving the 1.0 s contour line to the east. Overall, the 2020 contour map improved the estimates of site period, but still has some differences from the measured (MHVSR) site periods in this study.

A summary of the measured MHVSR site periods for the western portion of the Basin is provided in Figure 8. Figure 8 contains a bar graph of the measured site periods for each testing location categorized by seismic zones along with the accepted ranges of site period recommended by the 2004 NTC-DS (GDF, 2004), as shown by blue lines. Sites 17 and 22 did not have discernible HVSR site periods, thus were omitted from the figure.

From this figure, it is clear that the most noticeable differences between the measured and the seismic zone ranges are observed in Zone IIIa, where several of the measured site periods are below the minimum value established in the 2004 NTC-DS (GDF, 2004). Moreover, Site 20 in Zone II is slightly over the maximum period for the zone. This indicates some changes in the zonations may be required in order for the sites to be correctly group by site period.

Since 2017, the NTC-DS established that for seismic design, it is necessary to obtain the design spectra and site periods of any place in Mexico City from the SASID, available at <https://sasid.unam.mx/webNormasCDMX/> (GCM, 2017, 2020). This software was used to obtain the theoretical predominant periods of the 25 measured sites. Table 2 tabulates the comparison between the measured and SASID site periods, the corresponding seismic zone of each site according to the 2004 NTC-DS site period map, and the proposed zone the sites should be in accordance with the results of this study. Figure 9 shows that the linear fit between measured and SASID site periods has a slope of 0.936 and a correlation coefficient of 0.929, indicating the close similarity of the values. This figure suggests that Sites 1, 2, and 5 are situated in Zone II instead of Zone IIIa, Site 20 in Zone IIIa instead of Zone II, and Site 23 in Zone IIIc instead of Zone IIId.

Shear wave velocity profiles with a focus on a lacustrine clay layer

The median 1D V_s profiles developed for the 25 sites tested in this study in the western portion of the Mexico City Basin are categorized based on the proposed zonation presented in Table 2 and presented in Figure 10. According to these V_s profiles, the subsurface layering of the western portion of the Mexico City Basin can be divided into five main layers up to 60 m depth. These include a crustal layer with a V_s ranging approximately between 100 and 200 m/s and a thickness less than 3 m, a very soft lacustrine clay layer with a V_s ranging approximately between 45 and 100 m/s, a soft soil layer with V_s ranging approximately between 100 and 200 m/s, a stiff soil layer with V_s ranging approximately between 300 and 415 m/s, followed by the half-space model layer with a V_s ranging approximately between 420 and 580 m/s. The depths and thickness of these layers are variable across the Basin. It should also be mentioned that not all the sites have the five main layers discussed here. For example, the very soft lacustrine clay layer was not observed in the V_s profiles of Sites 16, 17, 22, and 24. This remark coincides with the history of the sites. Sites 16 and 17 are associated with lava flows of the Xitle volcano (Siebe, 2000). The area of Sites 22 and 24 is associated with nineteenth-century brickyards, particularly, Site 22 at Parque Hundido is several meters below the street level (Pensado Leglise and Correa Etchegaray, 1996). It is very likely that part of the soft lacustrine clay layer was removed for brick fabrication at both sites. For comparison, a suspension logging V_s profile from Yamashita Architects and Engineers Inc. Oyo Corporation (1996) located between Sites 17 and 19 is provided in Figure 10 for comparison. This V_s profile shows reasonable agreement with V_s profiles in Zone II with a thin clay layer with stiffer materials below the clay.

The most critical subsurface layer in the Mexico City Basin is the very soft unconsolidated lacustrine clay layer. Therefore, the variations of the lacustrine clay properties across

Table 2. Site period comparison between measured and SASID site periods (GCM, 2020) and seismic zone comparison between the 2004 NTC-DS site period map (GDF, 2004) and a proposed seismic zone according to the results of this study

Site	Latitude	Longitude	Measured site period (s)	Site period (s) obtained from SASID	2004 zone	Proposed zone
1	19.30445	-99.12917	0.89	0.90	IIIa	II
2	19.29454	-99.13322	0.95	0.90	IIIa	II
3	19.30957	-99.11674	1.26	1.10	IIIa	IIIa
4	19.33081	-99.12665	1.25	1.30	IIIa	IIIa
5	19.33493	-99.14232	0.92	1.00	IIIa	II
6	19.34186	-99.13422	1.09	1.10	IIIa	IIIa
7	19.35220	-99.14198	0.99	1.10	IIIa	IIIa
8	19.30234	-99.10560	2.07	2.00	IIIb	IIIb
9	19.31441	-99.10928	1.60	1.30	IIIb	IIIb
10	19.30660	-99.12343	1.30	1.00	IIIa	IIIa
11	19.33679	-99.12641	1.33	1.10	IIIa	IIIa
12	19.34364	-99.12431	1.32	1.20	IIIa	IIIa
13	19.33145	-99.11256	0.99	0.70	II	II
14	19.31407	-99.12635	1.09	1.10	IIIa	IIIa
15	19.28992	-99.14285	0.78	0.60	II	II
16	19.323342	-99.15083	0.73	0.50	I	I
18	19.35633	-99.15094	1.00	1.10	II	II
19	19.34706	-99.15934	0.65	0.70	II	II
20	19.37187	-99.15643	1.09	1.10	IIIb	IIIb
21	19.39115	-99.14328	1.54	1.90	IIIc	IIIc
23	19.40897	-99.10816	3.38	3.30	II	II
24	19.38944	-99.17750	0.55	0.60	IIIb	IIIb
25	19.40028	-99.14917	1.88	2.00		

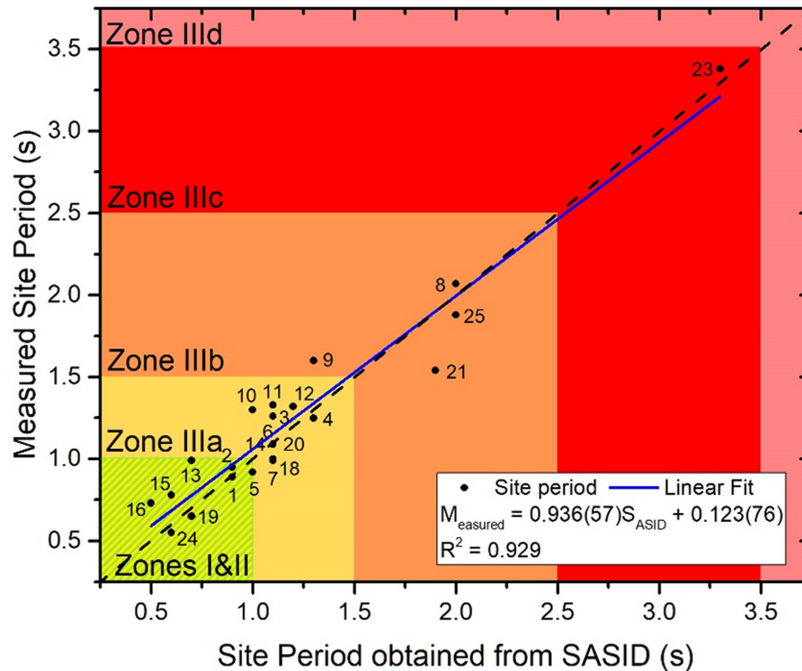


Figure 9. Correlation between measured and SASID site periods along seismic zones according to the 2004 NTC-DS map (GCM, 2020; GDF, 2004; SASID, 2020).

the western portion of the Basin are the main focus of this section. Accordingly, the shear wave velocity, depth, and thickness of the lacustrine clay layer for each individual site tested in this study are provided in Figure 11a to c, respectively, along with the seismic zonation recommended by the 2004 NTC-DS map (GDF, 2004). Sites with no clay layer in the V_s profile (Sites 16, 17, 22, and 24) are marked as N/A in this figure. For most sites, only a single V_s was resolved for the entire clay layer. However, some sites had multiple consecutive clay layers with increasing V_s with depth; thus, a time-averaged V_s was computed for them to identify the average V_s of the clay layer.

Sites in Seismic Zone II on the outer Northwest rim of the lakebed (Sites 18, 19, and 20) have relatively stiff clay layers with V_s ranging between 80 and 100 m/s, whereas the only site in this zone for the South lakebed (Site 15) has a clay layer V_s of approximately 69 m/s. However, a nearby site inside Zone IIIa (Site 2) has a clay V_s of approximately 87 m/s. The only site in Zone II between the lakebeds (Site 13) has a clay V_s of approximately 61 m/s, while a nearby site inside Zone IIIa (Site 12) has a clay V_s of approximately 69 m/s. A similar clay V_s value of 61 m/s is obtained at Site 5 in Zone IIIa, close to the border with Zone II. As noted, nearby sites fit well with sites along the outside rim. This again suggests that the border of Zone II and Zone IIIa in the 2004 NTC-DS map needs to be updated to accurately represent the subsurface conditions in the Basin. For the other six sites in the South lakebed the clay layer is very soft. Sites 1, 3, 10, and 14 in Zone IIIa and Sites 8 and 9 in Zone IIIb have clay V_s ranging approximately between 54–61 m/s and 45–49 m/s, respectively. Sites between the lakebeds in Zone IIIa (Sites 4, 6, 7, and 11) have clay layer V_s of approximately 57 m/s. The two sites in Zone IIIb in the North lakebed (Sites 21 and 25) have similar clay V_s values between 62 and 65 m/s. The only site in Zone IIId at the North lakebed (Site 23) has a clay V_s of 49 m/s.

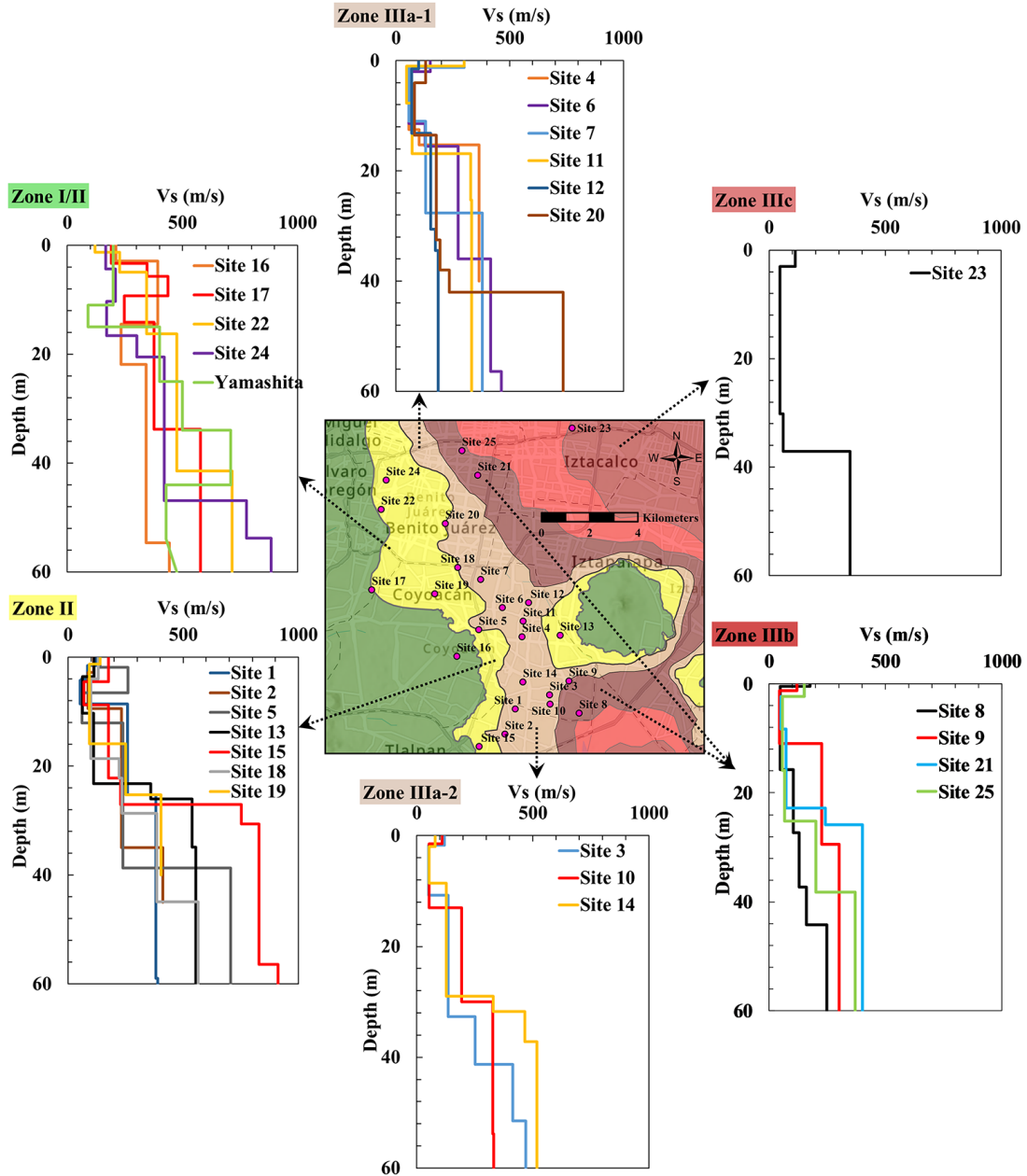


Figure 10. Median 1D V_s profiles for the 25 sites tested in this study categorized by proposed seismic zones in Table 2. A V_s profile in Zone II from Yamashita Architects and Engineers Inc. Oyo Corporation (1996) is provided for comparison. The 2004 NTC-DS zonation map (GDF, 2004) is provided for reference.

Overall, sites located along the outside of the lakebeds have higher V_s values than those within the north and South lakebeds. Sites located between the lakebeds have slightly higher clay V_s than sites in the South lakebed. The sites with the softest clay layers are located toward the centers of the lakebeds with clay V_s ranging between 45 and 50 m/s.

Depth to the clay layer varies across the Basin, with values ranging between 0.5 and 6.6 m, as illustrated in Figure 11b. Generally, sites located in Zone II and close to the border with Zone IIIa have the deepest depths to the top of the clay layer with depths ranging between 1.2 and 6.6 m, while sites located in Zone IIIa have the shallowest depths to the

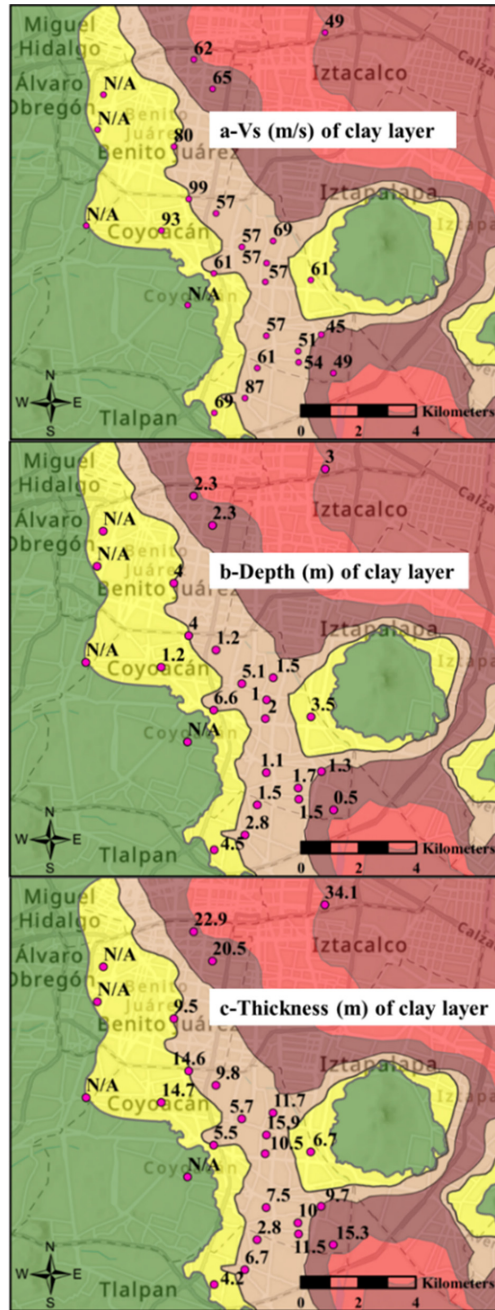


Figure 11. Variations of the lacustrine clay layer properties across the basin: (a) shear wave velocity, (b) depth to the layer, and (c) thickness of the layer. The 2004 NTC-DS zonation map (GDF, 2004) is provided for reference.

top of the clay layer with depths ranging between 1.0 and 2.8 m. Sites located in Zones IIIb and IIId in the North lakebed have a deeper depth to the top of the clay layer than sites located in Zone IIIa. Sites located in Zone IIIb in the North lakebed have deeper depths to the top of the clay layer than those located in the same Zone in the South lakebed.

The thickness of the clay layer, which is an important factor influencing the site period in the Basin, varies significantly across the western portion of the Basin. The thickest clay

layers are observed in the North lakebed in Zones IIIb (Sites 21 and 25) and IIId (Site 23), with a thickness ranging between 20.5 and 34.1 m. Generally, sites located in Zones II and IIIa have the thinnest clay layer across the western portion of the Basin with a thickness ranging between 2.8 and 10.5 m, with some exceptions for sites close to the boundary of Zone IIIa and IIIb (Sites 10, 11, and 12). Sites located in Zone II and Zone IIIb in the South lakebed have an intermediate clay layer thickness with values ranging between 4.2–14.7 m and 9.7–15.3 m, respectively.

To better illustrate the variations of the lacustrine clay layer properties across different seismic zones, box and whisker plots of the V_s of the clay layer, depth to clay layer, and thickness of the clay layer are provided in Figure 12a to c, respectively, based on the proposed seismic zones for each site in Table 2. From Figure 12a, it is apparent that the lacustrine clay layer in Zone II has the highest V_s among the other seismic zones. Moreover, the clay layer in Zone IIIb has the lowest V_s with an average value at 55 m/s. The clay layer located in Zone II starts at a deeper depth than Zones IIIa and IIIb, as shown in Figure 12b. In addition, Zone IIIb has the shallowest depth to the start of the clay layer between the seismic zones. In Figure 12c, it is clear that the thickness of the clay layer is significantly greater in Zone IIIb compared to Zones II and IIIa. The thickness of the clay layer is lower for Zone II than Zone IIIa, and Zone II has more variability than observed in Zone IIIa.

Conclusion

This study performed dynamic site characterization measurements using active and passive surface wave methods across the western portion of the Mexico City Basin that was severely affected by the Mw 7.1 September 19, 2017, Puebla–Morelos, Mexico, earthquake. Field measurements were performed using active MASW, passive MAM using an L-array, passive MAM using a circular array, and passive MHVSR. Both Rayleigh- and Love-type surface waves were utilized to enhance the reliability of the retrieved 1D shear wave velocity profile through a joint inversion process. Using the measured MHVSR site period, discussions regarding the potential bias in the site periods estimated from the 2004 NTC-DS (GDF, 2004) and Lermo et al. (2020) site period map and values computed using the SASID software following the 2020 NTC-DS (GCM, 2020) were provided. In addition, using the shear wave velocity profiles developed from the active and passive surface wave measurements, the variations of the lacustrine clay layer properties, as the most critical layer in the basin, were discussed.

Comparison of the measured MHVSR site periods to the 2004 NTC-DS (GDF, 2004) map, which is commonly used for site period prediction across the Basin, indicated that there are several sites with noticeable differences between the measured and estimated values. The most noticeable biases in the site period prediction map from the 2004 NTC-DS (GDF, 2004) were observed in the boundary of Zones II and IIIa, with five sites having shorter site periods than those associated with Zone IIIa. In addition, our results show a close similarity with SASID computed site periods values and the 2020 site period map from Lermo et al. (2020). According to the results, site periods are getting shorter in these areas as the lacustrine clay layer consolidates over time due to the subsidence produced by excessive groundwater extraction. This indicates that the seismic properties (i.e. site period) of the lacustrine clay are time-dependent, and therefore, there is a need to update the border of Zone II and Zone IIIa in the 2004 NTC-DS (GDF, 2004) site period estimation

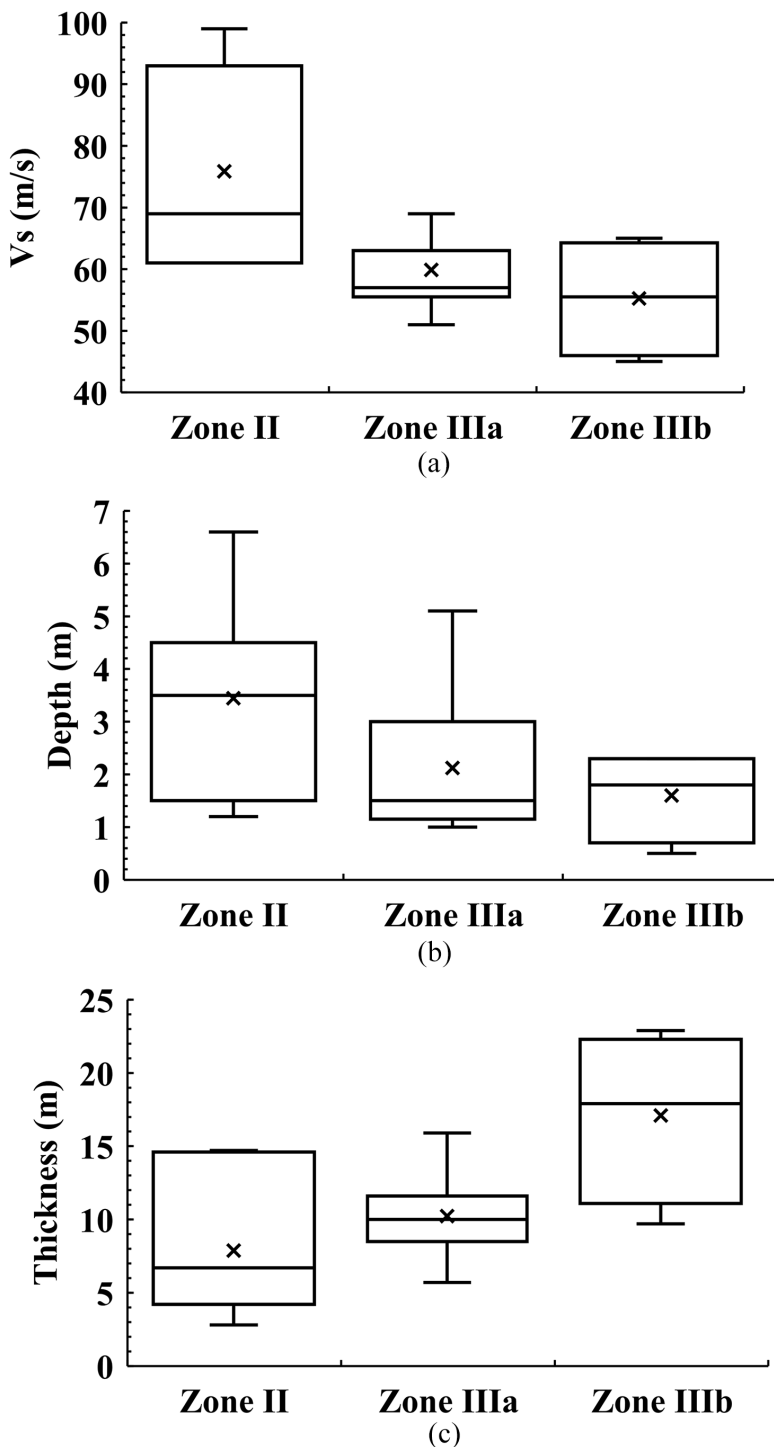


Figure 12. Box and whisker plots of lacustrine clay properties categorized by proposed seismic zones in Table 2: (a) Vs of clay layer, (b) depth to clay layer, and (c) thickness of the clay layer

map. However, in general, the 2004 NTC-DS (GDF, 2004) site period estimation map, 2020 site period map (Lermo et al., 2020), and computed values from SASID software following the 2020 NTC-DS (GCM, 2020) seem to provide reasonable site periods for the majority of the Mexico City Basin.

According to the 1D V_s profiles collected in this study, the subsurface layering of the Basin can be divided into five main layers up to 60 m depth, including a crustal layer with a V_s ranging between 100 and 200 m/s, a very soft lacustrine clay layer with a V_s ranging between 45 and 100 m/s, a soft soil layer with V_s ranging between 100 and 200 m/s, a stiff soil layer with V_s ranging between 300 and 415 m/s, followed by half-space model layer with a V_s ranging between 420 and 580 m/s. The thickness and depth of these layers, particularly the lacustrine clay layer, are quite variable across the Basin. Among these layers, the lacustrine clay layer is the most critical soil layer within the Basin since it dominates the site effects in the Basin through amplification and duration elongation of ground motions. Generally, the V_s of the clay layer depends on location. Sites along the outside of the lakebeds have higher clay V_s values than those within the North and South lakebeds. Sites between the lakebeds have slightly higher clay V_s than sites in the Southern lakebed. Sites 21 and 25 on the outer edge of the Northern lakebed in Zone IIIb were stiffer than sites in the Southern lakebed. The softest sites are toward the centers of the lakebeds with clay V_s values ranging between 45 and 57 m/s.

This study provides a detailed set of site period and 1D V_s measurements in a critical area of Mexico City, which had significant damage to infrastructure during the Mw 7.1 2017 Puebla–Morelos, Mexico, earthquake. This data set provides an excellent opportunity to update and complement the data set and model embedded in SASID software to account for site period changes in the Basin. The 1D V_s profiles provided in this study provide a detailed view of the variations of the lacustrine clay deposit and subsurface conditions on the western edge of the Basin. These data provide an excellent start to building a shallow three-dimensional (3D) velocity model of the Basin, which can complement the development of models that improve our understanding of wave propagation within of the Basin.

Declaration of conflicting interests

The author(s) declared no potential conflicts of interest with respect to the research, authorship, and/or publication of this article.

Funding

The author(s) disclosed receipt of the following financial support for the research, authorship, and/or publication of this article: This work is based on work supported the National Science Foundation through the Geotechnical Engineering Program under grant nos CMMI-1266418, CMMI-1822482, and CMMI-2100889. Any opinion, findings, and conclusions or recommendations expressed in this article are those of the authors and do not necessarily reflect the view of the NSF. Partial support from DGAPA-UNAM Project IN 107720 is appreciated. In fact, the authors thank the National Autonomous University of Mexico (UNAM) for the resources, space, and personnel who helped with the planning and collection of the field data associated with the paper including Santiago Rábade, Berenice Martínez, Diana Valencia, Fabi Mora, Joaquín Sánchez, Jorge González, along with many other people.

Data availability

Data collected for this study are freely available through the www.designsafe-ci.org/ website in the following location: <https://doi.org/10.17603/ds2-4kc2-zr63>.

References

- Arroyo D, Ordaz M, Ovando-Shelley E, Guasch JC, Lermo J, Perez C, Alcantara L and Ramírez-Centeno MS (2013) Evaluation of the change in dominant periods in the lake-bed zone of Mexico City produced by ground subsidence through the use of site amplification factors. *Soil Dynamics and Earthquake Engineering* 44: 54–66.
- Bettig B, Bard PY, Scherbaum F, Riepl J, Cotton F, Cornou C and Hatzfeld D (2001) Analysis of dense array noise measurements using the modified spatial auto-correlation method (SPAC): Application to the Grenoble area. *Bollettino di Geofisica Teoria ed Applicata* 42(3–4): 281–304.
- Capon J (1969) High-resolution frequency-wavenumber spectrum analysis. *Proceedings of the IEEE* 57(8): 1408–1418.
- Díaz-Rodríguez JA (2003) Characterization and engineering properties of Mexico City lacustrine soils. In: Tan TS, Phoon KK, Hight DW and Leroueil S (eds) *Characterization and Engineering Properties of Natural Soils*, vol. 1. London: Balkema Publishers, pp. 725–756.
- Franke KW, Candia G, Mayoral JM, Wood CM, Montgomery J, Hutchinson T and Morales-Velez AC (2019) Observed building damage patterns and foundation performance in Mexico City following the 2017 M7.1 Puebla-Mexico City earthquake. *Soil Dynamics and Earthquake Engineering* 125: 105708.
- GCM (Gobierno de la Ciudad de México) (2017) *Normas Técnicas Complementarias para Diseño por Sismo*. In: Gaceta Oficial de la Ciudad de México, no. 220Bis, Mexico. Available at: <https://www.consejeria.cdmx.gob.mx/> (Accessed 14 September 2021).
- GCM (Gobierno de la Ciudad de México) (2020) *Normas Técnicas Complementarias para Diseño por Sismo con Comentarios*. In: Gaceta Oficial de la Ciudad de México, no. 361, Mexico. Available at: <https://www.consejeria.cdmx.gob.mx/> (Accessed 14 September 2021).
- GDF (Gobierno del Distrito Federal) (2004) *Normas Técnicas Complementarias para Diseño por Sismo*. In: Gaceta Oficial del Distrito Federal, tomo II, no. 103-BIS, Mexico. Available at: <https://www.consejeria.cdmx.gob.mx/> (Accessed 14 September 2021).
- GEER (Geotechnical Extreme Events Reconnaissance Association) (2017) *Geotechnical engineering reconnaissance of the 19 September 2017 Mw 7.1 Puebla-Mexico City earthquake*, Version 2.0, Report No. GEER-055A. Available at: <https://doi.org/10.18118/G6JD46> (Accessed 14 September 2021).
- Griffiths SC, Cox BR, Rathje EM and Teague D (2016) Surface-wave dispersion approach for evaluating statistical models that account for shear-wave velocity uncertainty. *Journal of Geotechnical and Geoenvironmental Engineering* 142(11): 04016061.
- Gurler ED, Nakamura Y, Saita J and Sato T (2000) Local site effect of Mexico City based on microtremor measurement. In: *Proceedings of the 6th international conference on seismic zonation*, Palm Springs, CA, 12–15 November, pp. 65–70. Oakland, CA: Earthquake Engineering Research Institute.
- Harjes HP and Henger M (1973) Array-seismologie. *Zeitschrift für Geophysik* 39: 865–905.
- Himel AK and Wood CM (2021) Developing an updated set of Vs profiles for the central United States seismic observatory with estimates of uncertainty between different methods. *Soil Dynamics and Earthquake Engineering* 143: 106594.
- Jaimes-Viera MC, Martin del Pozzo AL, Layer PW, Benowitz JA and Nieto-Torres A (2018) Timing the evolution of a monogenetic volcanic field: Sierra Chichinautzin, Central Mexico. *Journal of Volcanology and Geothermal Research* 356: 225–242.
- Joh SH (1996) *Advances in interpretation and analysis techniques for spectral-analysis-of-surface-waves (SASW) measurements*. PhD Dissertation, Department of Civil, Architectural, and Environmental Engineering, University of Texas, Austin, TX, p. 240.
- Kelly EJ (1967) *Response of seismic arrays to wide-band signals*. Technical Note 1967-30. Cambridge, MA: Lincoln Laboratory, Massachusetts Institute of Technology. Available at: <https://apps.dtic.mil/sti/citations/AD0656344> (Accessed 14 July 2019).
- Konno K and Ohmachi T (1998) Ground-motion characteristics estimated from spectral ratio between horizontal and vertical components of microtremor. *Bulletin of the Seismological Society of America* 88(1): 228–241.

- Lermo J and Chávez-García FJ (1994) Site effect evaluation at Mexico City: Dominant period and relative amplification from strong motion and microtremor records. *Soil Dynamics and Earthquake Engineering* 13(6): 413–423.
- Lermo J, Sanchez-Sesma F, Perz E, Monroy I, Mendez N, Cuenca R, Gonzalez, Rodriguez N, Cruz I, Gonzalez N, Maldonado D, Espinoza O, Gonzalez K, Cruz J, Gonzalez H, Aragon J and Mendez J (2020) *Updating of the Seismic Zoning of Mexico City and Surrounding Areas Northern Part*. Mexico City, Mexico: Institute for Construction Safety, Government of Mexico City.
- Mayoral JM, Asimaki D, Tepalcapa S, Wood C, Roman-de la Sancha A, Hutchinson T, Franke K and Montalva G (2019) Site effects in Mexico City basin: Past and present. *Soil Dynamics and Earthquake Engineering* 121: 369–382.
- Mayoral JM, Castañon E, Alcantara L and Tepalcapa S (2016) Seismic response characterization of high plasticity clays. *Soil Dynamics and Earthquake Engineering* 84: 174–189.
- Mayoral JM, Romo MP and Osorio L (2008) Seismic parameters characterization at Texcoco lake, Mexico. *Soil Dynamics and Earthquake Engineering* 28(7): 507–521.
- O’Riordan N, Cañavate-Grimal A, Francisco Ciruela-Ochoa F and Kumar S (2017) The stiffness and strength of saltwater Lake Texcoco clays, Mexico City. In: *Proceedings of the 19th international conference on soil mechanics and geotechnical engineering*, Seoul, South Korea, 17–22 September, pp. 1067–1070. London: International Society for Soil Mechanics and Geotechnical Engineering.
- Pensado Leglise MP and Correa Etchegaray L (1996) *Mixcoac: Un barrio en la memoria*. Mexico City, Mexico: Instituto Mora.
- Pestana JM, Sancio RB, Bray JD, Romo MP, Mendoza MJ, Moss RES, Mayoral MJ and Seed RB (2002) Geotechnical engineering aspects of the June 1999 Central Mexico earthquakes. *Earthquake Spectra* 18(3): 481–499.
- Rahimi S, Wood CM and Teague DP (2021) Performance of different transformation techniques for MASW data processing considering various site conditions, near-field effects, and modal separation. *Surveys in Geophysics* 42(5): 1197–1225.
- Rahimi S, Wood CM, Coker F, Moody T, Bernhardt-Barry M and Mofarraj Kouchaki B (2018) The combined use of MASW and resistivity surveys for levee assessment: A case study of the Melvin Price Reach of the Wood River Levee. *Engineering Geology* 241: 11–24.
- Reinoso E, Ordaz M and y Sánchez-Sesma FJ (1990) A note on the fast computation of response spectra estimates. *Earth Engineering and Structural Dynamics* 19: 971–976.
- Romo MP (1995) Clay behavior, ground response and soil-structure interaction studies in Mexico City. In: *Proceedings of the 3rd international conference on recent advances in geotechnical earthquake engineering and soil dynamics*, St. Louis, MO, 2–7 April, pp. 1039–1051. Rolla, MO: Missouri University of Science and Technology.
- Romo MP, Jaime A and Reséndiz D (1988) The Mexico earthquake of September 19, 1985-general soil conditions and clay properties in the valley of Mexico. *Earthquake Spectra* 4(4): 731–752.
- Rosenblueth E, Ordaz M, Sánchez-Sesma FJ and Singh SK (1989) The Mexico earthquake of September 19, 1985—Design spectra for Mexico’s Federal District. *Earthquake Spectra* 5(1): 273–291.
- Santoyo E, Ovando E, Mooser F and León E (2005) *Síntesis Geotécnica de la Cuenca del Valle de México*. Mexico City, Mexico: TCG.
- SASID (Normas Técnicas Complementarias para Diseño por Sismo de la Ciudad de México) (2020) NTC-SISMO CDMX. Available at: <https://sasid.unam.mx/webNormasCDMX/> (Accessed 14 September 2021).
- Seed HB, Romo MP, Sun JI, Jaime A and Lysmer J (1988) The Mexico earthquake of September 19, 1985—Relationships between soil conditions and earthquake ground motions. *Earthquake Spectra* 4(4): 687–729.
- SESAME European Research Project (2004) *Guidelines for the implementation of the H/V spectral ratio technique on ambient vibration: Measurements, processing and interpretations*. Research General Directorate Project No. EVG1-CT-2000-00026. Brussels: European Commission.
- Siebe C (2000) Age and archaeological implications of Xitle volcano, southwestern Basin of Mexico-City. *Journal of Volcanology and Geothermal Research* 104(1): 45–64.

- Singh SK, Reinoso E, Arroyo D, Ordaz M, Cruz-Atienza V, Pérez-Campos X, Iglesias A and Hjörleifsdóttir V (2018) Deadly intraslab Mexico earthquake of 19 September 2017 (Mw 7.1): Ground motion and damage pattern in Mexico City. *Seismological Research Letters* 89(6): 2193–2203.
- Wathelet M (2008) An improved neighborhood algorithm: Parameter conditions and dynamic scaling. *Geophysical Research Letters* 35(9): L09301.
- Wood C, Woodfield L and Rieth R (2020) Dynamic site characterization in Mexico City following the 2017 Mw 7.1 Puebla-Mexico City earthquake. Available at: <https://doi.org/10.17603/ds2-4kc2-zr63> (Accessed 14 November 2020).
- Wood CM and Baker ER (2018) Cost savings of implementing site-specific ground motion response analysis in the design of short-period Mississippi embayment bridges. *Earthquake Spectra* 34(3): 1155–1175.
- Wood CM and Cox BR (2012) A comparison of MASW dispersion uncertainty and bias for impact and harmonic sources. In: *Proceedings of the GeoCongress 2012: State of the art and practice in geotechnical engineering*, Oakland, CA, 25–29 March, pp. 2756–2765. Reston, VA: Geo-Institute.
- Wood CM, Deschenes M, Ledezma C, Meneses J, Montalva G and Morales-Velez AC (2019) Dynamic site characterization of areas affected by the 2017 Puebla-Mexico city earthquake. *Soil Dynamics and Earthquake Engineering* 125: 105704.
- Woodfield LJ (2020) *Development of Vs profiles and site periods in the Mexico City basin*. Graduate Theses and Dissertations, University of Arkansas, Fayetteville, AR.
- Yamashita Architects and Engineers Inc. Oyo Corporation (1996) *Estudios del subsuelo del Valle de México*. Cuadernos de Investigación, No. 34, Centro Nacional de Prevención de Desastres, Mexico City, Mexico, p. 91.
- Zywicki DJ (1999) *Advanced signal processing methods applied to engineering analysis of seismic surface waves*. Doctoral Dissertation, Georgia Institute of Technology, Atlanta, GA.

4. Otros productos y actividades

La Universidad Nacional Autónoma de México tiene como fines educar, investigar y difundir la cultura. Estas tres áreas deben cubrirse conforme se avanza en la preparación del alumnado. Desde mi ingreso al posgrado he realizado actividades en éstas tres áreas encaminadas hacia una formación integral que refleje haber sido alumno del Posgrado en Ciencias de la Tierra. Sin profundizar en las actividades y productos académicas en los que he colaborado y los eventos en los que participé, los cuales merecen ser reconocidas pues han contribuido a mi formación profesional y como investigador del área, aprovecho este espacio para mencionar brevemente el trabajo realizado durante los años dedicados al doctorado.

Adicionalmente a los artículos mencionados en este escrito, he colaborado en la publicación de tres artículos en revistas indizadas (ver productos 1 a 3 en la siguiente lista), en dos artículos aceptados en revistas indizadas con revisiones menores (ver productos 4 y 5 en la siguiente lista) y en un artículo en extenso y/o memorias (ver producto 6 en la siguiente lista):

1. Wood, C. M., Rieth R. M., Rahimi, S., Rahimi M., Rosado-Fuentes, A., Mayoral, J. M., de la Rosa, D., Sánchez-Sesma, F. J. & Cruz-Jiménez, H. (2024). Shallow 3D Shear Wave Velocity Model for the Mexico City Basin. *Earthquake Spectra*, 40(1), 314-345. <https://doi.org/10.1177/87552930231222458>.
2. Mendo-Pérez, G., Arciniega-Ceballos, A., Matoza, R. S., Rosado-Fuentes, A., Sanderson, R. W., & Chouet, B. A. (2021). Ground-coupled airwaves template match detection using broadband seismic records of explosive eruptions at Popocatépetl volcano, Mexico. *Journal of Volcanology and Geothermal Research*, 419, 107378. <https://doi.org/10.1016/j.jvolgeores.2021.107378>
3. Matoza, R. S., Arciniega-Ceballos, A., Sanderson, R. W., Mendo-Pérez, G., Rosado-Fuentes, A. & Chouet, B.A. (2019). High broadband seismo-acoustic signature of Vulcanian explosions at Popocatépetl volcano, Mexico. *Geophysical Research Letters*, 46(1), 146 - 157. <https://doi.org/10.1029/2018GL080802>. Imagen seleccionada para la portada del ejemplar correspondiente.
4. Mendo-Pérez, G., Arciniega-Ceballos, A., Matoza, R. S., Rosado-Fuentes, A., Sanderson, R. W., & Claypool M. R. (Mayo 10, 2024). Seismo-acoustic wavefield at Popocatépetl volcano, Mexico captured by a temporary broadband network from 2021 to 2022. *Seismological Research Letters*. Manuscript number SRL-D-24-00199R1.
5. Baena-Rivera, M., Arciniega-Ceballos, A., Sánchez-Sesma, F. J., Rosado-Fuentes, A. & Pardo-Dañino, J. C. (Octubre 1, 2023). Directional HVSR in the Chalco lakebed zone of the Valley of Mexico. *Journal of Applied Geophysics*. Manuscript number APPGEO-D-23-00614.

6. Rosado-Fuentes, A. (2020). Wavefields: characteristics and properties. Libro de Congreso: *Humboldt Kolleg on Measuring Nature's Wavefields: Alexander von Humboldt's Time and Today*, CDMX, México. Enero 30 - Febrero 1, 2020. 25-26.

Las investigaciones en las que colaboré se presentaron como carteles en 9 congresos y/o reuniones internacionales como Latin American and Caribbean Seismological Commission, American Geophysical Union, Society of American Archaeology, European Geophysical Union, Japan Geoscience Union e International Union of Geodesy and Geophysics; en 4 congresos y/o reuniones nacionales como Unión Geofísica Mexicana, Congreso Nacional de Física y Encuentro de Arqueología de Noreste y con una ponencia en un Humboldt Kolleg. Fui miembro del Comité Organizador de una serie de charlas en la Facultad de Ciencias-UNAM (2023) y del Simposio Latinoamericano de Física y Química en Arqueología, Arte y Conservación de Patrimonio Cultural 2019. Igualmente asesoré, revisé, repare o puse en operación equipo de exploración geofísica usado para la docencia e investigación de la Escuela Nacional de Antropología e Historia y del Instituto de Geofísica.

Los productos académicos mencionados en este escrito y en este capítulo han sido por mi participación en tres proyectos de investigación que ya concluyeron (UC-MEXUS-CONACYT: CN 18-51, PAPIIT-UNAM: IN108219 e IN105716) y en dos que están en curso (CONACYT: 320343, PAPIIT-UNAM: IN104823). La constante capacitación y actualización de conocimientos en las Ciencias de la Tierra me llevó a tomar 15 cursos impartidos por la Sociedad Mexicana de Ingeniería Geotécnica, Facultad de Ciencias-UNAM, Sociedad Mexicana de Física, Instituto de Ingeniería-UNAM, Instituto de Geofísica-UNAM e Instituto Panamericano de Geografía e Historia; igualmente participé en el Summer of Applied Geophysical Experience y en la elaboración de un peritaje matemático en un juicio civil en la ciudad de La Paz, Baja California Sur.

En el área de la docencia, imparti 26 cursos como profesor titular en las licenciaturas de Física en la Facultad de Ciencias, y Ciencias de la Tierra en la Facultad de Ciencias y en la Escuela Nacional de Ciencias de la Tierra. También fui sinodal en dos exámenes de grado en la licenciatura de Ciencias de la Tierra en la Facultad de Ciencias. Esto conlleva elaborar, actualizar o mejorar el material docente de 9 asignaturas de licenciatura: Geofísica Aplicada 1 y 2, Mecánica de Medios Deformables, Matemáticas 3, Laboratorios de Física Contemporánea 1, Fenómenos Colectivos y Electromagnetismo, Técnicas Experimentales y Métodos Geofísicos de Exploración. Fui tutor de dos alumnos que participaron en congresos académicos en la Facultad de Ciencias y apoyé la liberación de las prácticas profesionales de cuatro alumnos de Ingeniería Geofísica de la Facultad de Ingeniería-UNAM.

En el área de la difusión y divulgación de las ciencias, en particular de las Ciencias de la Tierra y los temas de mi doctorado, imparti cinco conferencias y/o seminarios en el Museo de Geofísica del Instituto de Geofísica-UNAM, Grupo MARQ y Club Rotary Anáhuac Tacubaya. Colaboré elaborando contenido y figuras que forman parte de la aplicación móvil *Sismos y Volcanes CDMX* y participé como tallerista en 23 eventos de divulgación organizados por el Museo de Geofísica, la Facultad de Ciencias y el Instituto de Geología.

Conclusiones

Se ha presentado un compendio de tres artículos publicados en revistas indizadas que abarcan estudios de exploración geofísica multi-técnica somera no destructiva en diversos sitios dentro de la Cuenca de México en donde se emplearon, en cada uno de ellos, al menos dos técnicas distintas. Dos de ellos se realizaron en el Campo de Pruebas Geofísicas de Teoloyucan (TGTS), ubicado dentro del Observatorio Geomagnético de Teoloyucan, UNAM en el municipio de Teoloyucan, Estado de México, mismo que fue diseñado y construido como se indica en el primer artículo; mientras que el tercer artículo abarca la zona occidental de la CDMX, la cual sufrió graves daños por el sismo de Mw 7.1 de Puebla-Morelos de 2017.

Con la construcción del TGTS, la UNAM cuenta ahora con un campo de pruebas diseñado para calibrar equipo e instrumentos, probar técnicas de exploración geofísica somera, capacitar estudiantes e investigar nuevas ideas, técnicas de exploración geofísica somera e interpretación de datos enfocados a contextos de ingeniería, arqueología y patrimonio cultural. Los resultados de la caracterización geofísica del sitio, aplicando gradiente magnético, inducción electromagnética, radar de penetración terrestre y tomografías de refracción sísmica y resistividad eléctrica, muestran que en lugares como Teoloyucan los primeros 3 m de profundidad están conformados por cuatro capas relativamente planas con pequeñas protuberancias, con una distribución suave de propiedades físicas y sin la presencia de discontinuidades ni cambios abruptos. Los resultados granulométricos y la sección litoestratigráfica del sitio muestran que el primer metro de profundidad está conformado por cuatro capas de suelo grueso bien gradado, incluyendo dos tepetates de origen volcánico. La integración de los resultados fue la base para el diseño y construcción del TGTS. Esta integración y la concordancia entre las interfaces geofísicas y litológicas indican que el sitio seleccionado es ideal para la construcción del TGTS.

Adicionalmente, se introduce la novedosa técnica de Gradiente de Inducción Electromagnética (EMIG - por sus siglas en inglés) desarrollada para resaltar fuentes locales y someras, mejorando así su identificación y localización dentro de los espesores del subsuelo mapeados por la técnica de inducción electromagnética. Mediante la aplicación conjunta de gradiente magnético (MG) e inducción electromagnética (EMI) en el TGTS se complementaron las metodologías convencionales de adquisición y procesamiento de datos de MG y EMI que incluyen mapear y sumar dos levantamientos adquiridos con transectos paralelos pero perpendiculares entre sí, calcular el EMIG y realizar mapas de acercamiento a áreas más pequeñas. Tanto el uso del EMIG como la metodología propuesta muestran resultados sobresalientes a los que se obtendrían con las técnicas y metodologías convencionales, resaltando anomalías que de otra manera, sin la metodología propuesta, pasarían por alto. Además, la comparación de los levantamientos de transectos ortogonales muestra diferencias significativas en la distribución de las propiedades físicas del subsuelo debidas a la dirección de adquisición, la orientación de los transectos y a la orientación y rumbo de los sensores. La posible contribución de efectos anisotrópicos no debe descartarse, aunque se requieren estudios más detallados

que están fuera de los alcances de los trabajos presentados en este escrito. Recomendamos replicar la metodología en otros sitios de estudio somero en contextos de ingeniería, arqueología, patrimonio cultural o forense.

Por otra parte, se estudiaron sísmicamente los primeros 60 *m* de profundidad en 25 sitios distribuidos en la zona occidental de la CDMX mediante la aplicación de las técnicas de análisis multicanal de ondas superficiales, arreglo multicanal de microtremores y cociente espectral H/V. Adicionalmente se calcularon los períodos fundamentales de sitio. Su comparativa con los publicados por otros estudios muestra ligeras discrepancias, indicando que las propiedades del subsuelo son variables en el tiempo y evidenciando la necesidad de actualizar y complementar constantemente las bases de datos y parámetros de las Normas Técnicas Complementarias por Diseño Sísmico de la CDMX. Con especial atención se analizó a detalle la capa crítica de arcilla lacustre blanda no consolidada, determinando su valor de V_s y espesor a lo largo del área de estudio. Los perfiles 1D de V_s se pueden utilizar para construir un modelo tridimensional de V_s de la parte somera de la Cuenca que complemente los modelos y amplíe la comprensión de la propagación de ondas sísmicas dentro de ella.

El grupo de investigación conformado usa constantemente el TGTS para la docencia, probar y calibrar equipos y continuar nuestras investigaciones, los resultados se continuarán presentando en congresos nacionales e internacionales y serán publicados en revistas indizadas en un futuro próximo. Finalmente, los estudios mostrados en este escrito y el resto de las actividades realizadas durante el lapso del doctorado han contribuido a mi formación integral en el área de las Ciencias de la Tierra. Las actividades no solo reflejan la experiencia adquirida, sino que también impulsan el desarrollo y el conocimiento científico al contribuir e innovar en el avance de la ciencia y la tecnología, al igual que se transmiten con veracidad los conocimientos adquiridos a la sociedad.

Referencias

- Aki, K. (1957). Space and Time Spectra of Stationary Stochastic Waves, with Special Reference to Microtremors. *Bulletin of the Earthquake Research Institute*, 35(3):415-456. <https://oceanrep.geomar.de/id/eprint/43280/>.
- Alcocer, J. y Williams, W. D. (1996). Historical and recent changes in Lake Texcoco, a saline lake in Mexico. *International Journal of Salt Lake Research*, 5(1):45-61. <https://doi.org/10.1007/BF01996035>.
- Arroyo, D., Ordaz, M., Ovando-Shelley, E., Guasch, J. C., Lermo, J., Perez, C., Alcantara, L., y Ramírez-Centeno, M. S. (2013). Evaluation of the change in dominant periods in the lake-bed zone of Mexico City produced by ground subsidence through the use of site amplification factors. *Soil Dynamics and Earthquake Engineering*, 44:54-66. <https://doi.org/10.1016/j.soildyn.2012.08.009>.
- Asten, M. W. y Henstridge, J. D. (1984). Array estimators and the use of microseisms for reconnaissance of sedimentary basins. *Geophysics*, 49(11):1828-1837. <https://doi.org/10.1190/1.1441596>.
- Blancas-Vázquez, J. E., Cortés-Ávila, F. J., Gómez-Vázquez, M. y Alatriste-Vilchis, D. R. (1996). Adquisición y Procesamiento de Datos de GPR en un Campo de Pruebas. En *VII Simposium de Geofísica y Exposición*, páginas 281-288, Veracruz, Mexico. Asociación Mexicana de Geofísicos de Exploración. <https://www.researchgate.net>.
- Campos-Enríquez, J. O., Delgado-Rodríguez, O., Chávez-Segura, R., Gómez-Contreras, P., Flores-Márquez, E. L., y Birch, F. S. (1997). The subsurface structure of the Chalco sub-basin (Mexico City) inferred from geophysical data. *Geophysics*, 62(1):23-35. <https://doi.org/10.1190/1.1444123>.
- Chávez-García, F. J. y Bard, P. (1994). Site effects in Mexico City eight years after the September 1985 Michoacan earthquakes. *Soil Dynamics and Earthquake Engineering*, 13(4):229-247. [https://doi.org/10.1016/0267-7261\(94\)90028-0](https://doi.org/10.1016/0267-7261(94)90028-0).
- De Smedt, P., Saey, T., Meerschman, E., De Reu, J., De Clercq, W. y Van Meirvenne, M. (2014). Comparing Apparent Magnetic Susceptibility Measurements of a Multi-receiver EMI sensor with Topsoil and Profile Magnetic Susceptibility Data over Weak Magnetic Anomalies. *Archaeological Prospection*, 21(2):103-112. <https://doi.org/10.1002/arp.1467>.
- Erkan, K. (2008). *A Comparative Overview of Geophysical Methods, Report No. 488*. The Ohio State University, Columbus, OH, USA. <https://core.ac.uk/download/pdf/159585702.pdf>.
- Everett, M. E. (2013). *Near-Surface Applied Geophysics*. Cambridge University Press, UK. <https://doi.org/10.1017/CBO9781139088435>.

- Franke, K. W., Candia, G., Mayoral, J. M., Wood, C. M., Montgomery, J., Hutchinson, T., y Morales-Velez, A. C. (2019). Observed building damage patterns and foundation performance in Mexico City following the 2017 m7.1 Puebla-Mexico City earthquake. *Soil Dynamics and Earthquake Engineering*, 125:105708. <https://doi.org/10.1016/j.soildyn.2019.105708>.
- GCM (2017). Gobierno de la Ciudad de México. Normas Técnicas Complementarias para Diseño por Sismo. En *Gaceta Oficial de la Ciudad de México, no 220Bis, capítulo 2*, páginas 44-83. CDMX, México. <https://www.consejeria.cdmx.gob.mx>.
- GDF (2004). Gobierno del Distrito Federal. Normas Técnicas Complementarias para Diseño por Sismo. En *Gaceta Oficial del Distrito Federal, tomo II, no. 103-BIS, capítulo 4*, páginas 55-77. CDMX, México. <https://www.consejeria.cdmx.gob.mx>.
- GEER (2017). Geotechnical Extreme Events Reconnaissance Association. *Geotechnical engineering reconnaissance of the 19 September 2017 Mw 7.1 Puebla-Mexico City Earthquake: version 1.0. Report no. GEER 055-A*, GEER. Recuperado el 15 de enero de 2024. <https://geerassociation.org>.
- GF Instruments (2020). *Short Guide for Electromagnetic Conductivity Mapping and Tomography*. GF Instruments. <http://www.gfinstruments.cz>.
- Gres-Hernández, G. (2010). *Análisis de Espectrogramas de Anomalías Magnéticas Para la Deteción de Estructuras*. Tesis de licenciatura. TesiUNAM, Universidad Nacional Autónoma de México. <https://tesiunam.dgb.unam.mx/>.
- Guillemoteau, J., Simon, F. X., Hulin, G., Dousteysier, B., Dacko, M. y Tronicke, J. (2019). 3-D imaging of subsurface magnetic permeability/susceptibility with portable frequency domain electromagnetic sensors for near surface exploration. *Geophysical Journal International*, 219(3):1773-1785. <https://doi.org/10.1093/gji/ggz382>.
- Guillemoteau, J. y Tronicke, J. (2015). Non-standard electromagnetic induction sensor configurations: Evaluating sensitivities and applicability. *Journal of Applied Geophysics*, 118:15-23. <https://doi.org/10.1016/j.jappgeo.2015.04.008>.
- Harjes, H. P. y Henger, M. (1973). Array-seismologie. *Zeitschrift für Geophysik*, 39:865-905.
- Isaacson, J., Hollinger, R. E., Gundrum, D., y Baird, J. (1999). A Controlled Archaeological Test Site Facility in illinois: Training and Research in Archaeogeophysics. *Journal of Field Archaeology*, 26(2):227-236. <https://doi.org/10.1179/jfa.1999.26.2.227>.
- Joh, S. H. (1966). *Advances in interpretation and analysis techniques for spectral-analysis-of-surfacewaves (SASW) measurements*. Tesis de doctorado, University of Texas Libraries, University of Texas at Austin, TX, E.E.U.U. <https://search.lib.utexas.edu>.
- Kawase, H. and Aki, K. (1989). A study on the response of a soft basin for incident S, P, and Rayleigh waves with special reference to the long duration observed in Mexico City. *Bulletin of the Seismological Society of America*, 79(5):1361-1382. <https://doi.org/10.1785/BSSA0790051361>.

- Klose, T., Guillemoteau, J., Simon, F. X. y Tronicke, J. (2018). Toward subsurface magnetic permeability imaging with electromagnetic induction sensors: Sensitivity computation and reconstruction of measured data. *Geophysics*, 83(5):E335-E345. <https://doi.org/10.1190/geo2017-0827.1>.
- Langel, R. A. y Hinze, W. J. (1998). *The magnetic field of the Earth' lithosphere: the satellite perspective*, 1a edición. Cambridge University Press, E.E.U.U.
- Lermo, J. y Chávez-García, F. J. (1993). Site effect evaluation using spectral ratios with only one station. *Bulletin of the Seismological Society of America*, 83(5):1574-1594. <https://doi.org/10.1785/BSSA0830051574>.
- Lermo, J. y Chávez-García, F. J. (1994). Site effect evaluation at Mexico City: Dominant period and relative amplification from strong motion and microtremor records. *Soil Dynamics and Earthquake Engineering*, 13(6):413-423. [https://doi.org/10.1016/0267-7261\(94\)90012-4](https://doi.org/10.1016/0267-7261(94)90012-4).
- Lermo, J., Sanchez-Sesma, F. J., Ramos Pérez, E., Álvarez Monroy, I., Jiménez Mendez, N., Torres Cuenca, R., Machado González O. R. Téllez Rodríguez, N. A., Luna Cruz, I., Crespo González, N., López Maldonado, D., Huerta Espinoza, O., Castañeda González, K. Y., Luna Cruz, J. I., Lorenzo González, H., Pérez Aragon, J. F. y Luna Méndez, J. F. (2020). Actualización de la zonificación sísmica de la Ciudad de México y áreas aledañas - Parte Norte. Informe Técnico. Recuperado el 15 de enero de 2024. <https://transparencia.cdmx.gob.mx/storage/app/uploads/public/603/44b/1c6/60344b1c69beb045505965.pdf>.
- Lin, C. P. y Chang, T. S. (2004). Multi-station analysis of surface wave dispersion. *Soil Dynamics and Earthquake Engineering*, 24(11):877-886. [urlhttps://doi.org/10.1016/j.soildyn.2003.11.011](https://doi.org/10.1016/j.soildyn.2003.11.011).
- Lozano-García, M. y Ortega-Guerrero, B. (1998). Late Quaternary environmental changes of the central part of the Basin of Mexico; correlation between Texcoco and Chalco basins. *Review of Palaeobotany and Palynology*, 99(2):77-93. [https://doi.org/10.1016/S0034-6667\(97\)00046-8](https://doi.org/10.1016/S0034-6667(97)00046-8).
- Mayoral, J. M., Romo, M. P. y Osorio, L. (2008). Seismic parameters characterization at Texcoco lake, Mexico. *Soil Dynamics and Earthquake Engineering*, 28(7):507-521. <https://doi.org/10.1016/j.soildyn.2007.08.004>.
- Mayoral, J. M., Castanon, E., Alcantara, L. y Tepalcapa, S. (2016). Seismic response characterization of high plasticity clays. *Soil Dynamics and Earthquake Engineering*, 84:174-189. <https://doi.org/10.1016/j.soildyn.2016.02.012>.
- Mayoral, J. M., Asimaki, D., Tepalcapa, S., Wood, C. M., Roman-de la Sancha, A., Hutchinson, T., Franke, K. y Montalva, G. (2019). Site effects in Mexico City Basin: Past and present. *Soil Dynamics and Earthquake Engineering*, 121:369-382. <https://doi.org/10.1016/j.soildyn.2019.02.028>.
- McNeill, J. D. (1980). *Electromagnetic terrain conductivity measurements at low induction numbers. Technical Note TN-6*, pp. 17. Geonics Limited. <http://www.geonics.com>.

- McNeill, J. D. y Bosnar, M. (1999). *Application of ‘dipole-dipole’ electromagnetic systems for geological depth sounding. Technical Note TN-31*, pp. 17. Geonics Limited. <http://www.geonics.com>.
- Molina-Villegas, J. C., Jaramillo-Fernández, J. D., Piña-Flores, J. y Sánchez-Sesma, F. J. (2018). Local generation of Love Surface Waves at the Edge of a 2D Alluvial Valley. *Bulletin of the Seismological Society of America*, 108(4):2090-2103. <https://doi.org/10.1785/0120170360>.
- Mooser, F., Nairn, A. E. M. y Negendank, J. F. W. (1974). Palaeomagnetic investigations of the tertiary and quaternary igneous rocks: VIII a palaeomagnetic and petrologic study of volcanics of the valley of Mexico. *Geologische Rundschau*, 63(2):451-483. <https://doi.org/10.1007/BF01820824>.
- Mooser, F. (1975). Historia geológica de la Cuenca de México. En *Memorias de las Obras del Sistema de Drenaje Profundo del Distrito Federal (tomo 1)*, páginas 7-38. DDF, Secciones Geológicas.
- Nakamura, Y. (1989). A method for dynamic characteristics estimation of subsurface using microtremor on the ground surface. *Railway Technical Research Institute. Quarterly Reports*, 30(1):25-33.
- Padilla y Sánchez, R. J. (1989). Geology and tectonics of the basin of Mexico and their relationship with the damage caused by the earthquakes of September 1985. *International Journal of Mining and Geological Engineering*, 7(1):17-28. <https://doi.org/10.1007/BF01552836>.
- Pandey, B., Jakka, R. S., Kumar, A. y Mittal, H. (2016). Site Characterization of Strong-Motion Recording Stations of Delhi Using Joint Inversion of Phase Velocity Dispersion and H/V Curve. *Bulletin of the Seismological Society of America*, 106(3):1254-1266. <https://doi.org/10.1785/0120150135>.
- Park, C. B., Miller, R. D. y Xia, J. (1999). Multichannel analysis of surface waves. *Geophysics*, 64(3):800-808. <https://doi.org/10.1190/1.1444590>.
- Park, C. B., Miller, R. D., Ryden, N., Xia, J. e Ivanov, J. (2005a). Combined Use of Active and Passive SurfaceWaves. *Journal of Environmental and Engineering Geophysics*, 10(3):323334. <https://doi.org/10.2113/JEEG10.3.323>.
- Park, C. B., Miller, R. D., Laflen, D., Neb, C., Ivanov, J., Bennett, B. y Huggins, R. (2005b). Imaging dispersion curves of passive surface waves. En *SEG Technical Program Expanded Abstracts 2004* (pp. 1357-1360). Society of Exploration Geophysics. <https://doi.org/10.1190/1.1851112>.
- Pérez-Rocha, L. E., Sánchez-Sesma, F. J. y Flores-Cruz, F. (1995). Análisis de los datos de la Red Acelerométrica del Valle de México con técnicas espectrales. *Revista de Ingeniería Sísmica*, 49:21-38.

- Pestana, J. M., Sancio, R. B., Bray, J. D., Romo, M. P., Mendoza, M. J., Moss, R. E. S., Moyal, J. M. y Seed, R. B. (2002). Geotechnical Engineering Aspects of the June 1999 Central Mexico Earthquakes. *Earthquake Spectra*, 18(3):481-499. <https://doi.org/10.1193/1.1503340>.
- Pringle, J. K., Ruffell, A., Jervis, J. R., Donnelly, L., McKinley, J., Hansen, J., Morgan, R., Pirrie, D. y Harrison, M. (2012). The use of geoscience methods for terrestrial forensic searches. *Earth-Science Reviews*, 114(1):108-123. <https://doi.org/10.1016/j.earscirev.2012.05.006>.
- Quiroz-Suárez, D. (2020). *Métodos de exploración geofísica somera aplicados para la caracterización de inhumaciones: caso experimental y real*. Tesis de maestría. TesiUNAM, Universidad Nacional Autónoma de México. <https://tesiunam.dgb.unam.mx/>.
- Reynolds, J. M. (1997). *An Introduction to Applied and Environmental Geophysics*. John Wiley & Sons, Inglaterra.
- Rosado-Fuentes, A., Arciniega-Ceballos, A., Hernández-Quintero, E., Arango-Galván, C., Salas-Corrales, J. L. y Mendo-Pérez, G. (2021). Geophysical characterization, design and construction of the Teoloyucan Geophysical Test Site for archaeological and engineering applications, Central Mexico. *Journal of Applied Geophysics*, 194:104459. <https://doi.org/10.1016/j.jappgeo.2021.104459>.
- Rosado-Fuentes, A., Arciniega-Ceballos, A., Hernández-Quintero, E., Arango-Galván, C., Salas-Corrales, J. L. y Mendo-Pérez, G. (2023). Mapping near-surface structures in a geophysical test site using magnetic and electromagnetic induction gradients. *Journal of Applied Geophysics*, 215:105123. <https://doi.org/10.1016/j.jappgeo.2023.105123>.
- Sánchez-Sesma, F. J., Pérez-Rocha, L. E. y Reinoso, E. (1993). Ground motion in Mexico City during the April 25, 1989, Guerrero earthquake. *Tectonophysics*, 218(1):127-140. [https://doi.org/10.1016/0040-1951\(93\)90264-K](https://doi.org/10.1016/0040-1951(93)90264-K).
- Sánchez-Sesma, F. J., Rodríguez, M., Iturrarán-Viveros, U., Luzón, F., Campillo, M., Marquerin, L., García-Jerez, A., Suárez, M., Santoyo, M. y Rodríguez-Castellanos, A. (2011). A theory for microtremor H/V spectral ratio: application for a layered medium. *Geophysical Journal International*, 186(1):221-225. <https://doi.org/10.1111/j.1365-246X.2011.05064.x>.
- Santoyo Villa, E., Ovando Shelley, E., Mooser, F. y León Plata, E. (2005). *Síntesis Geotécnica de la Cuenca del Valle de México*. TGC, Ciudad de México, México.
- SEDATU (2024). Secretaría de Desarrollo Agrario, Territorial y Urbano. *Metrópolis de México 2020*. Secretaría de Desarrollo Agrario, Territorial y Urbano, Consejo Nacional de Población e Instituto Nacional de Estadística y Geografía, México.
- Seed, H. B., Romo, M. P., Sun, J. I., Jaime, A. y Lysmer, J. (1988). The Mexico Earthquake of September 19, 1985—Relationships between Soil Conditions and Earthquake Ground Motions. *Earthquake Spectra*, 4(4):687-729. <https://doi.org/10.1193/1.1585498>.

- Simpson, D., Van Meirvenne, M., Lück, E., Rühlmann, J., Saey, T. y Bourgeois, J. (2010). Sensitivity of multi-coil frequency domain electromagnetic induction sensors to map soil magnetic susceptibility. *European Journal of Soil Science*, 61(4):469-478. <https://doi.org/10.1111/j.1365-2389.2010.01261.x>.
- Singh, S. K., Lermo, J., Domínguez, T., Ordaz, M., Espinosa, J. M., Mena, E. y Quaas, R. (1988). The Mexico Earthquake of September 19, 1985—A Study of Amplification of Seismic Waves in the Valley of Mexico with Respect to a Hill Zone Site. *Earthquake Spectra*, 4(4):653-673. <https://doi.org/10.1193/1.1585496>.
- Singh, S. K., Reinoso, E., Arroyo, D., Ordaz, M., Cruz-Atienza, V., Pérez-Campos, X., Iglesias, A. y Hjörleifsdóttir, V. (2018). Deadly Intraslab Mexico Earthquake of 19 September 2017 (Mw 7.1): Ground Motion and Damage Pattern in Mexico City. *Seismological Research Letters*, 89(6):2193-2203. <https://doi.org/10.1785/0220180159>.
- Spies, B. R. y Frischknecht, F. C. (1991). Electromagnetic Sounding. En *Electromagnetic Methods in Applied Geophysics: Volume 2, Application, Parts A and B*, capítulo 5 (pp. 285-425). Society of Exploration Geophysicists. <https://doi.org/10.1190/1.9781560802686.ch5>.
- SSN (2017). Servicio Sismológico Nacional. *Sismo del día 19 de Septiembre de 2017, Puebla-Morelos (M 7.1)*. Reporte Especial, pp. 11. SSN, UNAM, México. <http://www.ssn.unam.mx>.
- Telford, W. M., Geldart, L. P., Sheriff, R. E. y Keys, D. A. (1978). *Applied Geophysics*. Cambridge University Press, E.E.U.U. <https://doi.org/10.1017/CBO9781139167932>.
- Tokimatsu, K., Shinzawa, K. y Kuwayama, S. (1992). Use of Short-Period Microtremors for V_s Profiling. *Journal of Geotechnical Engineering*, 118(10):1544-1558. [https://doi.org/10.1061/\(ASCE\)0733-9410\(1992\)118:10\(1544\)](https://doi.org/10.1061/(ASCE)0733-9410(1992)118:10(1544)).
- Wai-Lok Lai, W., Dérobert, X. y Annan, P. (2018). A review of Ground Penetrating Radar application in civil engineering: A 30-year journey from Locating and Testing to Imaging and Diagnosis. *NDT&E International*, 96:58-78. <https://doi.org/10.1016/j.ndteint.2017.04.002>.
- Wathelet, M. (2008). An improved neighborhood algorithm: Parameter conditions and dynamic scaling. *Geophysical Research Letters*, 35(9):L09301. <https://doi.org/10.1029/2008GL033256>.
- Wood, C. M., Deschenes, M., Ledezma, C., Meneses, J., Montalva, G., and Morales-Velez, A. C. (2019). Dynamic site characterization of areas affected by the 2017 Puebla-Mexico city earthquake. *Soil Dynamics and Earthquake Engineering*, 125:105704. <https://doi.org/10.1016/j.soildyn.2019.105704>.
- Wood, C. M., Woodfield, L. J., Rahimi, S., Rosado-Fuentes, A., Sánchez-Sesma, F. J., Cruz-Jiménez, H., Mayoral, J. M. y de la Rosa, D. (2023). Shear wave velocity and site period measurements for the western portion of the Mexico City Basin following the Mw7.1 2017 Puebla-Morelos, Mexico, earthquake. *Earthquake Spectra*, 39(1):505-527. <https://doi.org/10.1177/87552930221120834>.

- Xu, R. y Wang, L. (2021). The horizontal-to-vertical spectral ratio and its applications. *EU-RASIP Journal of Advances in Signal Processing*, 75. <https://doi.org/10.1186/s13634-021-00765-z>.